UNIVERSITY OF OKLAHOMA

GRADUATE COLLEGE

EFFECTS OF SEISMIC LOADING ON

OKLAHOMA HIGHWAY BRIDGES

A THESIS

SUBMITTED TO THE GRADUATE FACULTY

in partial fulfillment of the requirements for the

Degree of

MASTER OF SCIENCE

By

IVANNA A. KAID BAY CORTEZ
Norman, Oklahoma
2016

EFFECTS OF SEISMIC LOADING ON
OKLAHOMA HIGHWAY BRIDGES

A THESIS APPROVED FOR THE
SCHOOL OF CIVIL ENGINEERING AND ENVIRONMENTAL SCIENCE

BY

<div style="text-align: right">

_____
Dr. P. S. Harvey Jr., Chair

_____
Dr. K. K. Muraleetharan

_____
Dr. N. Wang

</div>

To my beloved family

Acknowledgements

Contents

List of Figures

List of Tables

Abstract

Since 2006, the number of magnitude (M) 3.0 and larger earthquakes occurring in Oklahoma has increased dramatically. Large magnitude (> 5.0) events have caused damage to residential structures, which raises a concern about the potential for damage to Oklahoma's highway bridges and their components. The purpose of this study is to assess the seismic response of the most common bridge class in Oklahoma and evaluate its potential for damage. This is accomplished by considering the Oklahoma Department of Transportation's on-system bridge inventory and determining the most typical bridge class — a 3-span prestressed concrete girder bridge. A representative bridge was modeled in detail using nonlinear finite elements and a series of transient analyses were performed to assess its performance under actual Oklahoma ground motions. A suite of 27 bidirectional ground motions from the September 3, 2016 M 5.8 Pawnee Earthquake (the largest event to date) were used for the transient analysis.

Transient time-history analyses were performed and responses such as bearing deflection and column curvature were recorded and presented. Small, linear bearing deflections and column curvatures were observed for the measured ground motions. To assess the response of the typical highway bridge under higher intensity ground motions, an incremental dynamic analysis was performed. The measured ground motions from seismic station GS.OK005 was incrementally scaled to AASHTO design levels and higher. At the design 1-second spectral acceleration $S_1 \approx 0.10g$, larger bearing deflections and column curvatures were predicted, including closing of the gap in the

elastomeric bearings and engagement of the anchor bolts. The ground mtoin was further scaled to 50% higher than the design level ($S_1 = 0.15g$), which corresponds to 75% of ground-motion predictions near the epicenter per ShakeMap. At this ground-motion intensity, bearing deflections and column curvatures were disproportionately larger than at design level due to nonlinear effects such as the yielding of the steel and sliding of the expansion type bearings. A maximum column curvature of 82% of the yield curvature was observed. For the measured ground motions and up to 1.5 times the design level, no damage was predicted. However, damage may occur at observed intensities closer to the epicenter.

Chapter 1

Introduction

1.1 Overview

Bridges are essential infrastructure systems that provide mobility and development of commerce in any region. With more earthquakes occurring in traditional and non-traditional seismic areas of the United States (U.S.) highway bridges are being affected and possibly weakened. Damage of highway bridge systems caused by characteristic aging and environmental effects incurs an increase in costs for federal and state agencies in charge of the supervision, repairing, and maintaining these systems. The Oklahoma Department of Transportation (ODOT) has provided an average rate of construction of 60 highway bridges per year (from 1910 to 2016) while managing an inventory of over 6000 bridges.

As a recent matter, since 2006, the cumulative number of magnitude 3.0 and larger earthquakes that have occurred in Oklahoma increased from 8 in 2006 to 1741 earthquakes by the end of 2015 (USGS, 2016a). Frequent earthquakes and progressive deterioration on bridges may lead to a reduction in structural strength, and thus make the system vulnerable to resist future earthquakes (Ghosh, 2013). This increase in earthquake occurrence in the area has raised concern to bridge owners about the potential damage to the structural integrity of highway bridges and their components.

In response to this matter, this study is intended to assess the fragility of a typical

bridge class under seismic loading, using Oklahoma as a case study. The results of this work will lead to a better understanding of the effect of seismic loads from moderate earthquakes, as well as a seismic risk assessment for Oklahoma. The assessment of highway bridges in Oklahoma is essential for informed bridge inspection and future considerations of bridge design in Oklahoma.

1.2   Seismicity in Oklahoma

Earthquakes are expected to occur in tectonically active regions, for example along the plate boundaries of the U.S. West Coast and within the Intermountain West. The U.S. Mid-Continental Region has been generally considered as part of the tectonically stable continental interior region (Howard et al., 1978) and has defined seismic source zones by the location of historic earthquake epicenters, for instance the New Madrid fault. Faults located in the Central U.S. produce very low deformation rates if compared with tectonically active regions of the Western U.S.

Oklahoma is located within the U.S. Mid-Continental Region, and the Oklahoma Geological Survey (OGS, 1987) established that Oklahoma possess the presence of one major natural fault, known as Meers fault, which is part of a major systems of northwest trending faults that form the boundary between the Wichita Mountains and the Anadarko basin in Southwestern Oklahoma. The seismic activity of Meers fault has not been very pronounced; earthquakes exceeding magnitude 4.0 have not occurred along the Meers fault since Fort Sill was established 145 years ago. Moreover, only one earthquake above magnitude 1.6 has occurred in the Meers fault region since the Oklahoma seismic network was established in 1977. Therefore, the Meers fault has remained basically aseismic over the last 25 years (Lawson, 1985). Fig. 1.1 represents the seismic hazard for 2% probability of exceedance in 50 years in peak ground acceleration for Oklahoma provided by the USGS (United States Geological Survey). The high seismicity
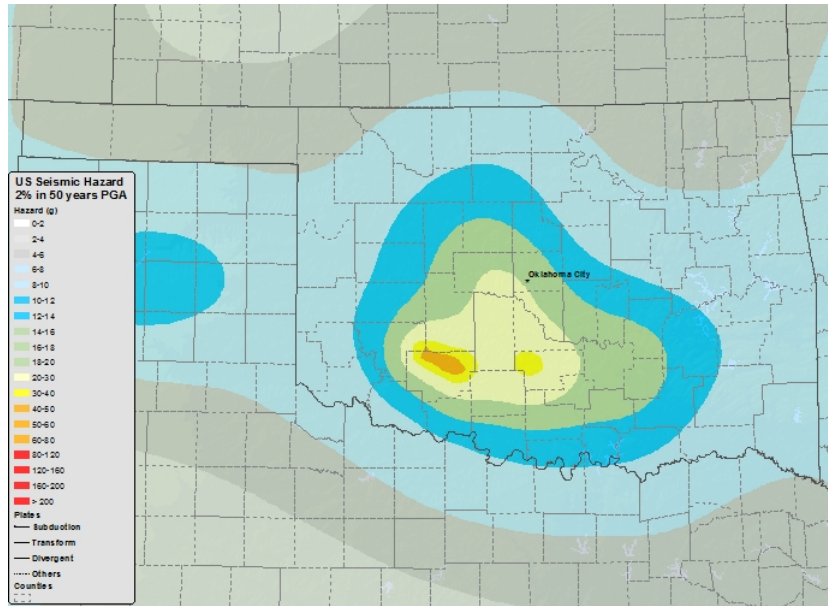
Figure 1.1: Seismic hazard in Oklahoma: 2% probability of exceedance in 50 years peak ground acceleration (USGS, 2016a).

region (yellow/orange) in the figure indicates the setting of the Meers fault.

Since 2006, more than 1700 earthquakes of magnitude 3.0 have occurred in Oklahoma (USGS, 2016a). However the seismic activity was not close to Meers fault. The USGS map (Fig. 1.2) shows all the earthquakes of magnitude 3.0 and above that have occurred in Oklahoma since 2009. The increase in seismicity activity represents a temporal change in earthquake rate for the state. Llenos and Michael (2013) indicated that since 2008 changes of the rate of small-to-moderate earthquakes in Oklahoma were not related to random fluctuations in natural seismicity. Furthermore, Hough and Page (2015) stated that the rate of tectonic earthquakes in Oklahoma was significantly lower than would be implied from seismicity rates in the twentieth century and the rate since 2008 far exceeds that during any preceding time period since 1900. Another source of seismicity in Oklahoma is located near the El Reno area, which produced a 5.5 moment magnitude earthquake (the 1952 El Reno earthquake), which was suspected to be related to local oil and gas production (Nicholson and Wesson, 1992).

Due to the elevated number of recent earthquakes appearing in areas where specific

3
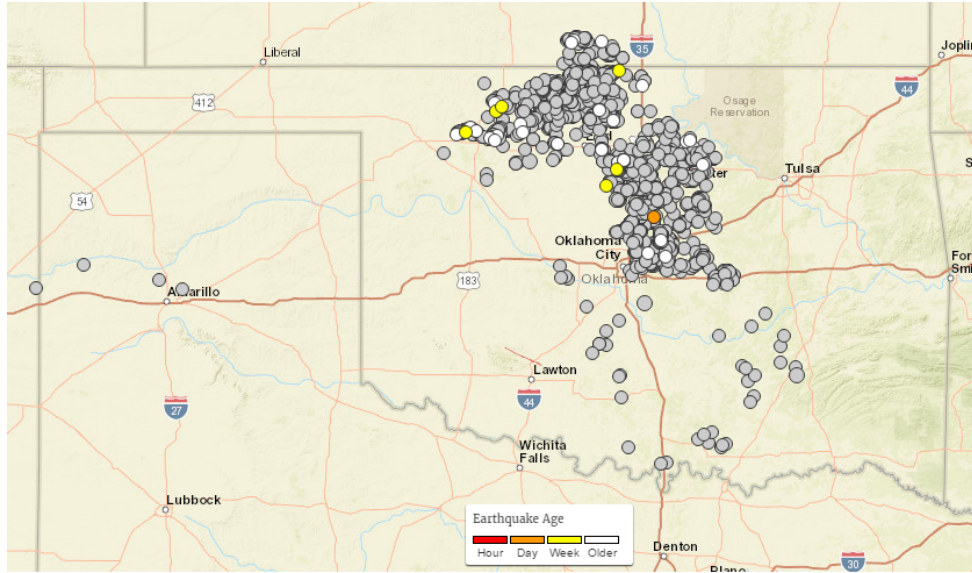
Figure 1.2: Earthquakes magnitude 3.0 and above that have occurred in Oklahoma since 2008 (USGS, 2016c).

types of industrial activities were performed, Ellsworth (2013) indicated the possibility that these events were induced by human activity that altered the stress and/or pore pressure in the underlying rocks. Most of these potentially induced events occur shortly after the industrial activity initiates, while in other cases they occur long after the activity has ceased (Townend and Zoback, 2000).

A study performed by Holland (2013) revealed that a series of felt earthquakes in Southcentral Oklahoma with maximum moment magnitude of 2.9 correlated with fracking operations in an adjacent well. Furthermore, Keranen et al. (2013) conjectured that wastewater injection into a dwindling oil field was the potential cause of the high earthquake activity in Central Oklahoma, triggering a moment magnitude 5.7 earthquake. Keranen et al. (2013) remarked that this major earthquake in Central Oklahoma caused damage to homes and unreinforced masonry buildings close to the epicenter. Natural earthquakes are independent of time while potentially-induced earthquakes vary with time due to changes in injection rate (McGarr et al., 2015). Rubinstein and Mahani (2015) determined that the largest amount of current earthquakes in Central and North-

central Oklahoma are very likely initiated by the injection of waste water in disposal wells. Proximity to the earthquake epicenter needs to be considered in assessing the seismic hazard to bridges.

Although potentially induced earthquakes have caused minor damage in Oklahoma, catastrophic events or fatalities have not been observed. Because earthquake hazard in Oklahoma is now comparable to the hazard in areas habitually recognized for earthquakes, such as California (Petersen et al., 2015), Oklahoma bridge owners undoubtedly are concerned with the effects that repeated earthquake loads might cause to the highway bridges. This study is intended to evaluate the hazard from recent earthquakes considering typical bridge classes that are representative of the bridge inventory in Oklahoma. Henceforth, a distinction between natural and potentially-induced events will not be made.

1.3 Bridge Fragility Curves

In general, fragility curves serve as adaptable probabilistic tools that estimate seismic vulnerability in a system. Due to the vulnerability of transportation systems in earthquake-prone regions, fragility curves have been adopted to assess the risk to highway bridges for a given ground motion intensity. Fragility curves represent the probability of meeting or exceeding some damage state for a given ground-motion intensity measure (e.g., peak ground acceleration or spectral acceleration).

This probabilistic approach initially was put in practice by approximating the structural damage in nuclear facilities (Bley et al., 1983; Campbell et al., 1998). Then, the fragility curves methodology expanded into other structures by the formulation of an approach for defining empirical fragility curves for highway bridges based on limited data readily available from the National Bridge Inventory (NBI) (Mander et al, 1999). The rapid screening approach was adopted by a Geographical Information

System (GIS) based risk assessment tool, named HAZUS (Hazards United States), for defining fragility curves (FEMA, 1997). The implementation of fragility curves is related to pre-earthquake preparation, retrofit prioritization, and loss estimation (Choi et al., 2004), as well as post-design verification (Nielson and DesRoches, 2007a) and for post-earthquake inspection prioritization schemes (Heinrich et al., 2015). Over the last two decades, researchers have used different methodologies and approaches related to field observations and advanced analysis using analytical models to determine fragility curves. Moreover, they have transitioned from empirical to analytical methods.

1.3.1 Empirical Fragility Curves

Empirical fragility curves are generated from past earthquake damage distribution data and require a post-earthquake evaluation of the bridges within a bridge type. The empirical fragility curves aid to facilitate a general idea about the relationship between a certain damage state of the structure and the ground-motion intensity; they can be generated by the application of estimation or inference methods.

After major earthquakes occurring in the late 1980s and mid 1990s (e.g., the 1989 Loma Prieta, 1994 Northridge and 1995 Kobe earthquakes), many researchers used the seismic data of these events to develop empirical fragility curves for the different structure conditions. Basoz and Kiremidjian (1997) performed a study of damage to highway bridges from Northridge earthquake by using a damage frequency matrix. They investigated damage states of bridges after the earthquake using logistic regression analysis to obtain empirical fragility curves and proposed new damage state definitions for concrete bridges.

Der Kiureghian (2002) proposed a framework for using an inference method (Bayesian approach) for assessing the seismic fragility of electrical substation equipment. The framework was based on field observations of past earthquakes and accounted for aleatoric and epistemic uncertainties. Shinozuka et al. (2003) presented an

approach for bridge fragility curve development using a traditional inference procedure (maximum likelihood method) in combination with hypothesis and goodness-of-fit tests to approximate the parameters of lognormal probability distribution relating to fragility curves.

Elnashai et al. (2004) created a procedure to derive vulnerability functions for reinforced concrete (RC) bridges using material characterization and high quality earthquake logs. They evaluated 4 bridges to obtain different over-strength ratios and found out that it was feasible to derive scaling factors that facilitate the process of deriving vulnerability functions for classes of bridges once a general correlation was established. The development of empirical fragility curves is hindered by some limitations that diminish their effectiveness and reliability. Namely, they are related to a database of specific soil conditions, select ground motions and particular structures that cannot be used for general purposes. Also, the efficiency of empirical functions is associated with a large degree of uncertainty from the subjective opinion of bridge inspectors to specify damage states for a particular bridge class. Even though these restrictions exist, empirical fragility curves still assist as a benchmark for analytical fragility curves.

1.3.2 Analytical Fragility Curves

Analytical fragility curves are based on structural modeling and response simulations. They offer a more robust way to assess the risk of bridge damage during different levels of earthquakes. Typically, analytical fragility curves are employed when ground motion data or history data of past earthquake in a region is limited or not available. On the other hand, they can also be used in conjunction with experimental or actual damage data.

Different approaches have emerged to develop analytical fragility curves for classes of bridges or individual bridge structures. Among the diverse studies the majority focus on the use of elastic spectral response, non-linear static analysis, or non-linear time

history dynamic analysis methods.

Hwang et al. (2000) developed a simple procedure to evaluate the expected damage of bridges and roadways on major routes in Memphis, Tennessee resulting from New Madrid earthquakes using the aid of GIS technology. To generate the fragility curves, an elastic spectral analysis for the forces/displacements (also known as demand) was calculated and then use in conjunction with the computed capacity of each bridge components by employing the C/D (capacity/demand) ratio method to assign a particular damage state for various levels of ground-motion intensity.

Because the simplicity of this method, the fragility curves with high reliability were the ones from bridges that were only expected to perform in the linear elastic range. Enhancement of the elastic spectral analysis was made by considering a methodology supporting the benefits of including non-linearities in a static analysis without the computational effort of including non-linearities in a time history analysis.

Shinozuka et al. (2000b) employed a capacity spectrum method (non-linear static analysis method) for generating analytical fragility curves of multiple three-span continuous concrete girder bridges located in the Memphis area. The method used a pushover curve to calculate the demand in combination with a reduced response spectrum to obtain the capacity. The results indicated an excellent agreement for the minor damage state, but the method was shown to be not as appropriate for the major damage state where non-linear properties noticeably alter the response.

The non-linear static analysis method was originally developed for buildings (ATC, 1996). Because of this, the bridge structure type definition and valuation of effective hysteretic damping is inaccurate. To address the concerns of this method, more detailed and complicated bridge models needed to consider the dynamic loading participation for more precisely capturing geometric non-linearities and material inelasticity of a bridge. Therefore, non-linear time history analysis was employed to simulate the seismic re-

sponse of a structure for a suite of ground motions.

Shinozuka et al. (2000a) performed a Monte Carlo simulation to investigate non-linear dynamic responses of two bridges typical in Southern California before and after column retrofit. The resulting fragility curves after column retrofit with steel jacketing was found to be less brittle compared to those before retrofit.

Many studies have applied non-linear analytical methods to generate fragility curves. Fragility curves can be created by following a basic framework outlined below, with some variations of the application analysis. First, a suite of ground motions representative of the seismic hazard in the area is combined with analytical bridge models by performing a non-linear time history analyses. Next, peak structural responses of individual components of the bridge are obtained and plotted versus the ground-motion intensity parameter related to the particular earthquake that produced the response. This represents a *probabilistic seismic demand model* (PSDM) which characterizes the correlation among response and ground-motion intensity. The demand model can be combined with predefined limit states (capacity) of each component to generate the fragility curves of the system.

Choi et al. (2004) developed fragility curves by using non-linear analytical models and a suite of synthetic ground motions, for four bridge types frequently found in the CSUS. Fragility curves were created for the individual components of each bridge type and then combined to characterize the whole bridge system. Comparison of the different fragility curves showed that the most susceptible bridge types were the multi-span simply supported and multi-span continuous steel-girder bridges.

Mackie and Stojadinovic (2003) evaluated the selection of an ideal PSDM for two-span single-bent highway overpass bridges with roller abutments located in California. They performed bridge design parameter (such as column diameter) sensitivity studies to obtain the optimal PSDM. Then the same PSDM was re-computed to assess the

equivalency of response using an *incremental dynamic analysis* (IDA). The findings demonstrated that the optimal PSDMs are maximum column moment and column drift ratio.

Nielson and DesRoches (2007a) developed three-dimensional analytical models and performed non-linear time history analyses to create fragility curves for 9 classes of typical three- span bridges located in the CSUS while considering the contribution of multiple bridge components. After comparison of the suggested fragility curves with those presently found in HAZUS, they found that the multi-span simply supported steel girder bridge class showed good agreement with the HAZUS values, but they observed lower vulnerability for other simply supported classes relative to HAZUS. To expand the methodology, Nielson and DesRoches (2007b) considered the contribution of major components of the bridge (e.g., bearings, columns, and abutment) to the overall bridge system fragility. They discovered that the bridge system is more fragile than any one of the individual components.

Zhang and Huo (2009) investigated the most favorable design parameters of isolation devices to decrease the general damaging potential of seismically-isolated bridges. They used 250 earthquake motions in combination with non-linear time history analyses and two different approaches (IDA and unscaled ground motions methodology) for obtaining two set of PSDMs and generating fragility curves. They found out that PSDMs generated with unscaled ground motions required less computational effort while PSDMs created with IDA needed more, yet were more precise.

Alam et al. (2012) determined fragility curves of a three-span continuous highway bridge equipped with laminated rubber bearings and shape memory alloy (SMA) restrainers. Fragility functions were derived based on non-linear IDA results of the bridge subjected to medium to strong ground motions. They found out that the failure probability of the bridge system was controlled by the bridge piers over the isolation bearings,

10

while the presence of SMA restrainers in the bridge system displayed high probability of failure when the system was isolated with lead rubber bearings.

Two methods are commonly used to generate PSDMs. The first is called the cloud approach (Choi et al., 2004; Mackie and Stojadinovic, 2003; Nielson and DesRoches, 2007a,b). In this method, un-scaled earthquake ground motions are employed in non-linear time history analysis to create a PSDM. The second is called the scaling approach (Zhang and Huo, 2009; Alam et al., 2012), which involves scaling all the ground motions to a desire intensity level throughout the application of IDA for each level of intensity.

Even though each type of analytical fragility curve method possess limitations, over-all this approach has become commonly accepted due to their easy application for different bridge classes located in geographical regions with insufficient seismic damage records.

1.3.3 HAZUS Fragility Curves

Fragility curves define the probability of exceeding a given damage (limit) state as a function of the ground-motion intensity. HAZUS (FEMA, 2003), a standardized methodology for estimating potential losses due to natural disasters, developed "standard bridge" fragility curves for *slight*, *moderate*, *extensive*, and *complete* damage (Mander, 1999). A qualitative description of the four damage states is given in Table 1.1.

For each of the 28 bridge classes described by HAZUS, a median PGA (peak ground acceleration) value is given for each damage state, which is converted to 1.0-second spectral acceleration (S_1) by a combination of the factors K_{3D}, K_{skew}, and K_{shape} to account for variations among the individual bridges due to the number of spans of the bridge, the skew angle of the bridge, and the estimated period of the bridge, respectively. The information needed from each bridge to complete these calculations in-

Table 1.1: HAZUS damage (limit) states (FEMA, 2003).

Limit State	Description
Slight	Minor cracking and spalling to the abutment, cracks in shear keys at abutments, minor spalling and cracks at hinges, minor spalling at the column (damage requires no more than cosmetic repair) or minor cracking to the deck.
Moderate	Any column experiencing moderate (shear cracks) cracking and spalling (column structurally still sound), moderate movement of the abutment (< 2 in.), extensive cracking and spalling of shear keys, any connection having cracked shear keys or bent bolts, keeper bar failure without unseating, rocker bearing failure or moderate settlement of the approach.
Extensive	Any column degrading without collapse – shear failure – (column structurally un-safe), significant residual movement at connections, or major settlement approach, vertical offset of the abutment, differential settlement at connections, shear key fail-ure at abutments.
Complete	Any column collapsing and connection losing all bearing support, which may lead to imminent deck collapse, tilting of substructure due to foundation failure.

cludes the year built, number of spans, skew angle, main span material, and maximum span length, all of which can be found in the National Bridge Inventory (NBI) (US-DOT, 2015). The *HAZUS MR4 Technical Manual* provides a full description of the calculations for fragility curves (FEMA, 2003). These same fragility curves are used by ShakeCast (Wald et al., 2008) to create a priority ranking of bridges to inspect after an earthquake, which served as the basis of the smart bridge inspection radii developed for the Oklahoma Deparment of Transportation (Heinrich et al., 2015). The fragility curves are based on standard bridges and cannot take into consideration all the details of an individual bridge. The purpose of this structural analysis is, in part, to verify the validity of the standard HAZUS fragility curves for Oklahoma bridges.

In the event of an earthquake, ShakeCast uses the median (50%) S_1 for each of the damage states to determine a list with the priority ranking of bridges to inspect. The California Department of Transportation (Caltrans) uses a trigger S_1 value of $0.10g$ instead of a fragility curve for slight damage. Heinrich et al. (2015) recommended the use of a base fragility curve with a median S_1 value of $0.0833g$ for Oklahoma bridges. A trigger S_1 value corresponding to a 25% probability of being in a slight damage state was found to be $0.0556g$ for all Oklahoma bridges, which formed the basis of the smart bridge inspection radii. There values will form a benchmark for subsequent analysis.

1.3.4 Deterioration

Fragility estimation methods previously described have been commonly used to assess seismic vulnerability of pristine (non-deteriorating) highway bridges, while neglecting the influence of progressive deterioration and sudden deterioration affecting the bridge performance (Basoz and Kiremidjian, 1997; Nielson and DesRoches, 2007a). To be able to obtain fragility curves that represent in-service highway bridges, deteriorating effects should be considered in the modelling of the bridge.

In general, the deterioration process of highway bridges is represented by progres-

sive and sudden deterioration. Progressive deterioration is a slow and continuing degradation process caused primarily by aging mechanisms and environmental factors. Sudden deterioration is associated with quick changes in the structural capacity produced by significant events such as earthquakes or blasts.

Corrosion   Progressive deterioration in RC bridges is initiated as a reduction of the structural capacity by penetration of chloride ions on the concrete cover that produces a reaction in the reinforcing steel, also known as corrosion. Usually, corrosion of bridges occurs at locations near the sea coast and in regions where deicing salts are employed for snow and ice removal. Different studies have investigated the degradation of bridges by corrosion.

Liu and Weyers (1998) used a deterministic corrosion model by monitoring corrosion rates (using a linear polarization technique and the guarded ring method), concrete ohmic resistance, and temperature of 44 bridge deck slabs over a 5-year period. It was confirmed by using a non-linear regression model that corrosion depends on the concrete chloride content, temperature, ohmic resistance, and active corrosion time. Moreover, they found that the linear polarization method was able to capture the average annual corrosion rate.

Alternatively, Stewart and Rosowsky (1998) developed a probabilistic deterioration model to estimate structural failure by corrosion of a reinforced concrete continuous slab bridge exposed to deicing salts and marine environments. Using a Monte Carlo simulation, they discovered that corrosion reduced the cross-sectional area of the reinforcing steel, increasing failure probabilities. Using a similar probabilistic deterioration model, Enright and Frangopol (1998) studied the flexural strength loss in concrete bridge beams due to corrosion of steel reinforcement. Their main finding related to a linear increase with time of the mean value of the resistance loss function.

Other researchers have considered the joint effects of corrosion and seismic events

by developing seismic fragility curves with the inclusion of aging effects in the capacity model. Choe et al. (2009) modeled probabilistic drift and shear force capacity models for time-dependent corroding RC columns exposed to marine environment by using a reduced diameter of reinforcement steel. They included uncertainties in capacity, corrosion models, environmental conditions, material properties, and structural geometry for developing fragility curves. As a result, it was observed that the shear force capacity degradation with corrosion was faster than the degradation of the drift capacity.

Ghosh and Padgett (2010) formulated time-dependent seismic fragility curves for multi-span continuous highway bridges located in CSUS considering effects of aging and deterioration. They estimated the impact of lifetime exposure to chlorides from deicing salts on the seismic performance, anticipating corrosion of RC columns and steel bridge bearings. By using three-dimensional non-linear dynamic analysis and a probabilistic analysis accounting for variation in bridge and corrosion parameters, they noticed that RC columns and expansion bearings experienced an increase in vulnerability.

Likewise, Akiyama et al. (2011) created a procedure to integrate the probabilistic hazard related to airborne chlorides into life-cycle seismic reliability assessment of RC bridge piers located in Japan. They estimated the relationship between lateral load and displacement based on the buckling of corroding longitudinal reinforcement bars. Their findings showed that the cumulative-time failure probabilities of RC bridge piers located in seismic zones were influenced by the effect of airborne chlorides.

Scour The effects of progressive deterioration caused by scour, which is the most common cause of highway bridge failures in the United States (Kattell and Eriksson., 1998), have been investigated as well. For instance, Deco and Frangopol (2011) considered a framework for the quantitative risk assessment of a highway bridge under multiple hazards (live loads, environmental attacks, scour, and earthquakes) located in

Wisconsin. Annual failure probabilities for the hazards were evaluated individually, and different levels of detailing were given depending on the hazard contribution to the total risk of the bridge. The results pointed out that risk associated with scour exceeded the risk associate with live loads and corrosion.

In addition, Dong et al. (2013) presented a framework for evaluating the time-varying sustainability of bridges under flood-induced scour, considering the effects of deterioration. They performed non-linear dynamic analysis of a single bent RC bridge including a deterioration model that represented the corrosion of the steel reinforcement and spalling of concrete cover to obtained fragility curves. The results showed that because the deterioration provoked severe reduction in structural capacity, the sustainability of bridges located in regions prone to high corrosion were an issue compared with the bridges located in low-corrosion regions.

Repeated seismic loading   In locations of moderate to high seismicity, repeated seismic shocks and consideration of the history of past earthquake during the lifetime of the existing structures were found to contribute to the fragility of the system. To represent the accumulation of damage caused by repeated loading due to earthquake shocks, Amadio et al. (2003) investigated the effects of repeated earthquake ground-motions on the response of single-degree-of-freedom systems (SDOF) with non-linear behavior. They performed a comparison with the effect of a single seismic event on the originally non-damaged system for different hysteretic models (elastic-perfectly plastic, bilinear, linearly degrading stiffness and Clough's model). The results indicated that multiple events could induce a considerable accumulation of damage and a consequent reduction in the quality factor.

Sanchez-Silva et al. (2011) presented a stochastic model to study the time-dependent performance of highway systems using a point process approach. They integrated uncertainty about the occurrence time and the damage caused by short-term or sudden

events (e.g., earthquakes) and progressive deterioration (e.g., corrosion and fatigue). They found that the probability of failure could be suggestively higher if the progressive failure mechanisms were considered.

Furthermore, Ghosh et al. (2015) proposed a framework to estimate damage accumulation in highway bridges under multiple shock scenarios after developing damage index prediction models and accounting for the probabilistic nature of the hazard. Multiple main shocks during the service life and multiple aftershock earthquake occurrences following a single main shock scenarios were applied to a single column box girder bridge located in California as a case study. The results indicated that in both scenarios there was a clear correlation in damage index exceedance probabilities due to repeated shocks within the time window of concern.

Multiple hazards such as aging and environmental effects, scour and repeated earthquake shocks have been shown to likely affect seismic performance of highway bridges. Neglecting aging and deterioration may lead to non-conservative estimates of potential damage in a bridge. Because of this, many researches have recommended including deterioration models in bridge seismic vulnerability (Ghosh and Padgett, 2010; Sanchez-Silva et al., 2011; Ghosh et al., 2015).

1.4 Summary

This chapter gave a background on the seismic hazard in Oklahoma, highlighting the recent rapid increase in the number and magnitude of earthquakes. Bridge fragility was addressed by reviewing different types of fragility curves and deterioration processes such as corrosion, scour, and repeated seismic loading. From the review of bridge fragility curves, it was determined that key damage indicators are related to column and bearing responses which will be used in subsequent analysis. In the following chapter a detailed analysis of the Oklahoma's bridge inventory is presented.

Chapter 2

Oklahoma Bridge Inventory Analysis

2.1 Overview

To select the Oklahoma bridge that will be modeled in this study, it is important to have a detailed understanding of the state's bridge inventory. The Oklahoma Department of Transportation (ODOT) provided data for 6815 bridges owned and maintained by the state on the ODOT-designated highway system, referred to as "on-system" bridges, which will serve as the inventory for this study. Note that "off-system" bridges (i.e., bridges owned and maintained by a county, city, or other local or regional governmental unit, and not on the ODOT-designated highway system) were not included.

2.2 Structure Type Statistics

For analyzing the bridge inventory, it is convenient to focus on typical structure types. This will make the amount of data and time to process it more manageable. To proceed systematically and in an organized way, it is essential to identify different structure types and the characteristics specific to each structure type. Based on the National Bridge Inventory (NBI) database (FHWA, 1995a), each structure type is organized by design type and material type (NBI Item 43). Table 2.1 presents the bridge distribution by design type. Culvert bridges constitute over 44% of the inventory, and, because culvert bridges are assumed to represent a different type of system, they are not taken

18

Table 2.1: Design main span for all bridges in the inventory.

Design type	Number	Percentage (%)
Culvert	3042	44.63
Girder	3002	44.05
Slab	508	7.45
Floorbeam	58	0.85
Frame	48	0.70
Box Beam – Multiple	45	0.66
Tee Beam	29	0.43
Arch – Deck	9	0.13
Box Beam – Single	7	0.10
Segmental	6	0.08
Truss – Deck	2	0.02
Other	1	0.01
Total	6815	100.00

into account in this study. Girder bridges are the dominant design type with 44% of the inventory. The remaining bridge design types represent less than 12% of the inventory and will not be considered further in this study because they are not characteristic of a typical Oklahoma bridge.

Next, the girder bridges were categorized based on kind of material (NBI segment 43A). Table 2.2 lists the defined material types, as well as the proportion of the 3002 girder bridges that fall into the respective material types. The biggest percentage is concentrated in Prestressed Concrete Girder bridges (47%), followed by Steel Girder (28%) and Continuous Steel Girder bridges (22%). The remaining bridge structure types represented less than 3% of the girders bridges and will not be considered further in this study because they are not representative of a typical Oklahoma bridge.

After identifying the bridge structure types, the most typical values for number of spans, dimensions such as main span length and bridge length, as well as the year built were obtained. Then a condensed list of bridges for the bridge structure types was generated. In areas of the United States that are not seismically active, seismic

Table 2.2: Bridge classes by construction material.

Name	Number	Percentage (%)
Prestressed Concrete Girder	1423	47.40
Steel Girder	849	28.28
Continuous Steel Girder	660	21.99
Concrete Girder	61	2.03
Prestressed Continuous Concrete Girder	8	0.27
Others	1	0.03
Total	3002	100.00

design in bridges was mainly considered after the 1990s. Because of this, the year that a bridge was constructed is an important indicator of the type of bridge design and seismic considerations. Furthermore, the year shows how long the bridge has been exposed to environmental or structural hazards, indicating the bridge deterioration over the years.

The skew angle is a common bridge parameter, but it is not the focus of this study. Sullivan (2010) specified that higher skew angles lead to fragile bridge systems while skew angles less than 30 degrees do not altered the bridge susceptibility. The critical skew angle, below which skew does not play a critical role in fragility, was then considered to be 30 degrees. From the girder bridge inventory data (3002 bridges), 39% of the bridges are skewed. Of these skewed bridges, only 62% have skew greater than 30 degrees. When skew angle is small, it is more feasible to consider simplifying assumptions for modelling. Because the number of bridges that have zero skew (61%) and that have skew angles less than 30 degrees (37%) is significant, skew angle will not be discussed in the following sections describing the selection of typical bridge classes but will be considered for the final selection.
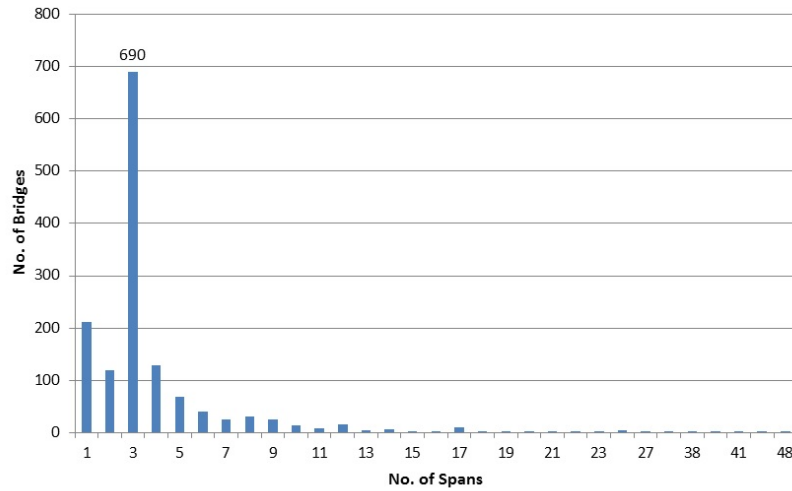
Figure 2.1: Number of spans histogram for Prestressed Concrete Girder bridges.

2.3 Bridge Class

The following subsections focus on filtering bridge characteristics such as number of spans, main span length, bridge length (total length) and year built for each of the major structure types: Prestressed Concrete Girder bridges, Steel Girder bridges and Continuous Steel Girder bridges. The bridge characteristics are characterized using histograms and key statistics (e.g., mode).

2.3.1 Prestressed Concrete Girder Bridges

Fig. 2.1 depicts the data range for number of main spans for the Prestressed Concrete Girder bridges. Examination of the graph indicates that the majority of the bridges possess one to five spans. Single-span bridges constitute 14.8% of the inventory, and multi-span bridges constitute the remaining 85.2% of the inventory. Moreover, it is observed that 48% of the bridges are represented by three spans. As such, this study focuses on three-span Prestressed Concrete Girder bridges, hereinafter denoted 3SPC bridges.

Histograms for main span length and bridge length are presented in Figs. 2.2 and

Figure 2.2: Main span length histogram for Three-Span Prestressed Concrete Girder bridges.
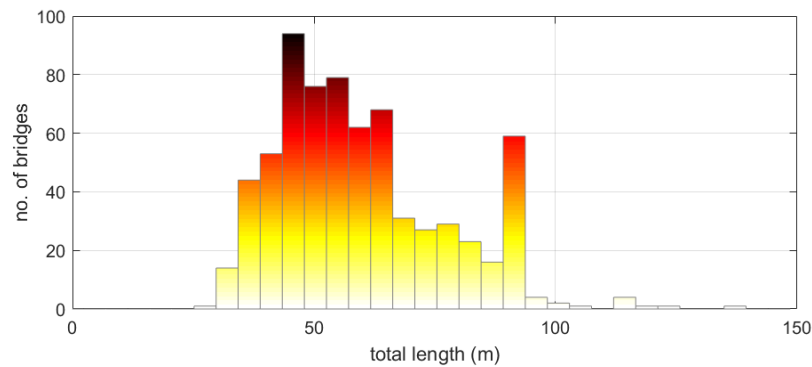
Figure 2.3: Bridge length histogram for Three-Span Prestressed Concrete Girder bridges.

2.3, respectively. The main span length and total length data are binned in 1.5 m (5 ft.) and 4.5 m (15 ft.) increments, respectively. Although the data shows variation, there are some trends to highlight for the main span length and bridge length histograms.

For instance, the largest groupings of main span length are concentrated at 15.25 m (50 ft.) and 30.5 m (100 ft.), while the predominant bridge lengths are concentrated at 45.72 m (150 ft.) and 91.44 m (300 ft.). Upon closer inspection of the predominant main span lengths and bridge length, the bridge length is three times larger than the main span length, which for a three-span bridge would indicate equal span lengths.

The relationship between main span length and the bridge length with the number of bridges is represented in Fig. 2.4 (left). It is evident from Fig. 2.4 (right) that the bridge length is commonly equal to three times the main span length, as indicated by

Figure 2.4: Prestressed Concrete Girder Bridges: (left) Three dimensional representation of main span length and total length histograms. (right) Aerial view of relationship between main span length and total length. The black line indicates a bridge length three times the main span length.

the black line. Because the majority of the bridges falls on the black line, 3SPC bridges with a total length three times the main span length will be considered candidates for the modeling portion of this study. In particular, we will consider 3SPC bridges with (a) 15-m main span length with 45-m total length and (b) 30-m main span length with 90-m total length, as these two combinations constitute roughly 18% of the 690 3SPC bridges.

A histogram of the year built for 3SPC bridges is shown in Fig. 2.5. Fig. 2.5 shows that the 3SPC bridge construction is concentrated between the 1970s and 2010s. In these six decades, the average is approximately 130 bridges, whereas the other decades have less than 10 bridges. This demonstrates that the use of 3SPC bridges in Oklahoma has been utilized widely over the last five decades.

2.3.2 Steel Girder Bridges

The number of main spans for Steel Girder bridges is shown in Fig. 2.6. Inspection of the graph indicates that the majority of the bridges possess one to five spans. Single-span bridges constitute 12% of the inventory, and multi-span bridges constitute the remaining 88% of the inventory. Moreover, it is observed that 56% of the bridges are
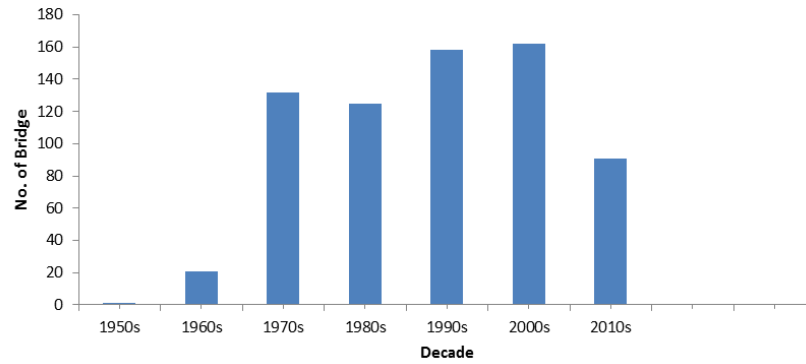
Figure 2.5: Year built histogram for Three-Span Prestressed Concrete Girder bridges.
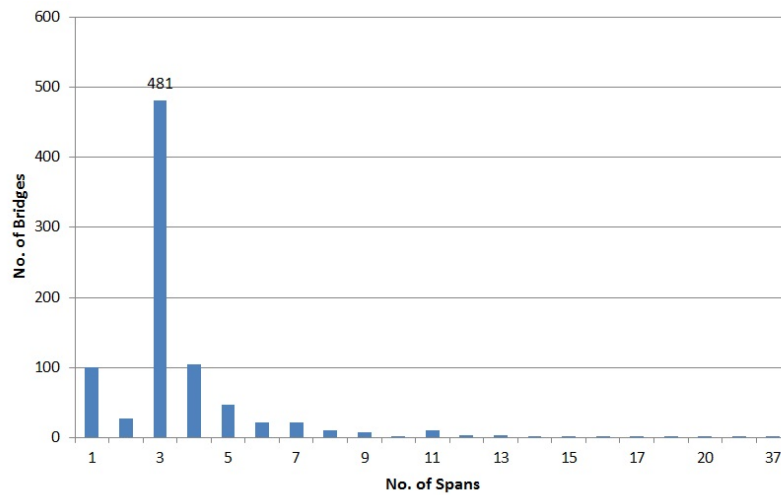
Figure 2.6: Number of spans histogram for Steel Girder bridges.

represented by three spans. As such, this study focuses on three-span Steel Girder bridges, hereinafter denoted 3SS bridges.

Figs. 2.7 and 2.8 display histograms of the main span length and bridge length, respectively. The main span length and total length data are binned in 1.5 m (5 ft.) and 4.5 m (15 ft.) increments, respectively. Although the data shows variation, there are some trends to highlight for the main span length and bridge length histograms.

For example, the largest groupings of main span length are concentrated at 12.2 m (40 ft.) and 15.25 m (50 ft.), while the predominant bridge lengths are concentrated at 36.58 m (120 ft.) and 45.72 m (150 ft.). Upon closer inspection of the predominant

24
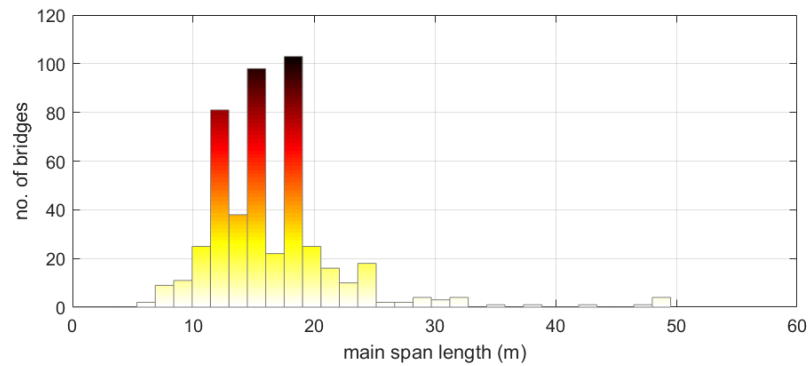
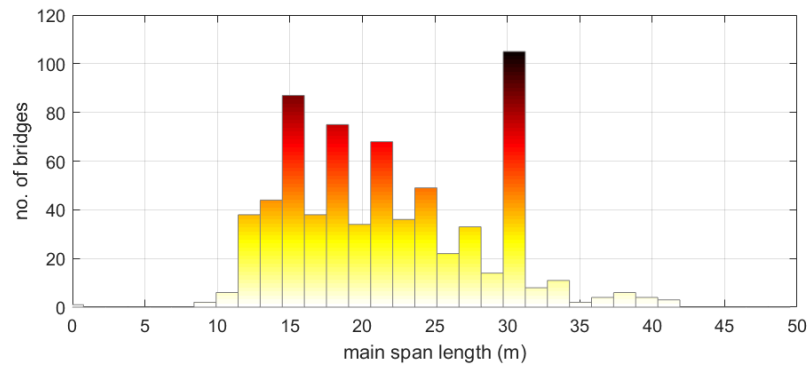**Figure 2.7:** Main span length histogram for Three-Span Steel Girder bridges.
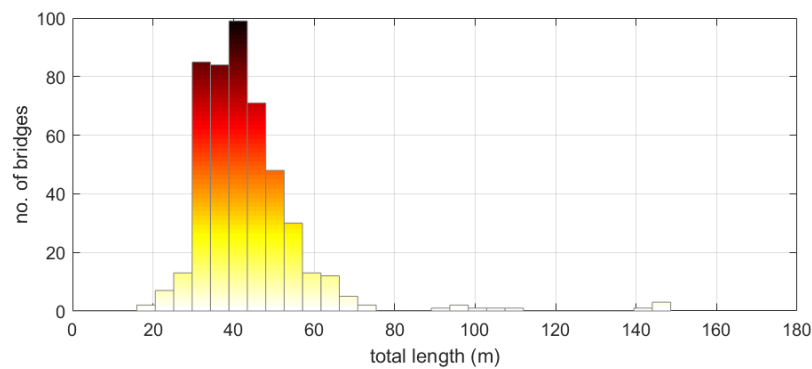
Figure 2.8: Bridge length histogram for Three-Span Steel Girder bridges.

main span lengths and bridge lengths, the bridge lengths are three times larger than the main span length, which for a three-span bridge would indicate equal span lengths.

The relationship between main span length and the bridge length with the number of bridges is represented in Fig. 2.9 (left). It is evident from Fig. 2.9 (right) that the bridge length is commonly equal to three times the main span length, as indicated by the black line. Because the majority of the bridges falls on the black line, 3SS bridges with a total length three times the main span length will be considered candidates for the modeling portion of this study. In particular, we will consider 3SS bridges with (a) 12-m main span length with 36-m total length and (b) 15-m main span length with 45-m total length, as these two combinations constitute nearly 20% of the 481 3SS bridges.

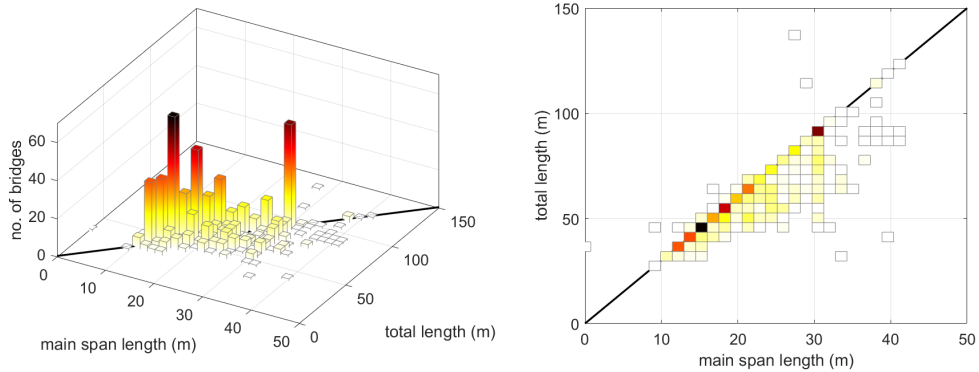Fig. 2.10 represents a histogram of the year built for 3SS bridges. 3SS bridge con-

Figure 2.9: Steel Girder Bridges: (left) Three dimensional representation of main span length and total length histograms. (right) Aerial view of relationship between main span length and total length. The black line indicates a bridge length three times the main span length.

Figure 2.10: Year built histogram for Three-Span Steel Girder bridges.

struction is concentrated between the 1930s and 1980s. In these six decades, the average looks to be around 90 bridges, whereas the other decades have less than 10 bridges. The number of bridges increases dramatically from the 1930s to 1940s, which marks the beginning of using 3SS bridges in highway systems. The histogram possesses noticeable peaks around 1940s and 1970s. However, the graph shows that the use of 3SS Girder bridges in Oklahoma has substantially decreased over the last three decades.

2.3.3 Continuous Steel Girder Bridges

The number of main spans for Continuous Steel Girder bridges is shown in Fig. 2.11. Assessment of the graph reveals that the majority of the bridges possess two to eight

26
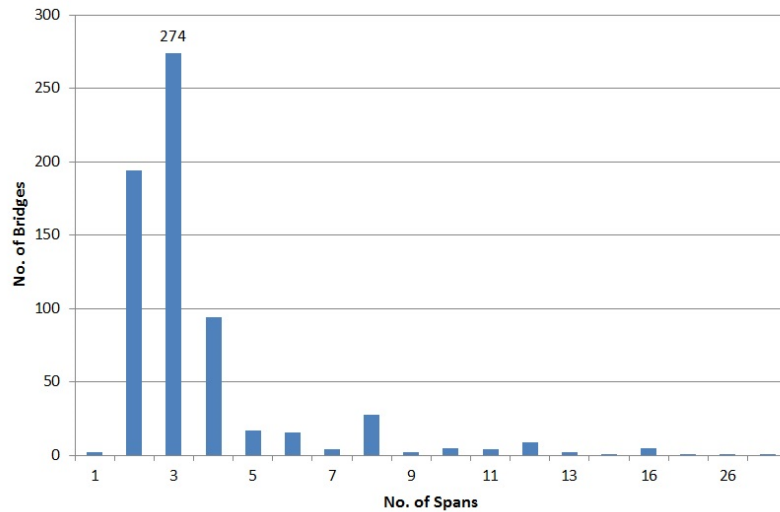
Figure 2.11: Number of spans histogram for Continuous Steel Girder bridges.

spans. Single-span bridges constitute 0.3% of the inventory, and multi-span bridges constitute the remaining 99.7% of the inventory. Moreover, it is observed that 40% of the bridges are represented by three-spans, while two spans represent 30.6%. As such, this study focuses on three-span Continuous Steel Girder bridges, hereinafter denoted 3SCS bridges.

Histograms for main span length and bridge length are showed in Figs. 2.12 and 2.13, respectively. As the same for the previous two bridge structure types, the main span length and total length data are binned in 1.5 m (5 ft.) and 4.5 m (15 ft.) increments, respectively. Although the main-span and bridge-length data display variation, there are still some trends to point out. For example, main span length is concentrated at 24.4 m (80 ft.), while the predominant bridge length is concentrated at 64.0 m (210 ft.). Upon closer inspection of the predominant main span lengths and bridge lengths, the bridge lengths are three times larger than the main span length, which for a three-span bridge would indicate equal span lengths.

The correlation between main span length and the bridge length with the number of bridges is represented in Fig. 2.14 (left). It is evident from Fig. 2.14 (right) that
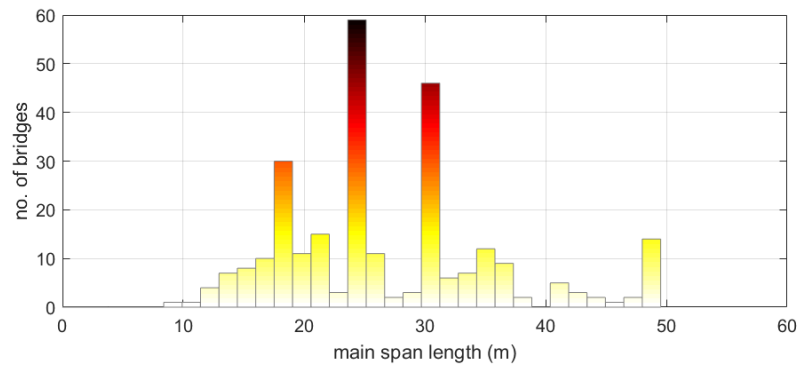
Figure 2.12: Span length histogram for Three-Span Continuous Steel Girder bridges.
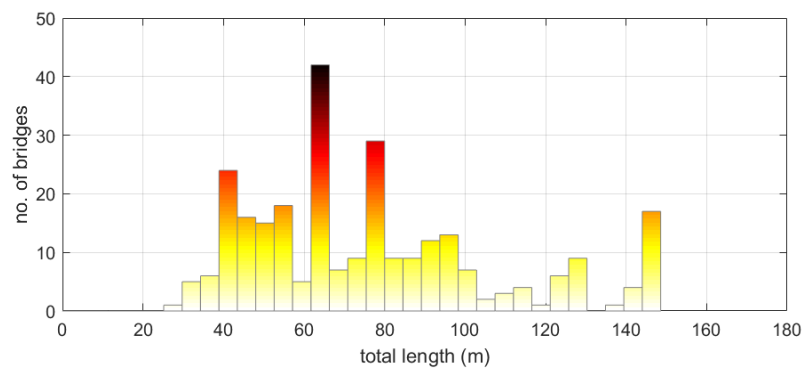
Figure 2.13: Bridge length histogram for Three-Span Continuous Steel Girder bridges.

the bridge length is commonly equal to three times the main span length, as indicated by the black line. 3SCS bridges with a total length three times the main span length will be considered candidates for the modelling portion of this study. In particular, we will consider 3SCS bridges with 24-m main span length with 64-m total length, as this combination constitutes roughly 14% of the 274 3SCS bridges.

Fig. 2.15 shows a histogram of the year built for 3SCC bridges. 3SCS bridge construction is concentrated between the 1960s and 1980s. In these three decades, the average is around 200 bridges, whereas other decades have less than 50 bridges. For this bridge structure type, the shape of the histogram increases promptly from the 1960s to 1970s and then decreases in the 1980s. The graph shows that the employment of 3SCS Girder bridges in Oklahoma has substantially decreased over the last three decades.

28
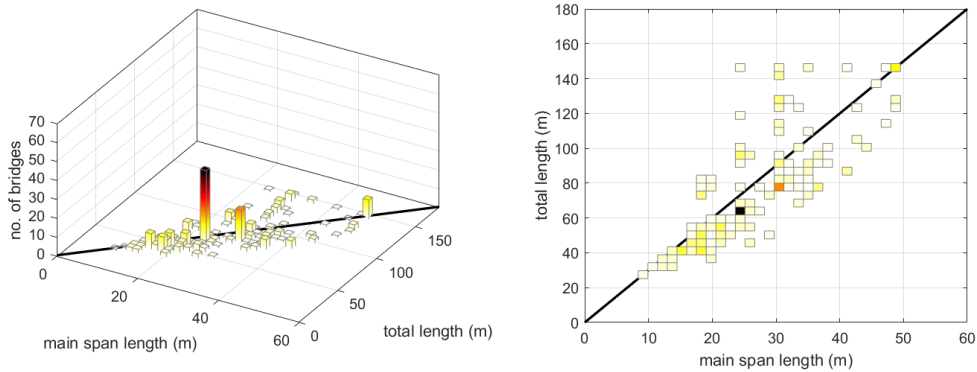
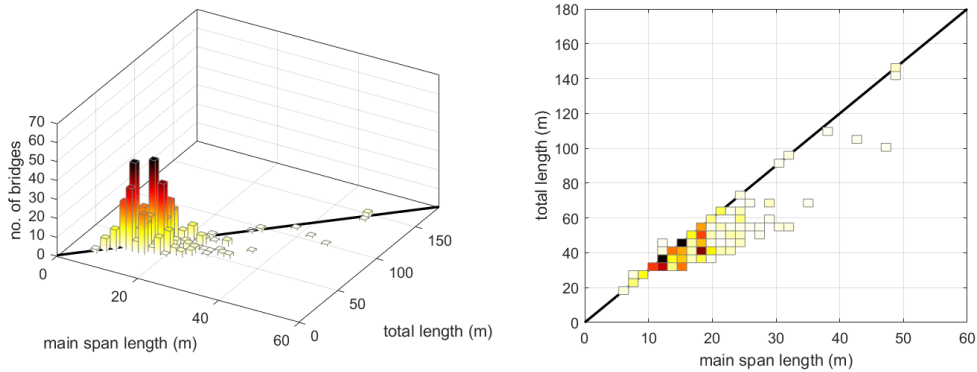**Figure 2.14:** Continue Steel Girder Bridges: (left) Three dimensional representation of main span length and total length histograms. (right) Aerial view of relationship between main span length and total length. The black line indicates a bridge length three times the main span length.
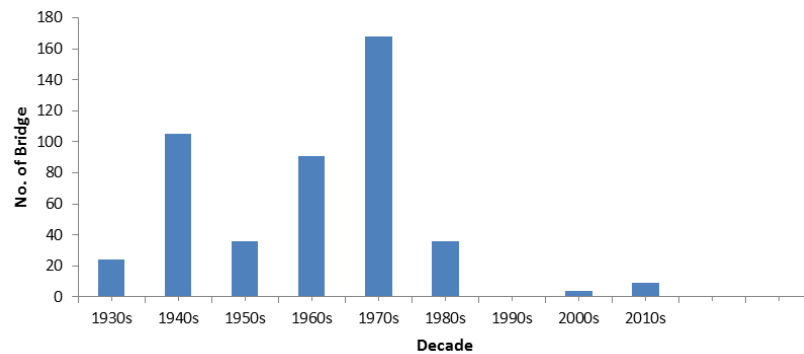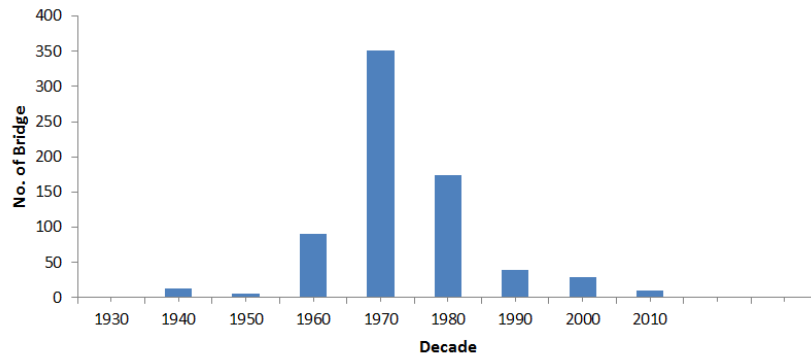

Figure 2.15: Year Built histogram for Three-Span Continuous Steel Girder bridges

2.4 Summary

After establishing the different series for main span length, bridge length and year built for each bridge structure type, three major bridge classes were found: Three-Span Prestressed Concrete Girder bridges, Three-Span Steel Girder bridges and Three-Span Continuous Steel Girder bridges. Fig. 2.16 indicates the locations of those bridges in the state of Oklahoma. From all the bridges shown in Fig. 2.16, the State Highway 99 (SH-99) bridge over Tiger Creek was selected for this study because it is representative of the most typical bridge class (3SPC girder bridge) and complete plans were available. The modeling is described in the following chapter.
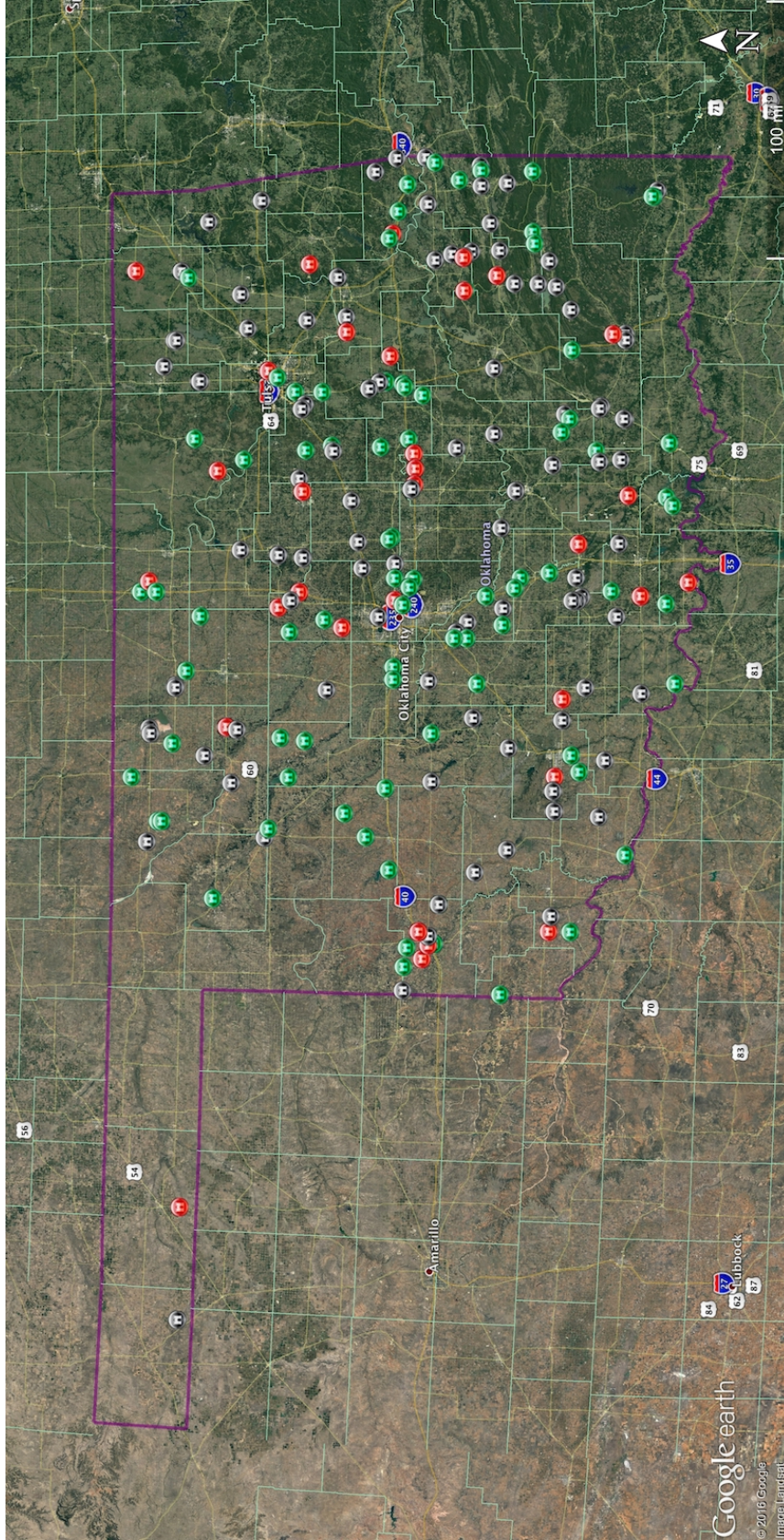
Figure 2.16: Location of proposed bridges for the different bridge classes: (grey) prestressed concrete girder bridges, (green) steel girder bridges, (red) continuous steel girder bridges.

30

Chapter 3

Analytical Model of a Typical Oklahoma Bridge

3.1 Overview

The designation of the typical Oklahoma bridge was taken in consideration previously, and the SH-99 bridge over Tiger Creek was selected. This chapter gives the details of the analytical model of the selected bridge and its components.

3.2 Bridge Layout

The SH-99 bridge over Tiger Creek is located northeast of Drumright, Oklahoma between Oklahoma City and Tulsa. Figs. 3.1 and 3.2 present topographical maps with the bridge location. The bridge is approximately 80 miles from Oklahoma City and 40 miles from Tulsa. Fig. 3.3 shows the plan and elevation of the SH-99 bridge over Tiger Creek. The bridge is comprised of two 50-ft $2^1/_2$-in. end spans and one 50-ft main span for a total length of 150-ft 5-in. The width of each span is 45-ft 5-in. and each span is constructed of five AASHTO type III prestressed concrete girders.

The girders for the end spans bear on a seat-type abutment at one end and a reinforced concrete (RC) two-column bent at the other, and the girders in the main span are supported by bents at each end. Fig. 3.4 shows the plan and elevation of the multi-

Figure 3.1: Location of the SH-99 bridge over Tiger Creek.
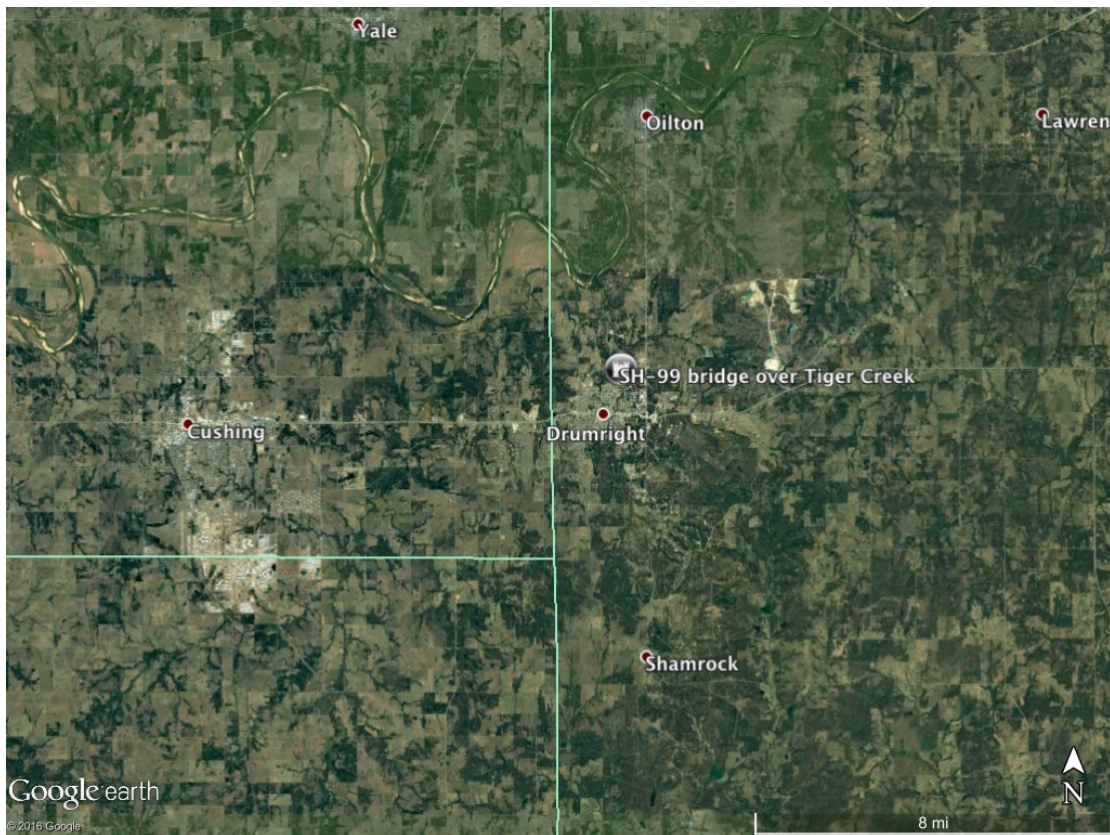
Figure 3.2: Detailed location of the SH-99 bridge over Tiger Creek.
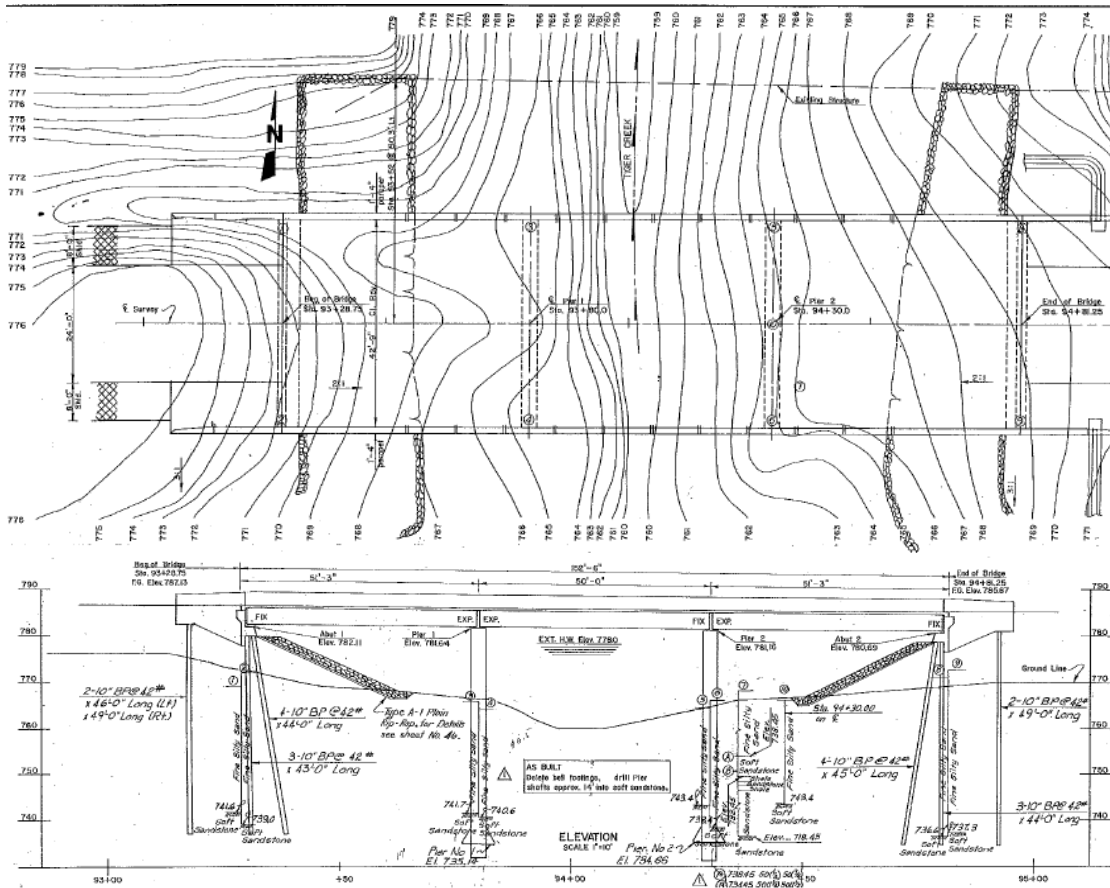
Figure 3.3: General plan and elevation of the SH-99 bridge over Tiger Creek. Taken from FAS Project No. R.S. 1910(103) plans.

column bent. The bent consists of a 3-ft wide by 4-ft 6-in. deep RC bent beam supported by two 36-in.-diameter circular RC columns which are made continuous to the drilled shaft by spiral reinforcement. Each 10-ft 6-in. column has 12-#9 reinforcing bars over the height of the column while 12-#10 reinforcing bars are used for the drilled shaft. The bent beam uses 20-#10, 19-#9, and 4-#4 reinforcing bars across the section while transverse steel is provided by #5 stirrups spaced at 9 in. on average. The design strength for the concrete is 4 ksi while the reinforcing steel has yield strength of 60 ksi.

Fixed-type and expansion-type bearings are used on this bridge. These bearings are composed of an elastomeric pad on which the ends of the girders rest and two anchor bolts set into the bent cap that are inserted through an anchor plate. A clearance hole is

used for fixed-type bearings, while a slot is used for expansion-type.

Both fixed-type and expansion-type bearings include a 20$\frac{1}{2}$-in. long by 7$\frac{1}{2}$-in. wide by $\frac{5}{8}$-in thick elastomeric pad with two 1$\frac{1}{4}$-in. diameter anchor bolts. For the fixed-type bearings, the bolts are inserted in 1$\frac{5}{8}$-in. diameter holes, while for the expansion-type the bolts are inserted in 3$\frac{5}{8}$-in. by 1$\frac{5}{8}$-in. slots.
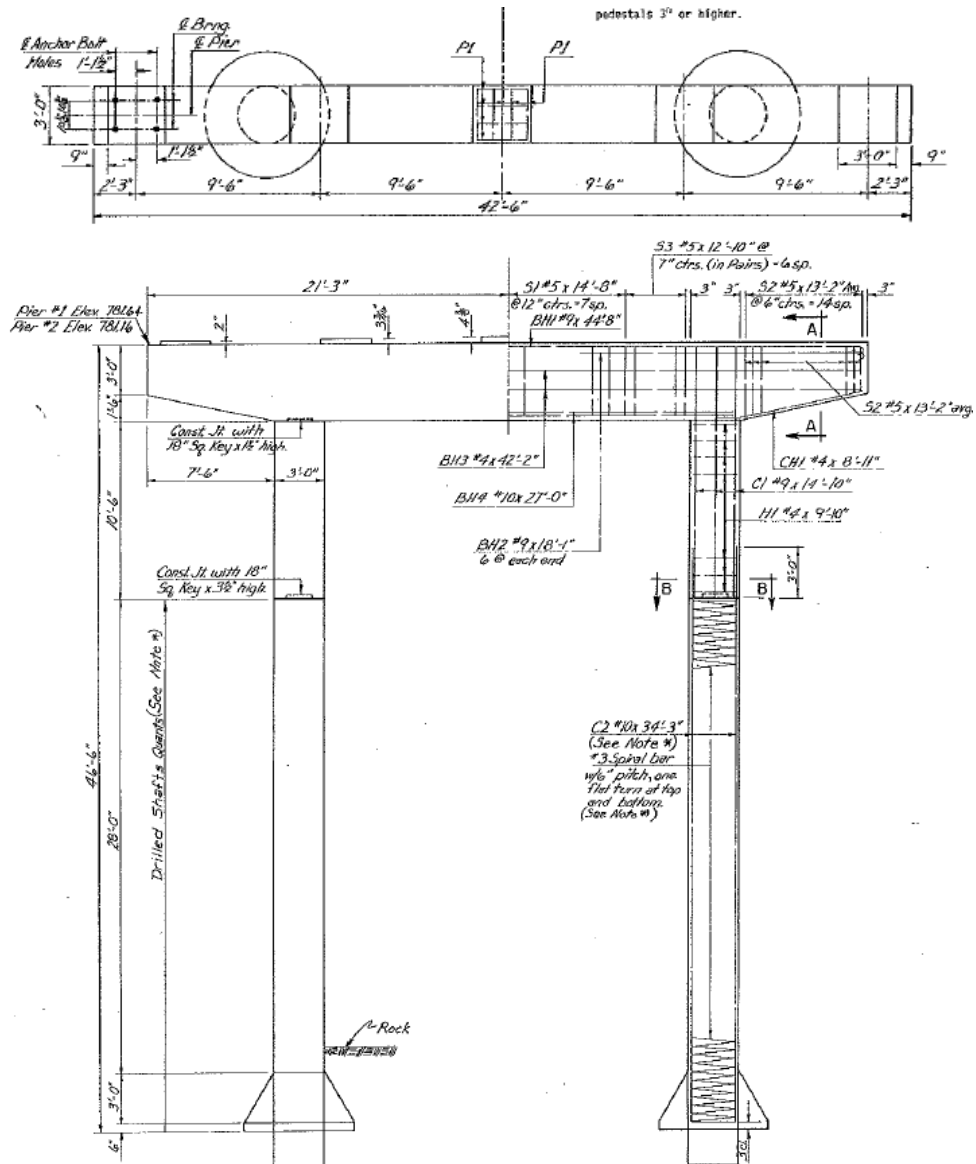
Figure 3.4: Plan and elevation of multi-column bent. Taken from FAS Project No. R.S. 1910(103) plans.

3.3 Analytical Models of Bridge Components

To generate the analytical bridge model with high degree of fidelity, a significant amount of detail in modeling the various bridge components is required. These components are classified into one of three main categories: (i) superstructure which consists of girders, deck slab, and parapets; (ii) substructure which consists of abutments, bents (beams and columns), footings, and foundations (drilled shafts); and (iii) bearings whose primary responsibility is to tie the superstructure to the substructure. The models of these bridge components are created in the analysis software *OpenSees*, which was initiated and is maintained by the Pacific Earthquake Engineering Research (PEER) Center (McKenna and Feneves, 2000). Fig. 3.5 depicts the node layout for the entire SH-99 bridge over Tiger Creek.
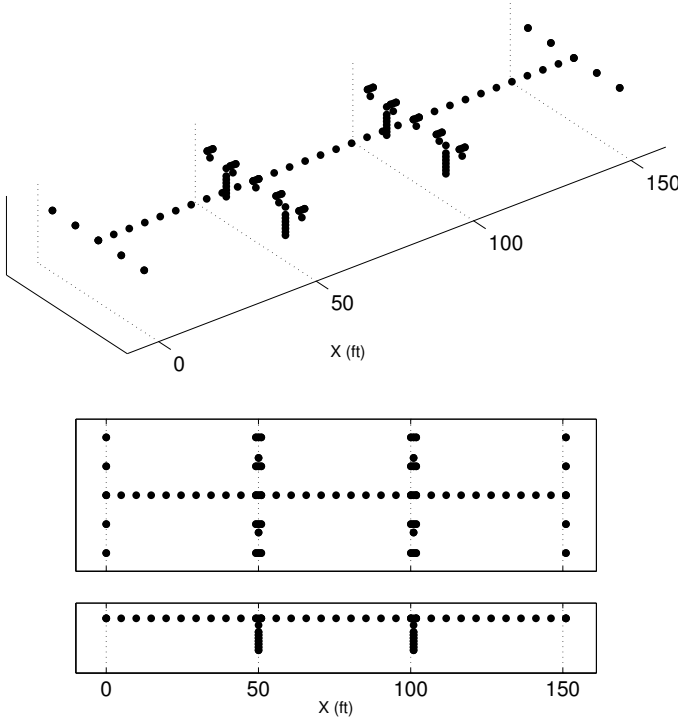
Figure 3.5: Nodes in the finite element model of the SH-99 bridge over Tiger Creek.

3.3.1 Bridge Superstructure

The superstructure of the bridge refers to the portion of the bridge located above the bearings, which consists of a set of girders with a thin concrete deck poured on top. The girders and deck operate in composite action, so the section properties of each span are calculated for the composite section of the girders and deck. The superstructure is expected to remain linearly elastic under seismic loading. Therefore, the superstructure elements were modeled in *OpenSees* by using elastic beam-column elements (*elasticBeamColumn*).

The superstructure details for the SH-99 bridge over Tiger Creek are shown in Figs. 3.6–3.8. The concrete deck (Fig. 3.6) is 7-¼-in. thick and 45-ft 5-in. wide and has an assumed density of 150 pcf. For 50-ft spans, prestressed concrete (PC) girders are represented by AASHTO type III (Fig. 3.8). The properties of the AASHTO type III girders are: height of 45 in., area of 560 in.^{2}, moment of inertia of 125×10^3 in.^{4}, weight of 0.0485 kip/in., and a distance from the bottom to neutral axis of girder of 20.27 in.

The section properties of each span were calculated for the composite section of the deck and girders. The properties, expressed with a modulus of elasticity of 3605 ksi, are as follows: area of 6751 in.^{2}, moment of inertia for the z (weak) axis of 1×10^6 in.^{4}, and moment of inertia for the y (strong) axis of 170×10^6 in.^{4}. The weight of the section is 0.58 kips/in.

Note that the girders are not continuous over the pier, but the deck is (Fig. 3.7). To represent the continuous deck, the 11-in. space between the center lines of the bearings was modeled using an elastic beam element with the following section properties (expressed with a modulus of elasticity of 3605 ksi): area of 3951 in.^{2}, moment of inertia for the z (weak) axis of 17×10^3 in.^{4}, and moment of inertia for the y (strong) axis of 97×10^6 in.^{4}.
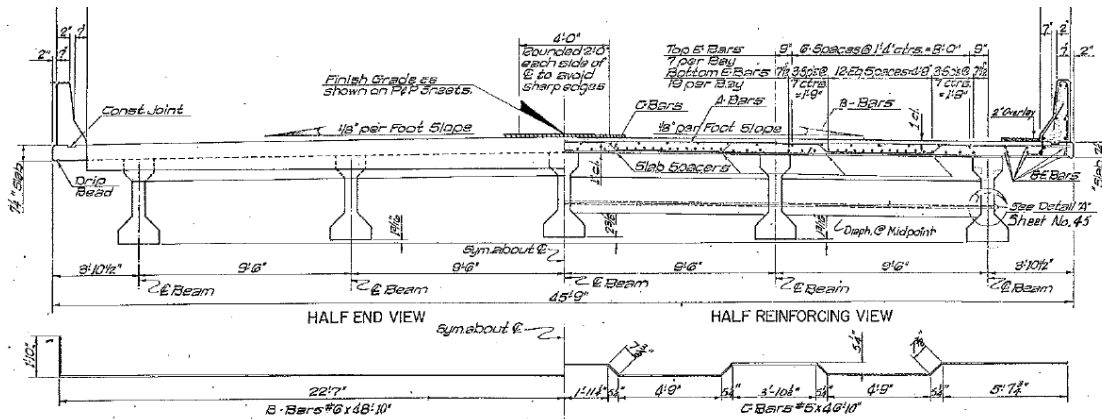
Figure 3.6: Superstructure typical cross section. Taken from FAS Project No. R.S. 1910(103) plans.
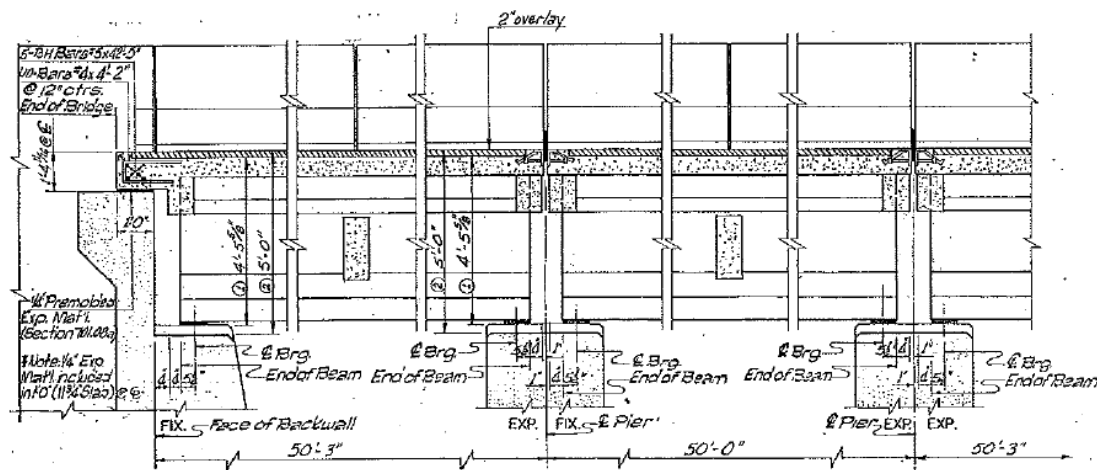
Figure 3.7: Superstructure longitudinal section. Taken from FAS Project No. R.S. 1910(103)) plans.

3.3.2 Bridge Substructure

The substructure of the bridge refers to the portion of the bridge located below the bearings. In general, this consists of bents (beams and columns), foundations, and abutments. The bents were modeled in detail for the finite element analysis of the bridge structure, but soil-structure interactions at the bottom of the columns were not modeled; i.e., fixed conditions were assumed at the top of the drilled shafts. The SH-99 bridge over Tiger Creek employs seat-type abutments; translational springs are considered to
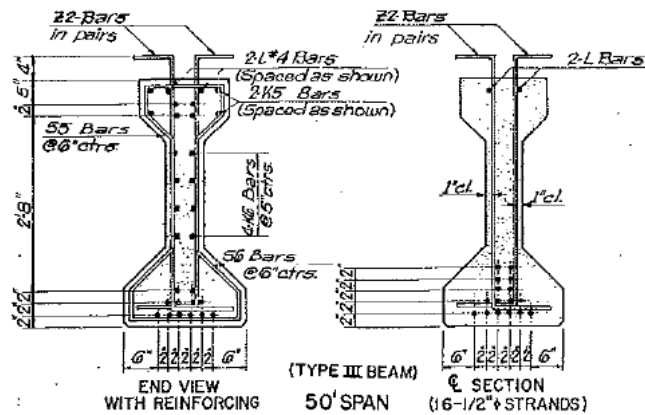
Figure 3.8: Superstructure girder details. Taken from FAS Project No. R.S. 1910(103) plans.

represent the soil (substructure method) which increases the fidelity of the model.

Multi-column Concrete Bents

Bridge piers (or bents) are substructure components which act as intermediate vertical and horizontal supports for bridge decks. In this case, the bridge bent configuration consists of two reinforced concrete columns which are supported on drilled shafts. The tops of the columns are joined by a reinforced concrete bent beam (pier cap), used to provide support for the bridge girders. Fixed conditions were assumed at the bottom of the columns (i.e., at the top of the drilled shaft / soil surface).

Analytical Modeling of Concrete Bents The concrete bents were modeled in *OpenSees* using a combination of displacement-based beam column elements (*dispBeamColumn*) and rigid links (*rigidLink*). The section properties for the columns and the bent beams were created using fiber elements with appropriate constitutive models for both the concrete and the steel reinforcement. Fiber elements allow the creation of a composite section which consists of different materials located at various spatial locations. Rigid links were used to connect the neutral axis of the bent to the top of the bent and to the columns.

Material Models   Reinforced concrete sections are constructed from three materials, namely unconfined concrete, confined concrete and reinforcing steel. The unconfined concrete behavior is modeled using the *Concrete01* material as provided in *OpenSees*. This material uses the Kent-Scott-Park model (Scott et al., 1982) which utilizes a degraded linear unloading/reloading stiffness and a residual stress. A concrete peak compressive stress of 4 ksi occurs at an associated strain $\epsilon_o = 0.002$.

The model for the confined concrete, which is inside the transverse reinforcing steel cage, is slightly different from that of the unconfined (cover) concrete. This is because the confinement of concrete by transverse reinforcement results in a significant increase in both the strength and ductility of compressed concrete (Mander et al., 1988). The maximum stress and associated strain for the confined concrete is given as $K f_c'$ and $\epsilon_o = 0.002K$ respectively, for which

$$K = 1 + \frac{\rho_s f_{yh}}{f_c'} \tag{3.1}$$

where f_c' is the unconfined compressive cylinder strength, ρ_s is the ratio of volume of steel hoops to volume of concrete core measured to the outside of the peripheral hoop, and f_{yh} is the yield strength of the steel hoops (Park et al., 1982).

For each column, the confinement reinforcement is provided by 11 hoops spaced at 12 in. The hoops are made of #4 bars with length 9 ft 10 in. with a 2-ft lap. Therefore, the volume of steel hoops is 18.8 in.^{3}. For a 36-in. diameter circular column, the volume of confined concrete is 8478 in.^{3} and the ratio of volume of steel hoops to volume of concrete core is $\rho_s = 2.22 \times 10^{-3}$, which results in a K value of 1.033. Therefore, the confined compressive strength and associated strain are equal to 4.13 ksi and 2.06×10^{-3}, respectively.

The reinforcing steel is assumed to have a yield strength $f_{ys} = 60$ ksi and an elastic modulus $E_s = 29,000$ ksi, and is modeled as an uniaxial bilinear steel material object

with kinematic hardening (*Steel01*). A strain hardening ratio of 0.018 was used for this material.

Analytical Model of Concrete Columns   The elements for the columns were generated using displacement beam-column elements (*dispBeamColumn*) that have an associated fiber section being representative of the true column section. Fiber elements allow the creation of a composite section which consists of different materials located at various spatial locations. The bridge bents use 36-in. diameter circular columns with vertical reinforcing bars. The vertical reinforcement consists of 12-#9 bars.

A moment-curvature analysis of the reinforced concrete section at the bottom of the column was performed. Given the geometry of a column section and reinforcement, the moment-curvature interaction diagram of a column section was determined. The nonlinear characteristics of a column section are affected by the axial force acting on the column; the axial force from dead load (230 kips) was used. The moment-curvature relation of a column section is shown in Fig. 3.9. The moment M_y and curvature ϕ_y at the first yielding, that is, when the vertical reinforcing bars reach the steel yield strength for the first time, are indicated in the figure, as well as the ultimate capacity M_u of a column section and corresponding curvature ϕ_u. Yield and ultimate moments and curvatures for the columns are given in Table 3.1.

Analytical Model of Concrete Bent Beam   The section for the concrete bent beam is created in the same way as for the circular columns; i.e., displacement beam-column elements with fiber sections. The bent beam is a rectangular section that is 36-in. wide by 54-in. tall and employs 20-#10, 19-#9, and 4-#4, grade 60 reinforcing bars. Non-

Table 3.1: Moment-curvature values for reinforced concrete columns.

P (kip)	M_y (10^3 kip-in.)	ϕ_y (10^{-6} 1/in.)	M_u (10^3 kip-in.)	ϕ_u (10^{-6} 1/in.)
230	15.4	106.0	20.5	528.0
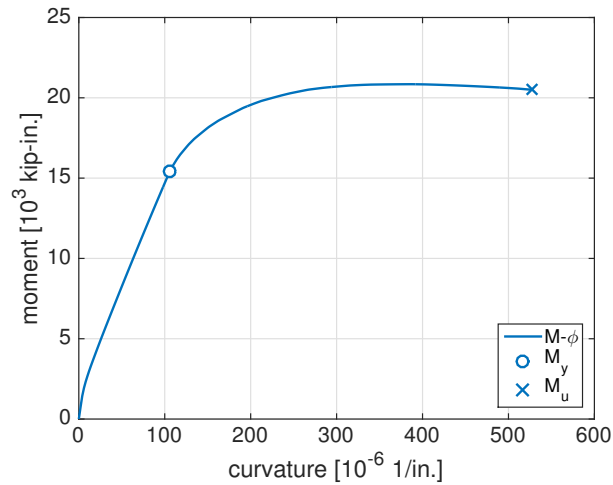
Figure 3.9: Moment-curvature relationship for reinforced concrete columns.

symmetric behavior of the beam is present due to the non-symmetric distribution of the reinforcing steel. It should be noted that this beam section was assumed for the entire length of the bent beam.

Seat-type Abutments

Abutments are vital components of highway bridges as they provide vertical support of the bridge superstructure at its ends and connect the bridge with the roadway approaches. Abutments also provide lateral restraint to the bridge superstructure when the bridge undergoes longitudinal and transverse loading. Under longitudinal loading, there are two types of resistance present: passive and active. Passive resistance develops as the abutment wall is pressed into the soil backfill, and active resistance develops as the abutment wall is pulled away from the soil backfill. Passive resistance is partially provided by the soil and partially provided by the piles, whereas active resistance is primarily provided by the piles. Under transverse loading, lateral resistance is provided solely by the piles.

Analytical Model of Seat-type Abutments   The seat-type abutments are modeled using linear springs based on the recommendations provided by Nielson (2005). For

longitudinal passive and active loading, total stiffness values of 962.70 kip/in. and 96.85 kip/in., respectively, are used for each of the abutments. These values are divided by 5 and assigned to the support for each of the girders. The abutment resistance in active loading is provided by 7 HP 10x42 piles in weak axis bending, while the passive resistance comes from piles in weak axis bending and the backfill granular soil. A total stiffness value of 282.47 kip/in. is used to model strong axis bending of 7 HP 10x42 piles for transverse loading. Again this value is divided by 5 and assigned to each girder support.

3.3.3 Bridge Bearings

A bridge bearing is a mechanical system that permits movement or transfers loads from the bridge superstructure to the substructure. Bearings are typically responsible for transmitting both vertical and horizontal loads to the substructure. The forces applied to a bridge bearing mainly include superstructure self-weight, traffic loads, wind loads and earthquake loads. They become a significant factor in the overall response and functionality of a bridge during and after seismic loading.

Elastomeric Bearings

Elastomeric bridge bearings are a common bearing used on concrete girder and slab type bridges. These types of bearings consist of an elastomeric rubber pad and anchor bolts for restraint that are embedded into the pier cap and project through steel plates attached to the underside of the girder. Each component of the bearing system provides a distinct contribution in the transfer of forces. The elastomeric pad transfers horizontal load by developing a frictional force while the anchor bolts provide resistance through a beam type action. Models of the pad and the anchor bolts are developed separately and then combined in parallel to get the appropriate composite action.

Fig. 3.10 presents the bearing dimensions for the SH-99 bridge over Tiger Creek.

Each bearing consists of a 70-durometer elastomeric pad that is 7½-in. wide by 20½-in. long and ⅝-in. thick. Two 1¹⁄₄-in. diameter anchor bolts are inserted into 3⅝-in.-by-1⅝-in. slots (expansion bearings) or 1⅝-in. diameter holes (fixed bearings) through anchor plates attached to the underside of the girder.
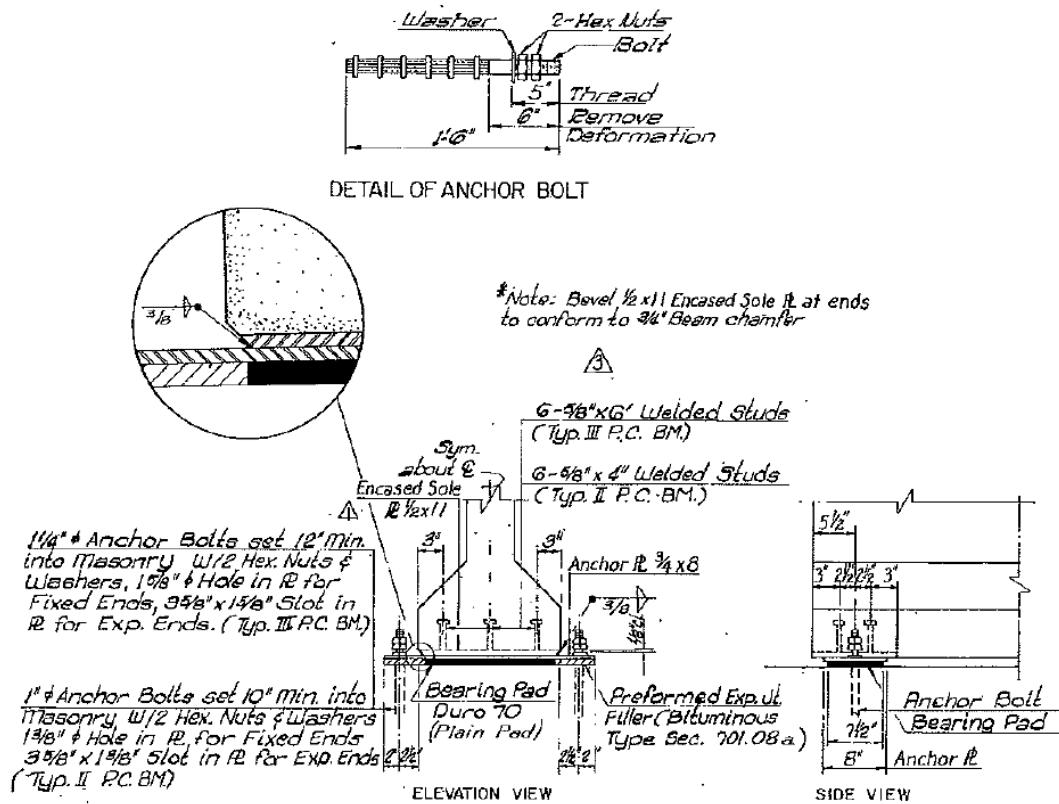
Figure 3.10: Elastomeric bearing details. Taken from PCB-42.75-3 plans.

Elastomeric Pad   The behavior of the elastomeric pad is characterized by sliding; the modeling of the elastomeric pad was accomplished by using a *Steel01* material in *OpenSees*. The *Steel01* material is used to construct a uniaxial bilinear steel material object with kinematic hardening described by a non-linear evolution equation. The initial shear stiffness of the bearing and also the calculation of an appropriate coefficient of friction are fundamental values that should be determined for modeling of the elastomeric pad. The initial stiffness k_o can be calculated as follows (Schrage, 1981):

43

$$k_o = \frac{GA}{h_r} \tag{3.2}$$

where A is the area of the elastomeric bearing, G is the shear modulus of the elastomeric pad and h_r is the thickness of the elastomeric pad. The elastomeric pads are 70 durometer, for which the shear modulus G is in the range 200–300 psi; a value of 245 psi was assumed.

The frictional coefficient for concrete bridges takes into account the interface between the elastomeric rubber and a concrete surface. Schrage (1981) showed that the coefficient of friction for an elastomeric bearing is a function of the normal stress on the bearing, σ_m, and is given by

$$\mu = 0.05 + \frac{0.4}{\sigma_m} \tag{3.3}$$

where μ is the coefficient of friction and σ_m is the normal stress on the bearing given in MPa. The normal force N on each bearings was found to be 34.5 kips. Table 3.2 presents the normal stress σ_m on each bearing, as well as the corresponding coefficient of friction μ and yield force $F_y = \mu N$.

Anchor Bolts   The anchor bolts are used to prevent excessive movement between the girders and the piers, on which they bear. Each girder requires two anchor bolts at each end. The anchor bolts are embedded into the top of the concrete pier cap and project out and through anchor plates attached to the underside of the girder. Under working loads the response of these anchor bolts is expected to remain linear. However, for moderate earthquakes, a non-linear behavior is expected.

Table 3.2: Elastomeric bearing pad properties for the SH-99 bridge over Tiger Creek.

Location	A (in.^{2})	h_r (in)	k_o (kip/in)	σ_m (psi)	μ	F_y (kip)
End and Main Spans	154	$^5/_8$	60.27	225	0.308	10.65

In work performed by Vintzeleou and Tassios (1987), it was shown that there is extreme pinching in the hysteresis when a dowel is loaded as a cantilever, as is the case for elastomeric-type bearings. There was also an obvious drop off in strength as the dowels fractured. In order to construct in *OpenSees* a uniaxial bilinear hysteretic material object with pinching of force and deformation, as well as, damage due to ductility and energy, we estimated the yield strength F_y and ultimate strength F_u of a $1^1/4$-in. diameter anchor bolt acting in cantilever action with $^5/_8$-in. length. For a single bolt, the estimated yield and ultimate strengths are given in Table 3.3 and are approximately 31.5 and 32.0 kips, respectively. The yield deformation δ_y was taken to be 0.05 in. and the deformation δ_u at failure to be 0.10 in.

Analytical Model of Expansion-type Elastomeric Bearings The composite behavior of an elastomeric bridge bearing was achieved by combining the behavior of the elastomeric pad and two anchor bolts in parallel. The elastomeric pad was represented and modeled in *OpenSees* by using a *Steel01* material with an initial stiffness k_o and yield force F_y given in Table 3.2. The anchor bolt behavior was modeled in *OpenSees* by using a *Hysteretic* material with points of the envelop given in Table 3.3.

For the expansion bearings, the slot allows a total of $^3/_8$ in. of transverse movement and $2^3/_8$ in. of longitudinal movement without initiating the effects of the anchor bolts. This condition is simulated by placing a $^3/_{16}$-in. transverse gap and $1^3/_{16}$-in. longitudinal gap on each side of the hysteresis; this gap is represented in *OpenSees* by using an elastic-perfectly plastic gap material (*ElasticPPGap*).

Table 3.3: Anchor bolt parameters for the SH-99 bridge over Tiger Creek.

Location	$\varnothing$ (in.)	F_y (kip)	δ_y (in.)	F_u (kip)	δ_u (in.)
End and Main Spans	$1\frac{1}{4}$	31.5	0.05	32.0	0.10
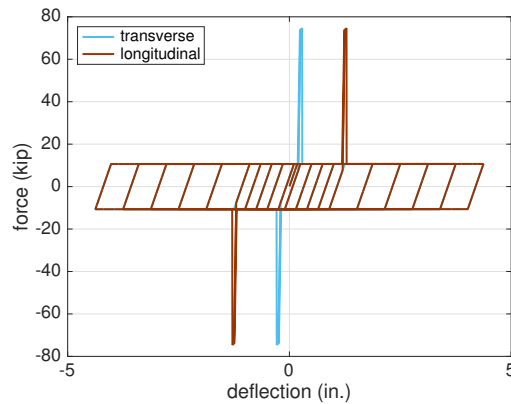
Figure 3.11: Transverse and longitudinal force-deflection relationships for elastomeric bearings.

Analytical Model of Fixed-type Elastomeric Bearings   For the fixed bearings, the hole allows a total movement of ⅜ in. in transverse and longitudinal direction without initiating the effects of the anchor bolts. This condition is simulated by placing a ³⁄₁₆-in. transverse and longitudinal gap on each side of the hysteresis; this gap is represented in *OpenSees* by using an elastic-perfectly plastic gap material (*ElasticPPGap*).

3.4   Modal Properties

The modal properties of bridges are a useful way to classify their general characteristics. An eigenvalue analysis of the SH-99 bridge over Tiger Creek using *OpenSees* extracted the first 50 natural periods and accompanying mode shapes. Fig. 3.12 shows these periods.

The analysis reveals that the bridge's fundamental (1st) period is approximately 0.296 seconds with the predominant motion being in the longitudinal direction. This mode shape is presented in Fig. 3.13 and confirms the longitudinal nature of this mode. The deck moves in a rigid-body mode, without significant bending in the columns being activated.

The 2nd mode is another rigid-body mode with predominant motion being in the transverse direction (Fig. 3.14). Like the 1st mode, significant bending in the columns
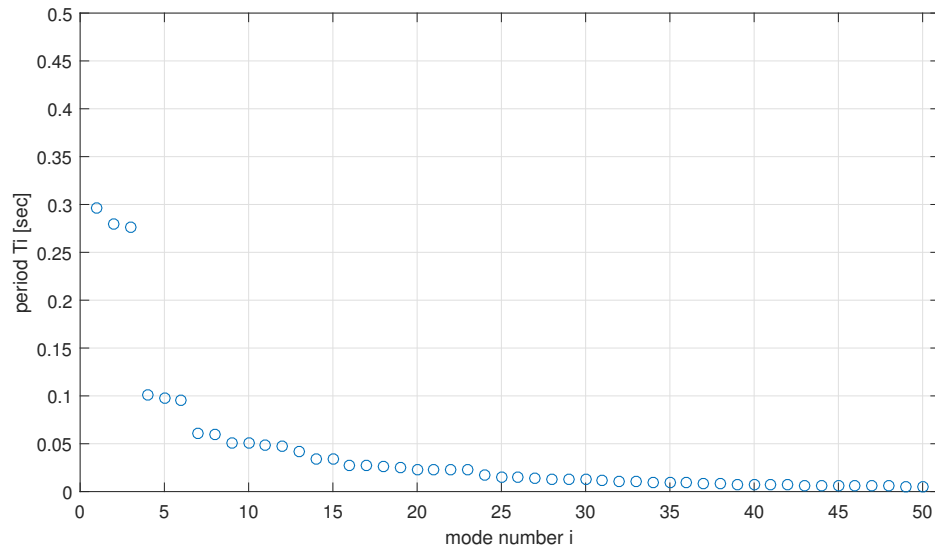
Figure 3.12: First 50 natural periods of SH-99 bridge over Tiger Creek.

is not activated. The 3rd mode is a rigid-body mode with rotation being the predominant motion (Fig. 3.15). The 6th mode is a flexural mode (Fig. 3.16). In addition to flexure in the deck, bending in the columns is activated as well.

3.5   Summary

A three-dimensional finite element model for the SH-99 bridge over Tiger Creek was generated using the analysis software *OpenSees*. The model was developed to integrate a high degree of fidelity in the major bridge components (e.g., bearings and columns) that were to be used as damage indicators. For the elastomeric bearings, deflections limits in terms of engagement and failure of the anchor bolts were established; for the reinforced concrete columns, first-yield and ultimate capacities were determined. An eigenvalue analysis was performed and indicated that the fundamental modes were dominated by longitudinal and transverse rigid-body motion.
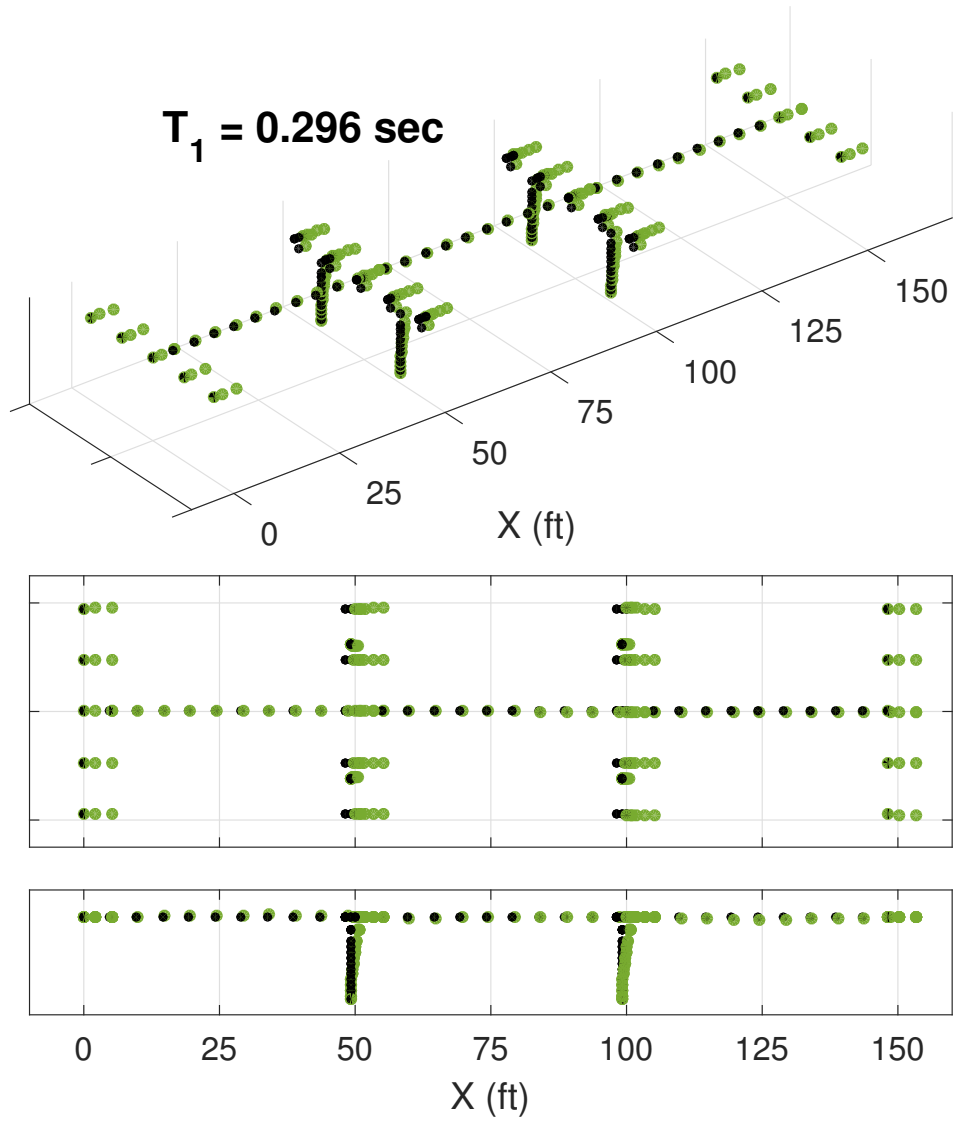
Figure 3.13: 1st mode of SH-99 bridge over Tiger Creek.
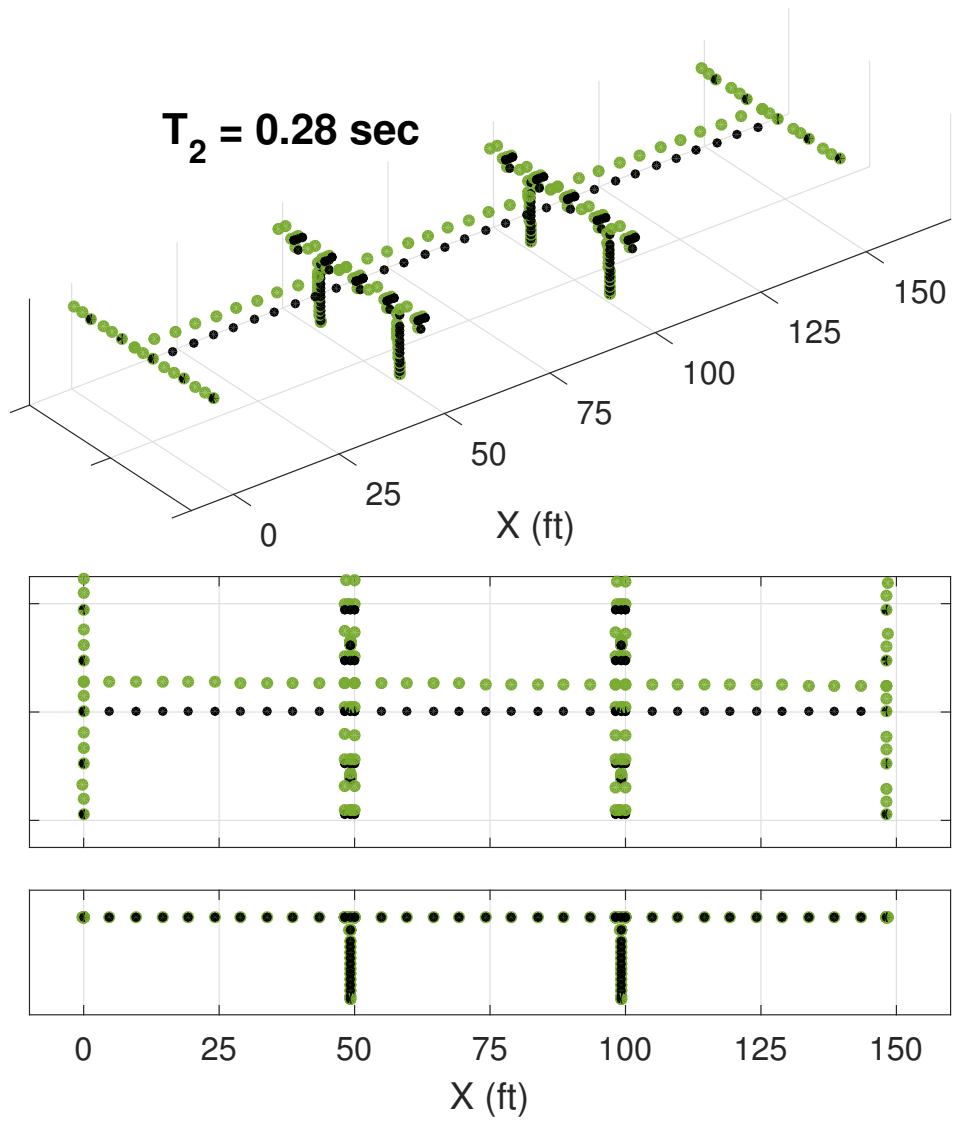
Figure 3.14: 2nd mode of SH-99 bridge over Tiger Creek.
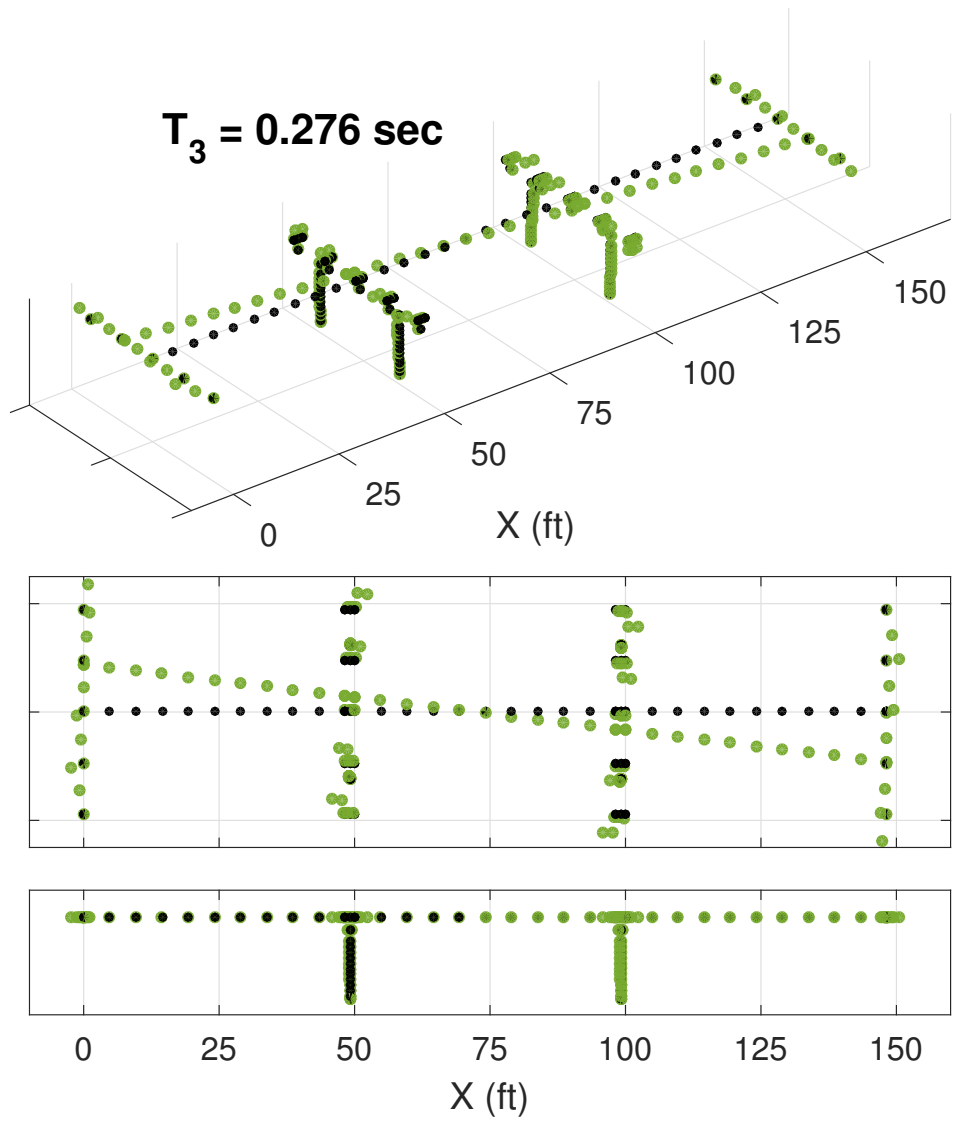
Figure 3.15: 3rd mode of SH-99 bridge over Tiger Creek.
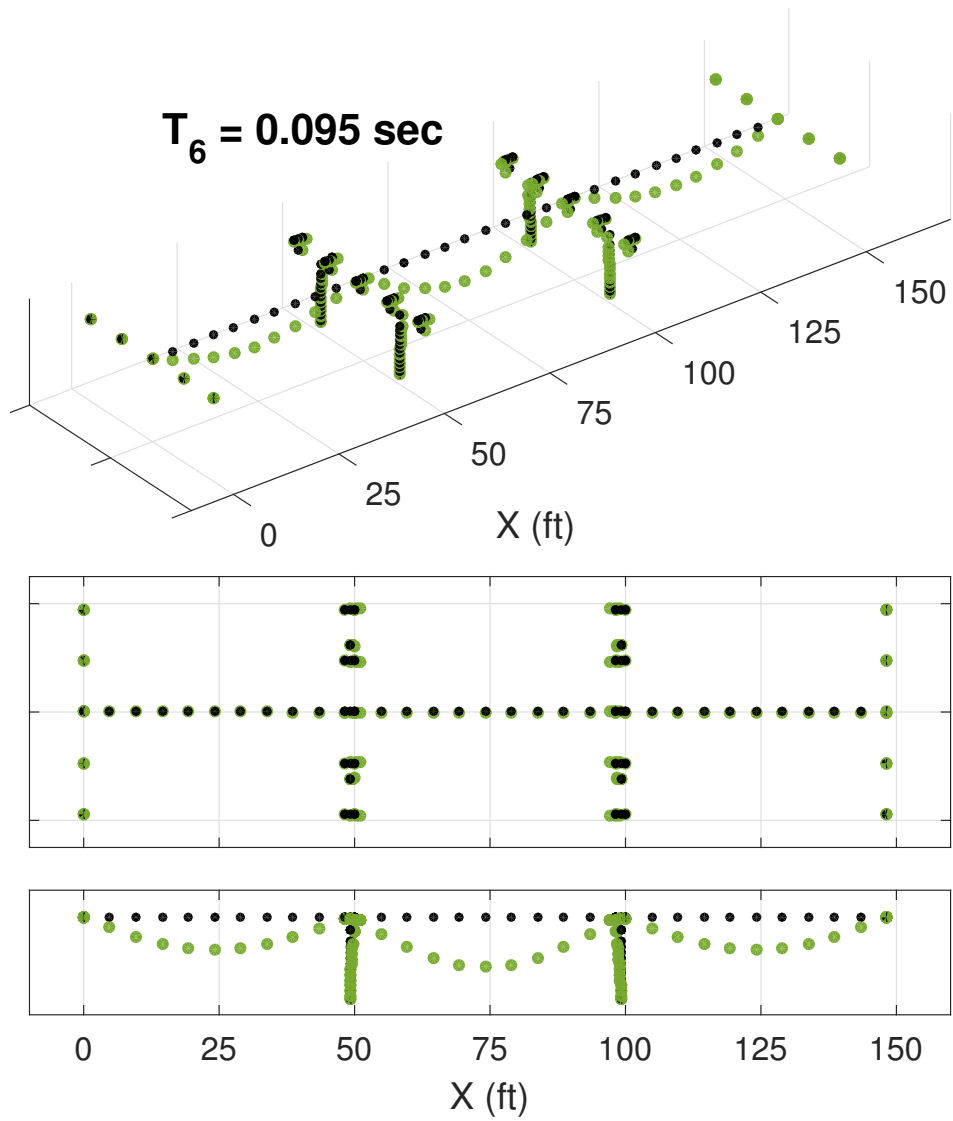
Figure 3.16: 6th mode of SH-99 bridge over Tiger Creek.

Chapter 4

Oklahoma Ground Motions

4.1 Overview

In the preceding two chapters, the typical Oklahoma bridge was identified and modeled. Now, the seismic demand on Oklahoma bridges needs to be characterized. To indicate the actual seismic hazard in Oklahoma, this chapter will focus on the latest earthquake events in the region.

4.2 Oklahoma Seismicity

Over the decade leading up to September 2016, Oklahoma experienced roughly 70 magnitude (M) 4.0 or larger events (USGS, 2016d). Two of these events were larger than M 5.0. The first one was the M 5.7 earthquake near Prague, Oklahoma on November 6, 2011, and the second was the M 5.1 earthquake near Fairview, Oklahoma on February 13, 2016. Both of these events were felt broadly across Oklahoma as well as the surrounding states. The Prague earthquake was felt in 17 states, causing damage in residential constructions and 2 injuries. The Fairview earthquake did not cause significant damage, as it was lower in magnitude.

On September 3, 2016, Oklahoma experienced its largest earthquake on record: a M 5.8 near Pawnee, Oklahoma. The Pawnee earthquake occurred at a depth of 5.6 km with its epicenter located at a latitude and longitude of 36.4251°N and 96.9291°W.
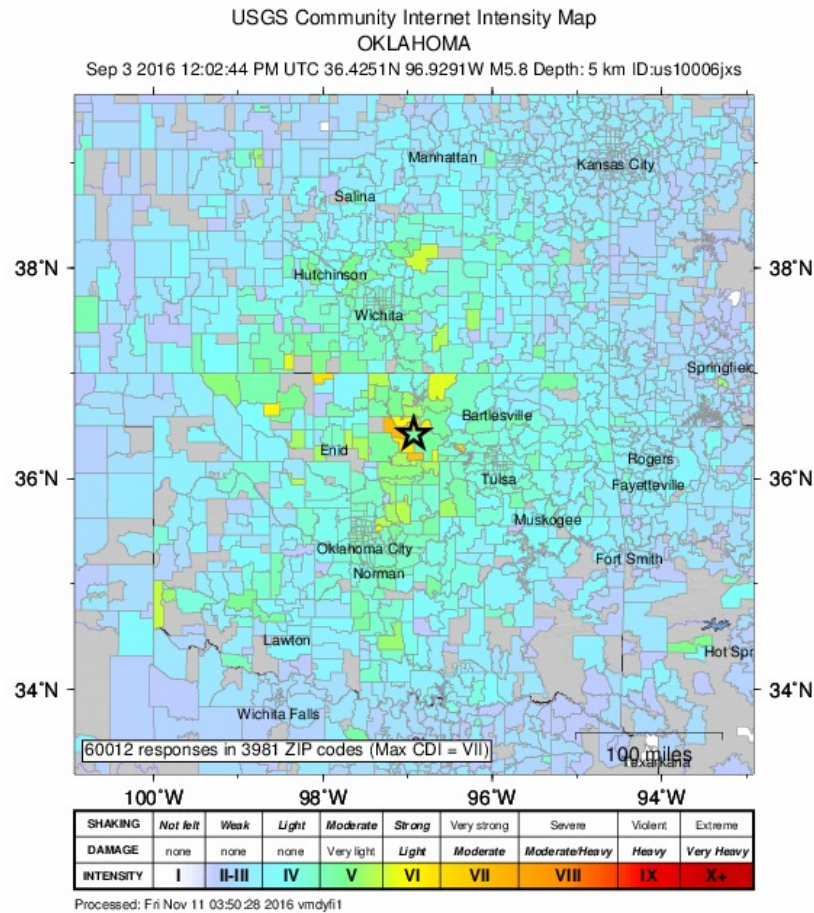
Figure 4.1: Intensity map for M 5.8 Pawnee earthquake.

The event was felt in 7 states and produced damage to historical buildings located in Pawnee and adjacent towns. Figure 4.1 shows an intensity map for the event created from information collected from people who felt the earthquake (USGS, 2016b).

As of November 7, 2016, Oklahoma has experienced 4 earthquakes equal and above M 5.0. Because the probability of earthquakes with higher magnitudes has surpassed the forecast, the present study uses seismic station data recorded during the largest Oklahoma earthquake (the September 3, 2016 earthquake near Pawnee) as ground motions for time-history analysis of the typical Oklahoma bridge.

Figure 4.2: Seismic stations and their proximity to the M 5.8 Pawnee earthquake epicenter.

4.2.1 Seismic Stations

Ground motions were obtained for all stations within 120 km of the M 5.8 Pawnee earthquake. A total of 28 stations were identified. Fig. 4.2 shows the identified stations and their locations relative to the earthquake epicenter. Table 4.1 presents a list of these stations, their locations and soil conditions (Vs30), as well as which channels are used. Biaxial ground motions are considered, so both the East and North components were retained, but the vertical components were not included. Note that one station that was identified, OK.GORE, was omitted from this study because its data was inconsistent and potentially corrupted.

4.2.2 Ground Motions

Fig. 4.3 show the response spectra for the 27 seismic stations that registered the Pawnee earthquake. The spectral acceleration reported is the largest radial acceleration:

$$S_a(T) = \max_t \sqrt{[a_1(t;T)]^2 + [a_2(t;T)]^2}$$

54

where $a_1(t; T)$ and $a_2(t; T)$ are the acceleration responses in two orthogonal horizontal directions, in this case East and North, for a structure with period T. This is an orientation-independent measure of the spectral acceleration, as opposed to the geometric mean of the response spectra in the two directions (Boore et al., 2006). The largest spectral accelerations are observed at periods between 0.05 and 0.3 seconds. There is variation in the spectra at different sites because the stations were located at

Table 4.1: All stations selected for ground motion data.

Station	Epicentral Distance (km)	Latitude	Longitude	Vs30 (m/s)	Channel East	Channel North
GS.KAN01	109.6	37.1534	-97.7590	245.1	HNE	HNN
GS.KAN05	113.3	37.1087	-97.8723	254.0	HNE	HNN
GS.KAN09	100.1	37.1361	-97.6183	263.4	HNE	HNN
GS.KAN13	81.6	37.0129	-97.4778	216.0	HNE	HNN
GS.KAN14	109.6	36.9568	-97.9630	234.1	HNE	HNN
GS.KAN17	101.4	37.0441	-97.7647	236.5	HNE	HNN
GS.KS20	105.3	37.2297	-97.5543	247.9	HN2	HN1
GS.KS21	115.9	37.2865	-97.6630	258.0	HN2	HN1
GS.OK005	88.7	35.6549	-97.1911	330.2	HNE	HNN
GS.OK009	103.7	35.5813	-97.4229	319.0	HNE	HNN
GS.OK011	106.6	35.4852	-96.6858	268.0	HNE	HNN
GS.OK025	100.6	35.5811	-97.3379	278.5	HH2	HH1
GS.OK029	84.3	35.7966	-97.4549	342.2	HN2	HN1
GS.OK030	56.7	35.9278	-96.7838	317.4	HN2	HN1
GS.OK031	53.0	35.9531	-96.8391	287.2	HN2	HN1
GS.OK033	42.3	36.0444	-96.9382	311.9	HN2	HN1
GS.OK034	50.0	36.0102	-96.7132	273.7	HN2	HN1
NQ.KAN15	112.8	37.2998	-97.5727	240.4	HNE	HNN
NQ.OK914	51.6	35.9708	-96.8048	273.6	HNE	HNN
NQ.OK915	54.2	35.9535	-96.7726	329.7	HNE	HNN
NQ.OK916	84.6	36.8073	-97.7477	204.3	HNE	HNN
OK.BCOK	105.0	35.6567	-97.6093	264.8	HHE	HHN
OK.BLOK	45.2	36.7606	-97.2150	243.4	HHE	HHN
OK.CHOK	96.6	35.5611	-97.0613	285.6	HHE	HHN
OK.CROK	94.9	36.5047	-97.9834	296.9	HHE	HHN
OK.DEOK	75.4	35.8427	-96.4983	281.4	HHE	HHN
OK.QUOK	34.5	36.1714	-96.7080	335.4	HHE	HHN
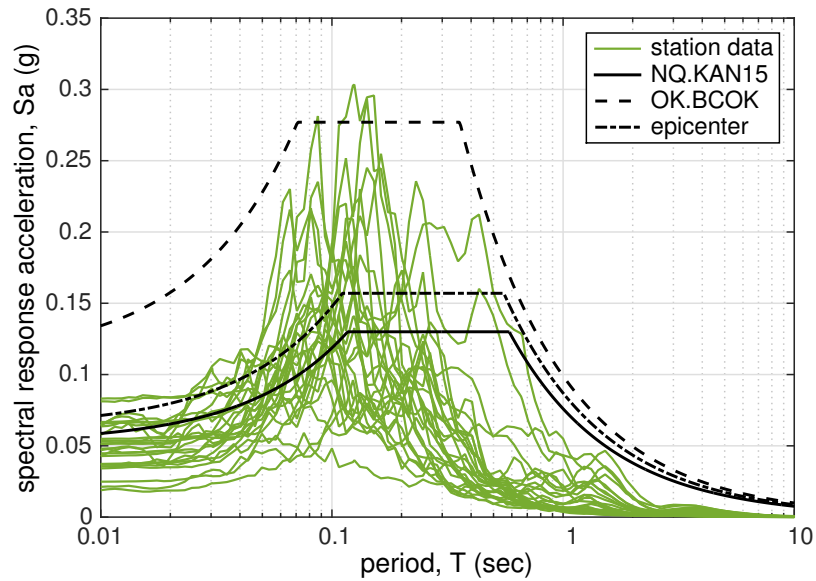
Figure 4.3: Spectral response acceleration S_a measured at all 27 stations, including the 2009 AASHTO Specifications Design Response Spectra at three sites: smallest design S_a (NQ.KAN15), largest design S_a (OK.BCOK), and at the M5.8 epicenter.

varying distances from the epicenter (Table 4.1).

4.2.3 Comparison to AASHTO Design Standards

Fig. 4.3 shows the spectral acceleration from each station compared to the AASHTO design response spectra (AASHTO, 2009). For the sake of clarity, design spectra are shown for only three locations: the smallest design values (NQ.KAN15), the largest design values (OK.BCOK), and at the epicenter of the Pawnee event. The design curves are based on the hazard from Meers fault in Southwest Oklahoma. This means that the design curves are larger closer to the fault (OK.BCOK) and smaller farther from the fault (NQ.KAN15). However, as can be seen from Fig. 4.3, this does not necessarily correspond to the intensity of the ground motions from the earthquake. Fig. 4.4 shows that the station OK.BCOK displays a spectral acceleration curve far below its design curve while in Fig. 4.5 the design curve and measured spectrum more closely match, with the measured S_a exceeding the design value at a period of about 0.15 s. Note that
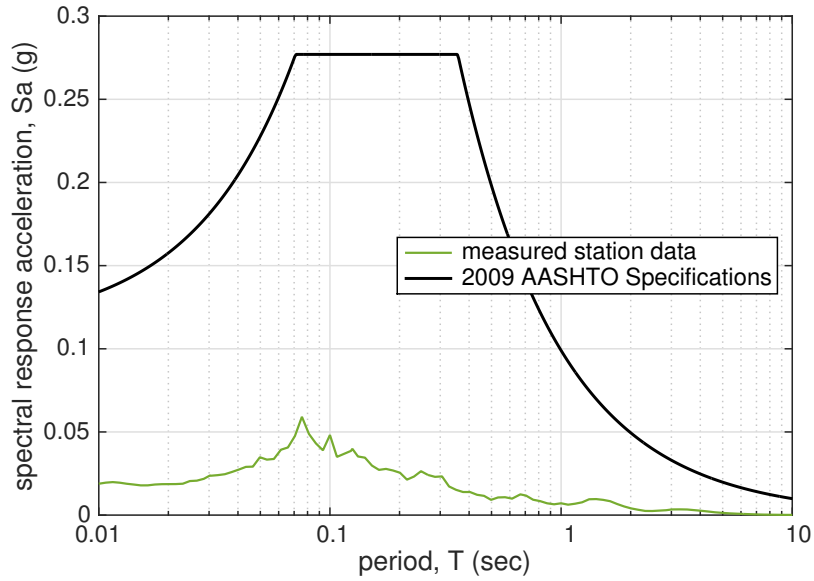
Figure 4.4: Spectral acceleration from station OK.BCOK
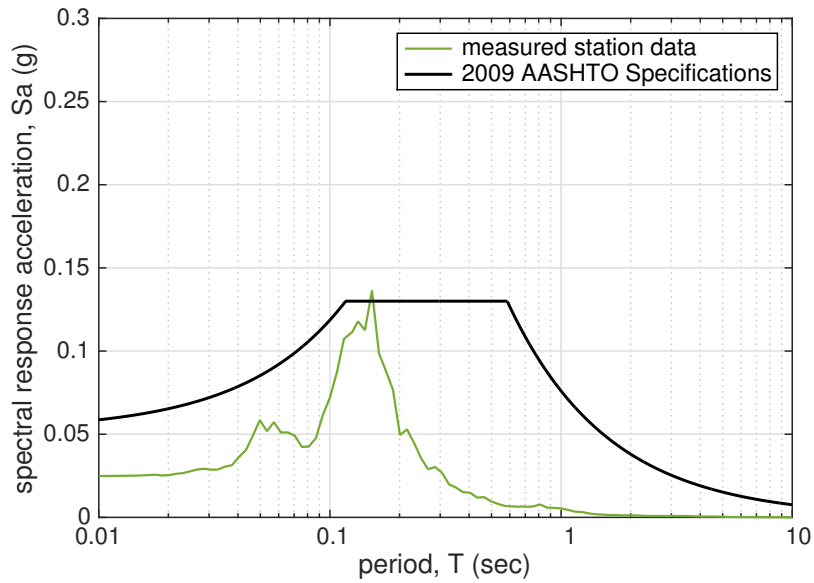
Figure 4.5: Spectral acceleration from station NQ.KAN15

there are stations between NQ.KAN15 and OK.BCOK that are closer to the epicenter but farther from Meers fault than OK.BCOK, such as GS.OK005; these stations would have design curves between OK.BCOK and NQ.KAN15 but larger measured spectra.

4.3 Summary

Seismic station data collected during the largest earthquake to date (the M 5.8 Pawnee earthquake) was used to generate a suite of 27 bidirectional ground motions that will be applied in time-history analyses of the typical Oklahoma bridge in the following chapter. Spectral response accelerations determined from the measured ground motions were compared to design spectra; in some cases the measured spectral responses exceeded the design values, especially at short periods (0.1 – 0.3 sec).

Chapter 5

Seismic Response Analysis — Measured Ground Motions

5.1 Overview

As part of the seismic response analysis, transient time-history bridge responses were calculated for the suite of 27 ground motions (GMs) presented in the previous chapter. The analytical model of a typical Oklahoma bridge (Chapter 3) was subjected to these bidirectional ground motion records. Two bridge orientations were considered for each GM: North-South (NS) and East-West (EW). Hence, a total of 54 numerical simulations were performed. The response of the columns and bearings were recorded, and the results are reported here. Maximum responses of key bridge components (bearing deflections and column curvatures) are presented, from which conclusions on the state of the bridge are drawn.

5.2 Damage States for Seismic Response Analysis

Past experiences have shown that the vulnerabilities of bridges during earthquakes are mainly due to damage to critical components, such as columns and bearings. For example, large relative movements at the expansion joints may result in the loss of support and excessive ductility demands on bridge piers may result in column failure in flexure.

Hence, estimating the capacity of bridge components is essential for determining the risk of damage to structural components and the entire structure. With the definition of qualitative damage (limit) states (Table 1.1), the next task is to assign a quantitative measure to each of the limit states for each of the bridge components. Capacity limit states for as-built components from Nielson (2005) are described below and will be used when appropriate and modified otherwise.

5.2.1 Flexural Capacity of Concrete Columns

There are different metrics which are available for defining the limit states of the RC columns, including drift, displacement ductility μ_Δ, and curvature ductility μ_ϕ. The metric chosen for this study is curvature ductility which is defined as

$$\mu_\phi = \frac{\phi_{\max}}{\phi_y} \tag{5.1}$$

i.e., the maximum realized curvature divided by the yield curvature or curvature at yield of the outer most steel reinforcing bar.

Nielson (2005) developed limit states using a Bayesian approach, whereby physics-based ("prescriptive") and survey-based ("descriptive") information was combined. The prescriptive approach used values adapted from Hwang et al. (2000). Hwang et al. (2000) proposed limit states, in terms of displacement ductility, of 1.0, 1.2, 1.76 and 4.76 which correspond to yield, cracking, spalling and reinforcement buckling[*], respectively. These limit states are defined in terms of displacement ductility, so Nielson (2005) translated them into equivalent curvature ductilities for typical RC columns in the Central and Southeastern United States, which are given in Table A.1 (Appendix A). The descriptive approach used survey data from Padgett and DesRoches (2007) where bridge inspectors and officials were asked to describe the functionality of a bridge for

---

[*]The *Seismic Retrofitting Manual for Highway Bridges* (FHWA, 1995b) notes that, for poorly confined columns, longitudinal steel will buckle at a displacement ductility of 3.0, which is thus the value chosen by Nielson (2005).

different levels of component damage. Following a Bayesian updating procedure, the limit states for the columns were modified, resulting in the limit states listed in Table A.2. In this study, we will use the prescriptive values for the column limit states, which are, in general, slightly conservative and are given in Table 5.1.

5.2.2 Deflection Capacity of Elastomeric Bridge Bearings

Nielson (2005) used the same Bayesian approach to define the limit states for elastomeric bearings. The behavior of the elastomeric bearings is one which is controlled by sliding. Unrestricted sliding can only occur once a fracture of the steel retention dowels (anchor bolts) occurs. For the prescriptive information, Nielson (2005) assumed a deformation of 1.18 in. for slight damage, 3.94 in. for moderate damage, 5.91 in. for extensive damage, and 10.0 in. for complete damage. These values correspond to noticeable deformation without significant closure, need for realignment with possible dowel fracture, need for some degree of repair (girder retention) with assured dowel fracture and additional deck realignment, and unseating of girder, respectively. These values were then updated using survey data (Table A.2).

The slot dimensions for the expansion elastomeric bearings detailed by Nielson (2005) differ from those on the SH-99 bridge over Tiger Creek. On the SH-99 bridge over Tiger Creek, the slot allows for ±0.1875 in. of deflection transversely and ±1.875 in. of deflection longitudinally. According to the anchor bolt model, yielding and failure of the bolt will occur, respectively, at 0.05 in. and 0.10 in. beyond engagement of the slot. Therefore, the values for slight damage determined by Nielson (2005) have been modified to be better representative of the SH-99 bridge over Tiger Creek. These limit state values are given in Table 5.1.

Note that Nielson (2005) considered dowels encased in the elastomeric pads, for which "it is difficult, if not impossible, for a bridge inspector to recognize this fracture or to differentiate between the fixed and expansion bearings." Therefore, Nielson (2005)

Table 5.1: Limit states for bridge components used in this study. Adapted from Nielson (2005).

Component	Slight	Moderate	Extensive	Complete
REINFORCED CONCRETE COLUMN				
curvature ductility μ_ϕ	1.00	1.58	3.22	6.84
FIXED-TYPE ELASTOMERIC BEARING				
longitudinal deflection (in.)	0.24	3.58	5.60	7.68
transverse deflection (in.)	0.24	3.58	5.60	7.68
EXPANSION-TYPE ELASTOMERIC BEARING				
longitudinal deflection (in.)	1.92	4.10	5.36	7.35
transverse deflection (in.)	0.24	3.58	5.60	7.68

assumed that the limit states for the fixed and expansion elastomeric bearings, in both the longitudinal and transverse directions, are the same. This is not the case for the bearings use on the SH-99 bridge over Tiger Creek, as reflected in Table 5.1.

5.3 Seismic Evaluation of Bridge Bearings

Fig. 5.1 shows the peak bearing deflections due to the 27 GMs for a bridge oriented NS and a bridge oriented EW. The bearing deflections are plotted versus the GMs' spectral acceleration at 1.0 s. The bridge has five bearings per abutments and ten bearings per pier, or 30 points per GM and orientation. Similar trends are observed for bridges oriented NS and ones oriented EW, but slightly larger bearing deflections are observed for the NS-oriented bridge, in general.

From Fig. 5.1, it is noticeable that the GMs recorded at station GS.OK005 produce the largest bearing deflection. Figs. 5.2 and 5.3 present representative force-deflection responses for GMs recorded at station GS.OK005 for a bridge oriented NS and EW, respectively. The deflections in the East and North direction, d_E and d_N, respectively, are shown, along with the corresponding forces F_E and F_N. Fig. 5.2 shows that the maximum deflection for an elastomeric bearing is 0.13 in., while Fig. 5.3 displays a maximum deflection of 0.10 in. In both cases, the maximum deflection occurs in the EW direction due to a larger EW component to the GM at this site. Recalling that the gap between the anchor bolt and the hole or slot is $^3/_{16}$ in., the response remains linear which indicates that the bolts were not activated due to the deflection; i.e., all motion was in the bolt hole or slot of the bearing.

5.4 Seismic Evaluation of Concrete Columns

Fig. 5.4 shows the peak column curvatures due to the 27 GMs for a bridge oriented NS and a bridge oriented EW. The column curvatures are plotted versus the GMs' spectral
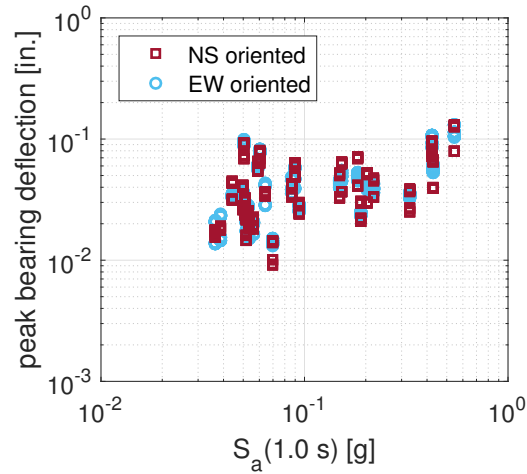
Figure 5.1: Peak bearing deflection for a bridge oriented NS and a bridge oriented EW.

acceleration at 1.0 s. This bridge has two columns per pier, or 4 points per GM and orientation, and display similar trends to the peak bearing deflections (Fig. 5.1). Futhermore, for Fig. 5.4, the GMs recorded at station GS.OK005 produce the largest column curvature. Contrary of what its seen in Fig. 5.1, for Fig. 5.4 larger column curvatures are observed for the EW-oriented bridge, in general.

The moment-curvature response for GMs recorded at station GS.OK005 for a bridge oriented NS and EW are shown in Figs. 5.5 and 5.6, respectively. Fig. 5.5 shows that the maximum column curvature is 13.65×10^{-6} 1/in., while Fig. 5.6 displays a maximum column curvature of 14.26×10^{-6} 1/in. It can be seen, that curvature ϕ_N about the North (N) is the largest, corresponding to a column drift in the East (E) direction, which matches the predominant bearing deflections.

The yield curvature of the columns is 106.0×10^{-6} 1/in. Compared to this yield limit, the predicted curvatures for NS- and EW-oriented bridges are very small (13.5% of yield). This is to be expected because the inertial loads from the deck are not transmitted to the bent because the bearing pads are quite flexible.
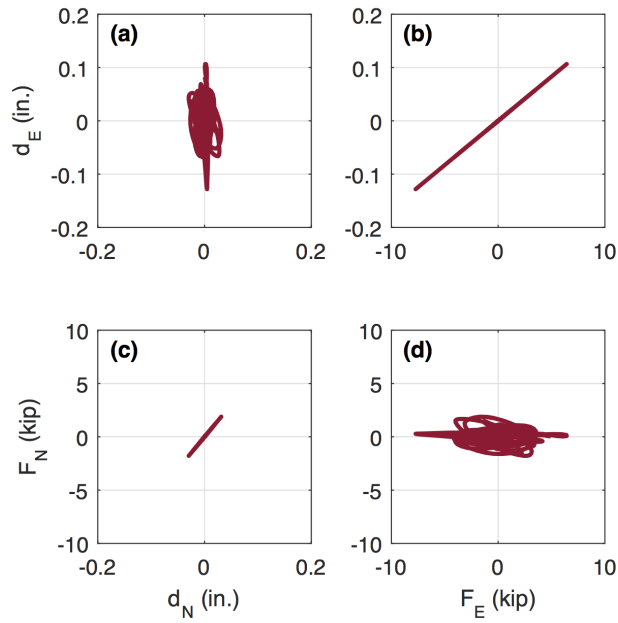
Figure 5.2: Force-deflection response of elastomeric bearing for GMs recorded at station GS.OK005 for a bridge oriented NS: (a) d_E vs. d_N (b) d_E vs. F_E (c) F_N vs. d_N and (d) F_N vs. F_E.
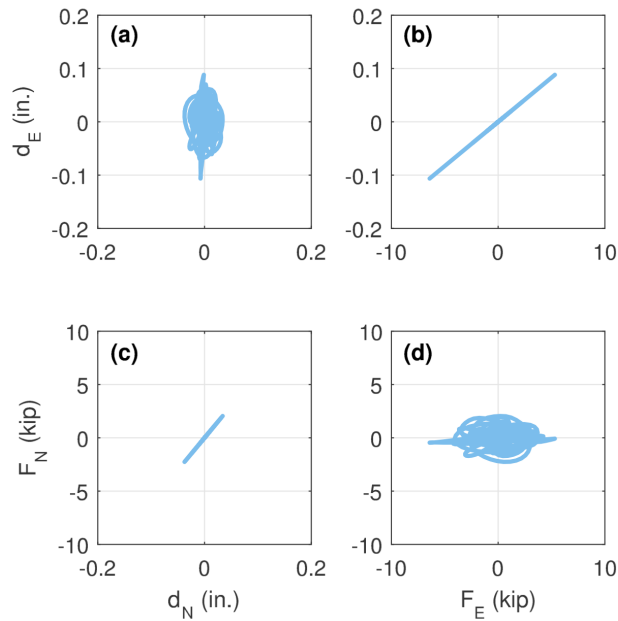
Figure 5.3: Force-deflection response of elastomeric bearing for GMs recorded at station GS.OK005 for a bridge oriented EW: (a) d_E vs. d_N (b) d_E vs. F_E (c) F_N vs. d_N and (d) F_N vs. F_E.
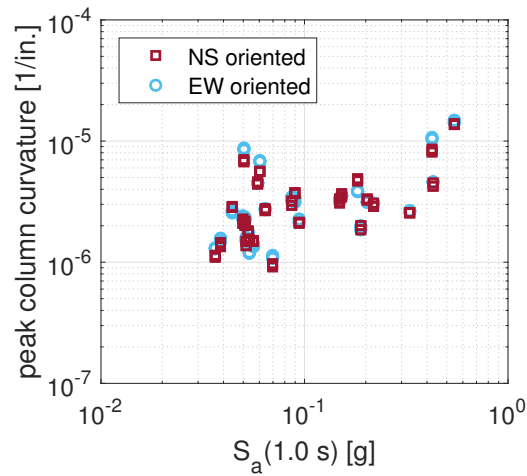
Figure 5.4: Peak column curvature for NS and EW orientation.

5.5 Summary

The detailed finite element model of the SH-99 bridge over Tiger Creek was used to conduct a bidirectional seismic response analysis. The analysis indicated that (a) the maximum bearing deflection (0.13 in.) is seen for a bridge oriented NS; and (b) the maximum column curvature is observed for a bridge oriented EW and is about 13.5% of the yield curvature. From the analysis, station GS.OK005 was identified as having the largest responses. In the following chapter, the ground motions from station GS.OK005 will be scaled to assess the response of the typical highway bridge to higher accelerations.
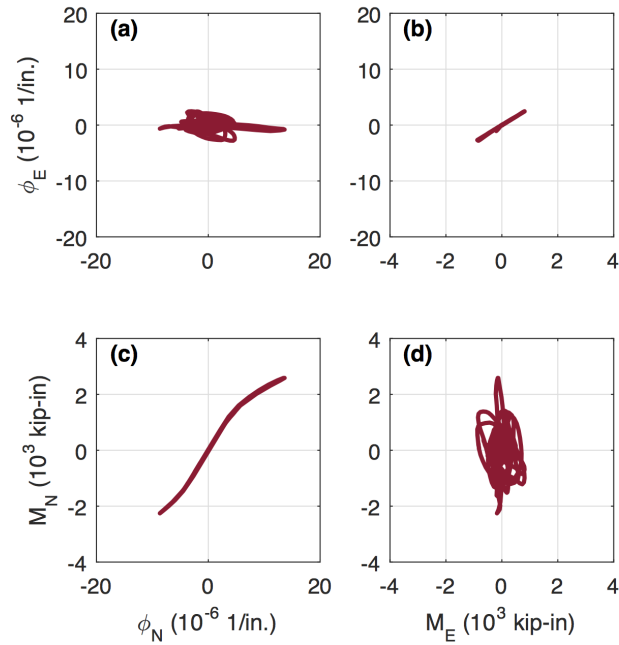
Figure 5.5: Moment-curvature response of a column for GMs recorded at station GS.OK005 for a bridge oriented NS: (a) ϕ_E vs. ϕ_N (b) ϕ_E vs. M_E (c) M_N vs. ϕ_N and (d) M_N vs. M_E.
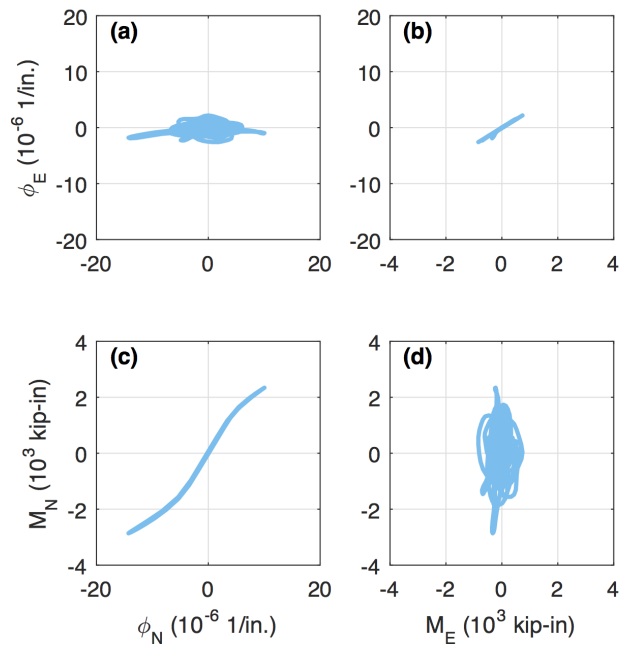
Figure 5.6: Moment-curvature response of a column for GMs recorded at station GS.OK005 for a bridge oriented EW: (a) ϕ_E vs. ϕ_N (b) ϕ_E vs. M_E (c) M_N vs. ϕ_N and (d) M_N vs. M_E.

Chapter 6

Seismic Response Analysis — Scaled
Ground Motions

6.1   Overview

In Chapter 5, unscaled, recorded ground motions (GMs) were used to assess the seismic response of a typical Oklahoma bridge to the M 5.8 Pawnee event. Small bearing deflections and column curvatures were observed. This chapter will explore the response of the bridge through *incremental dynamic analysis* by scaling one of the recorded GMs to match design values as well as observed ground-motion intensities. In particular, the bidirectional GM records from station GS.OK005 are used. Fig. 6.1 shows the measured GM records in the NS and EW directions. The peak ground accelerations for both orientations are seen at around 30 sec, and the peak ground acceleration (Fig. 6.1(b)) is about $0.8g$. It is evident that the accelerations are larger in the EW direction than in the NS direction.

Fig. 6.2 shows the acceleration response spectrum for this station compared to the design spectral acceleration. It is noticeable that the measured response spectrum from station GS.OK005 closely follows the design curve. At 1.0 sec, the measured spectral acceleration is $0.05g$ while the design value correspond to $0.097g$. Appendix B presents the calculations to determine the design response spectrum.
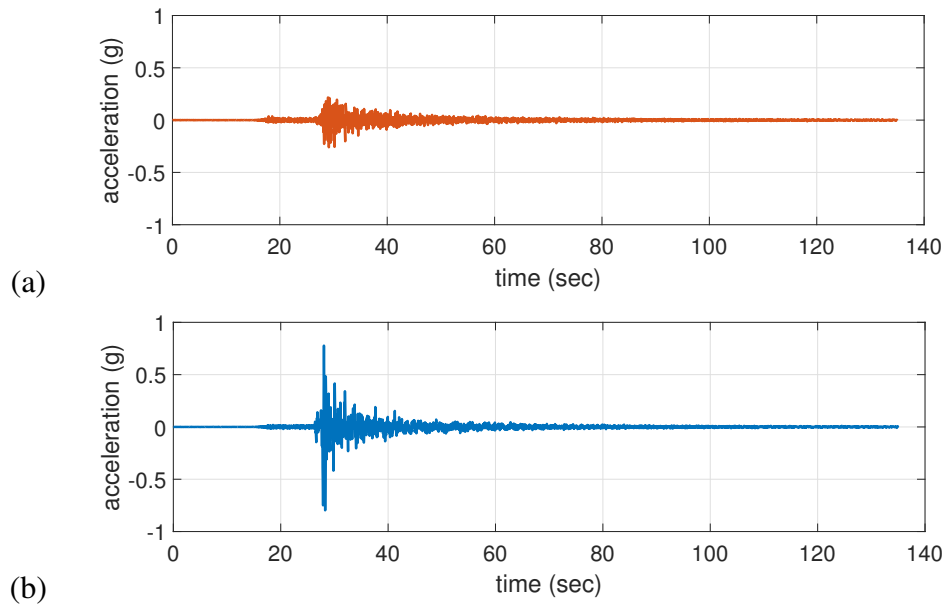
Figure 6.1: Measured ground-motion records from station GS.OK005 during the M 5.8 Pawnee event in the (a) NS and (b) EW directions.

Fig. 6.3 displays the 1.0-sec spectral acceleration (PSA) ShakeMap (USGS, 2016e) for the M 5.8 Pawnee earthquake. The ShakeMap shows that the contours of 1.0-sec PSA are not radial and this is because the spacial variation in site conditions. The largest 1.0-sec PSA close to the epicenter was determine to be $0.20g$ which was used to set up the scaling range for the scenarios.

In this chapter an incremental dynamic analysis is performed by scaling the GS.OK005 GM recordings. The recordings are scaled based on the 1.0-sec spectral acceleration (hereinafter denoted S_1) to be from $0.005g$ to $0.15g$ in increments of $0.005g$. The response of the typical bridge oriented both NS and EW were simulated under the 30 scaled bidirectional GMs, and the bearing and column responses were recorded. The maximum responses (bearing deflections and column curvatures) are presented in the following sections, along with representative force-deflection and moment-curvature responses.
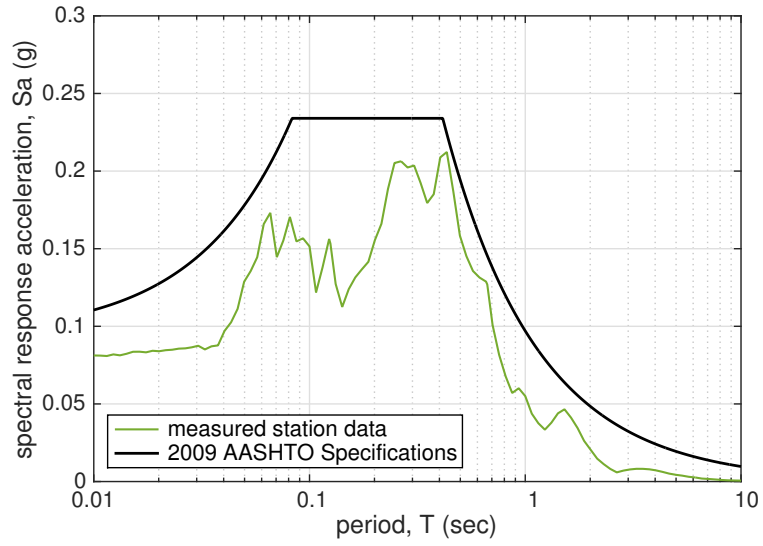
Figure 6.2: Spectral acceleration at station GS.OK005 during the M 5.8 Pawnee earthquake.
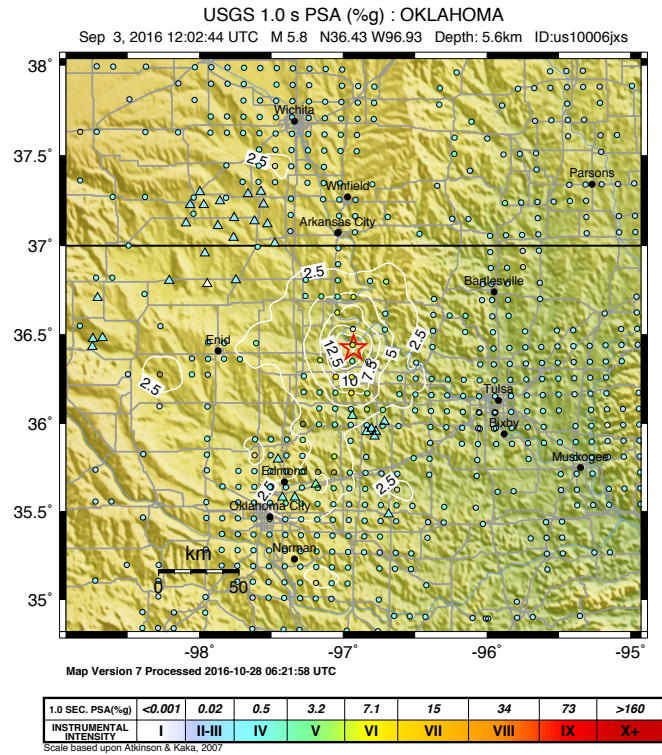
Figure 6.3: ShakeMap from M 5.8 Pawnee earthquake.

6.2   Seismic Evaluation of Bridge Bearings

Fig. 6.4 shows the peak bearing deflections for a bridge oriented NS and a bridge oriented EW versus the scaled spectral accelerations at 1.0 s. Different trends are observed for a bridge oriented NS and a bridge oriented EW.

For the NS-oriented bridge, the response remains predominantly linear up to $S_1 = 0.08g$, at which point the bearing deflections level off around 0.2 in. This nonlinearity corresponds to the bolts closing the 0.1875-in. gap in their holes and engaging the plates. Appreciably smaller bearing deflections are observed in some of the bearings for $S_1 < 0.13g$; the bearings that experienced smaller deflections were located in the abutments, which is more flexible transversely than the piers. Hence, the abutments accommodate additional transverse deflections instead of the bearings.

Similarly, for the EW-oriented bridge, the response remains predominantly linear up to $S_1 = 0.08g$, at which point the bearing deflections level off around 0.2 in. in the fixed-type bearings, whereas the expansion bearings permit additional deflection. The nonlinearity in the fixed-type bearings corresponds to the bolts closing the $\frac{3}{16}$-in. gap in their holes and engaging the plates.

At the design $S_1 = 0.10g$ (Appendix B), the bearing deflection responses on piers for a bridge oriented NS are slightly greater (0.1973 in.) than a bridge oriented EW. However, the bearing deflection response at the abutments for a bridge oriented EW are larger (0.1968 in.) than a bridge oriented NS. Considering the highest intensity case ($S_1 = 0.15g$), the bearing deflection responses at the abutments for a bridge oriented EW (0.32 in.) are 50% greater than a bridge oriented NS (0.21 in.).

6.2.1   Response Under Design Spectral Acceleration

The force-deflection response of two bearings — one located at pier one (expansion bearing) and another located at pier two (fixed bearing) — at $S_1 = 0.10g$ are represented
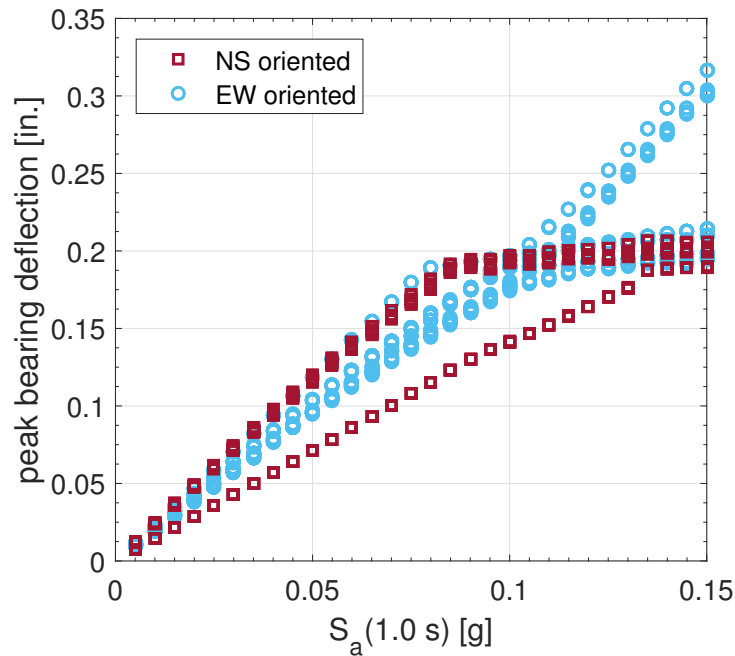
Figure 6.4: Peak bearing deflection for a bridge oriented NS and a bridge oriented EW.

individually for a bridge oriented NS and for a bridge oriented EW by Figs. 6.5 − 6.8.

For the NS-oriented bridge (Figs. 6.5 and 6.6), the maximum deflection for both types of elastomeric bearing is 0.19 in. in the transverse (EW) direction. The engagement of the anchor bolt can be seen in the force-deflection curve (Figs. 6.5(b) and 6.6(b)) by a large spike in the force. The expansion and fixed bearings behave similarly because transversely they have the same clearance gap, as can be seen in Figs. 6.5 and 6.6.

For the EW-oriented bridge (Figs. 6.7 and 6.8), the maximum deflection in the expansion and fixed elastormeric bearings are 0.18 and 0.17 in., respectively, with both occurring in the longitudinal (EW) direction. Furthermore, both the expansion and fixed bearings behave similarly as can be seen in Fig. 6.7 and 6.8.

Although the difference in peak bearing deflection for both bridge orientations is small, for the NS-oriented bridge, the gap (³⁄₁₆-in.) is closed and the anchor bolt is engaged. This occurs because the gap is small transversely. The maximum deflection is 0.19 in. and the bearing force reaches nearly 19 kips. In the EW-oriented bridge (Figs.

Figure 6.5: Force-deflection response of an expansion-type elastomeric bearing for a bridge oriented NS at $S_1 = 0.10g$: (a) d_E vs. d_N (b) d_E vs. F_E (c) F_N vs. d_N and (d) F_N vs. F_E.

Figure 6.6: Force-deflection response of a fixed-type elastomeric bearing for a bridge oriented NS at $S_1 = 0.10g$: (a) d_E vs. d_N (b) d_E vs. F_E (c) F_N vs. d_N and (d) F_N vs. F_E.

Figure 6.7: Force-deflection response of an expansion-type elastomeric bearing for a bridge oriented EW at $S_1 = 0.10g$: (a) d_E vs. d_N (b) d_E vs. F_E (c) F_N vs. d_N and (d) F_N vs. F_E.

Figure 6.8: Force-deflection response of a fixed-type elastomeric bearing for a bridge oriented EW at $S_1 = 0.10g$: (a) d_E vs. d_N (b) d_E vs. F_E (c) F_N vs. d_N and (d) F_N vs. F_E.

6.7 and 6.8), the responses are smaller than the transverse gap ($\frac{3}{16}$-in.) so the responses remains linear.

6.2.2 Response Under $1.5\times$ Design Spectral Acceleration

Next, the response of the bridge is presented for a case of shaking 50% greater than the design level. The force-deflection response of two bearings — one located at pier one (expansion bearing) and another located at pier two (fixed bearing) — at $S_1 = 0.15g$ are shown individually for a bridge oriented NS and for a bridge oriented EW by Figs. 6.9 – 6.12. Note that this level of shaking is smaller than the largest S_1 predicted by ShakeMap ($0.20g$).

For the NS-oriented bridge (Figs. 6.9 and 6.10), the maximum deflection for both types of elastomeric bearing is 0.20 in. in the transverse (EW) direction. The engagement of the anchor bolt can be seen in the force-deflection curve (Figs. 6.9(b) and 6.10(b)) by a large spike in the force. The expansion and fixed bearings behave similarly as shown in Figs. 6.9 and 6.10.

For the EW-oriented bridge (Figs. 6.11 and 6.12), the maximum deflection in the expansion and fixed elastormeric bearings are 0.30 and 0.19 in., respectively, with both occurring in the longitudinal (EW) direction. However, the expansion and fixed bearings behave differently. Fig. 6.11(b) exhibits sliding (friction) of the expansion-type bearings. Moreover, Fig. 6.12(b) shows a large spike in the force, which is the result of the anchor bolts being engaged.

Although the difference in peak bearing deflection for both bridge orientations when considering higher accelerations is still similar to the peak bearing deflection at $0.10g$, the gap ($\frac{3}{16}$-in.) is still closed and the anchor bolts are engaged. But, for an expansion-type bearing in a bridge oriented EW (Fig. 6.11), sliding effects are substantial when the bearing forces saturate around 10.65 kips.
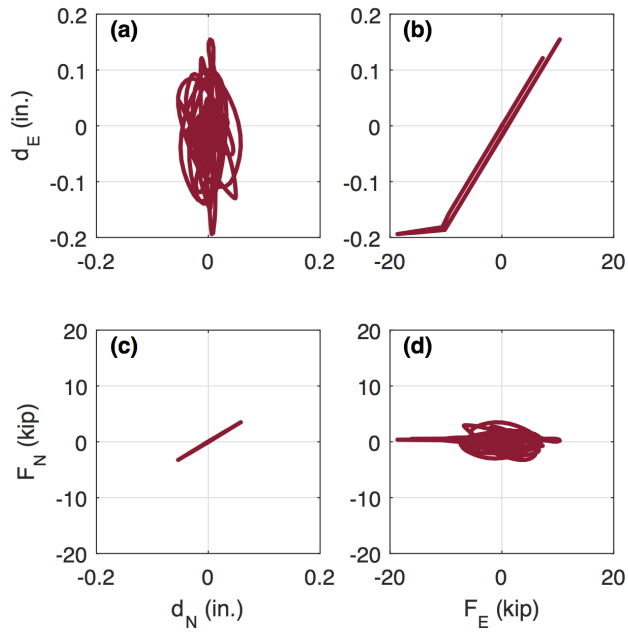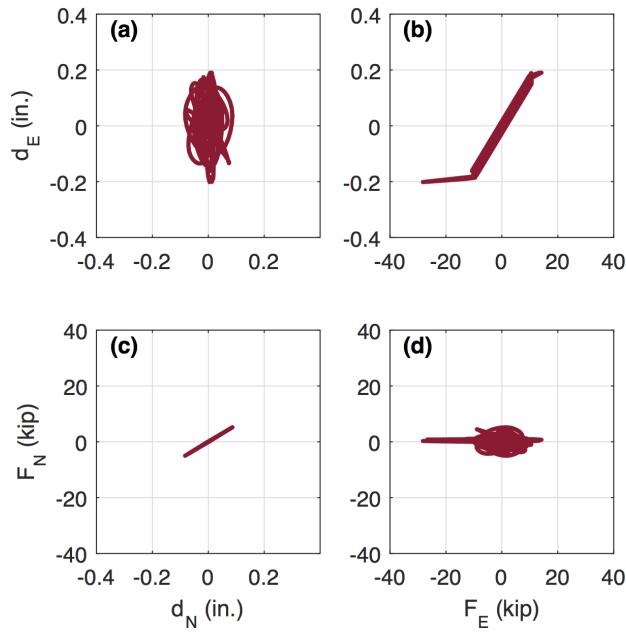
Figure 6.9: Force-deflection response of an expansion-type elastomeric bearing for a bridge oriented NS at $S_1 = 0.15g$: (a) d_E vs. d_N (b) d_E vs. F_E (c) F_N vs. d_N and (d) F_N vs. F_E.
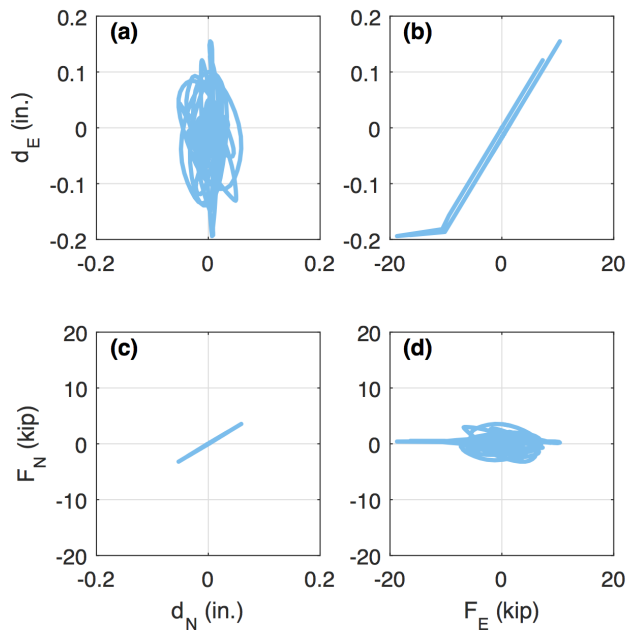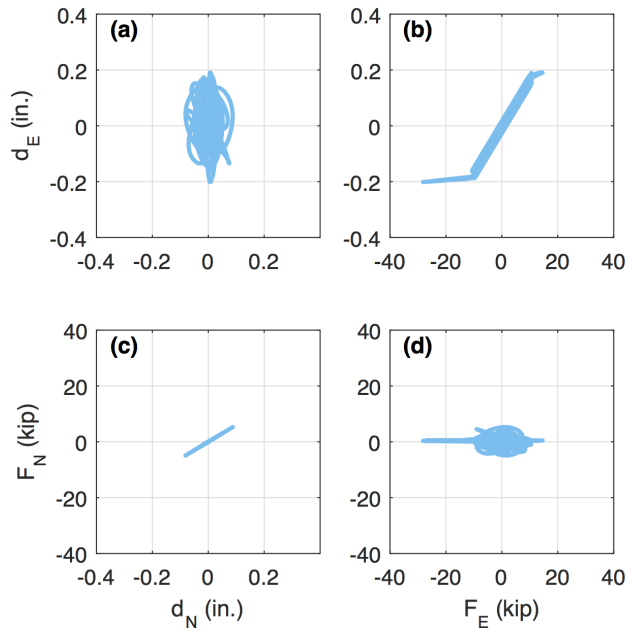

Figure 6.10: Force-deflection response of a fixed-type elastomeric bearing for a bridge oriented NS at $S_1 = 0.15g$: (a) d_E vs. d_N (b) d_E vs. F_E (c) F_N vs. d_N and (d) F_N vs. F_E.
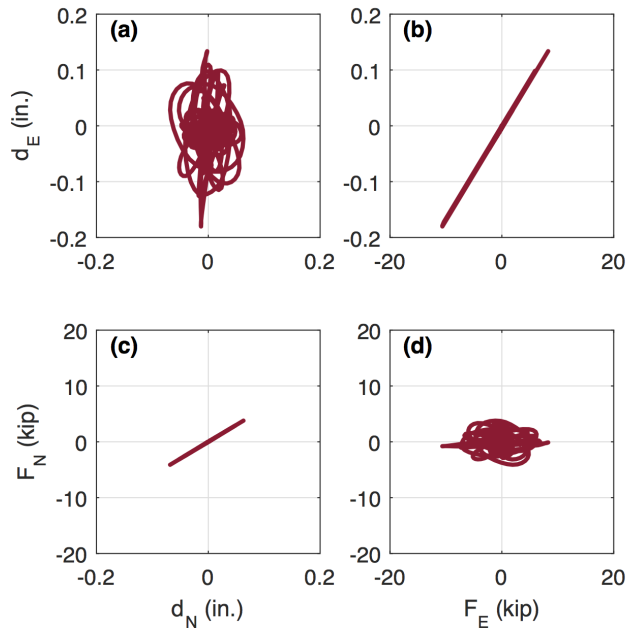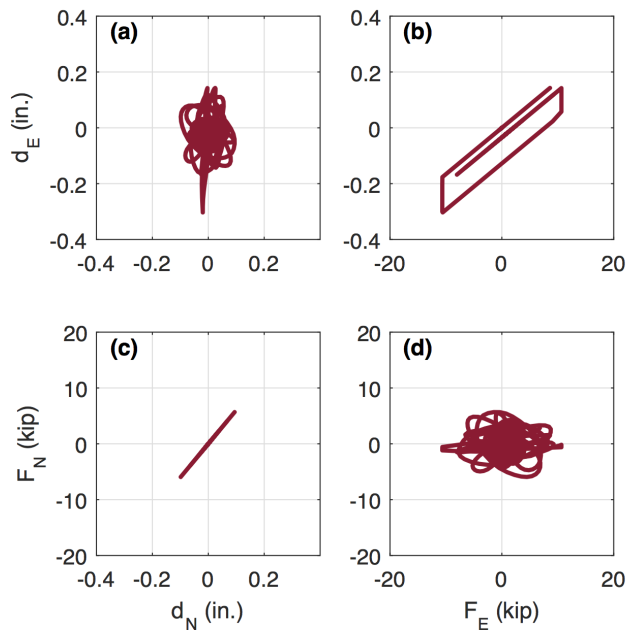
Figure 6.11: Force-deflection response of an expansion-type elastomeric bearing for a bridge oriented EW at $S_1 = 0.15g$: (a) d_E vs. d_N (b) d_E vs. F_E (c) F_N vs. d_N and (d) F_N vs. F_E.
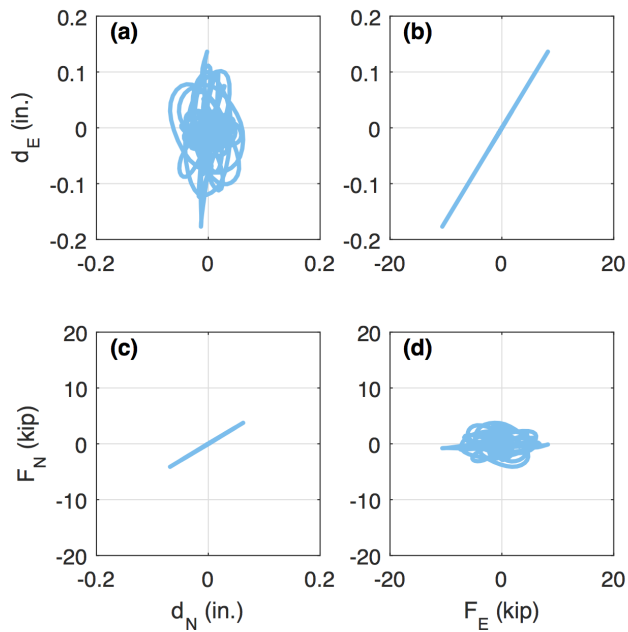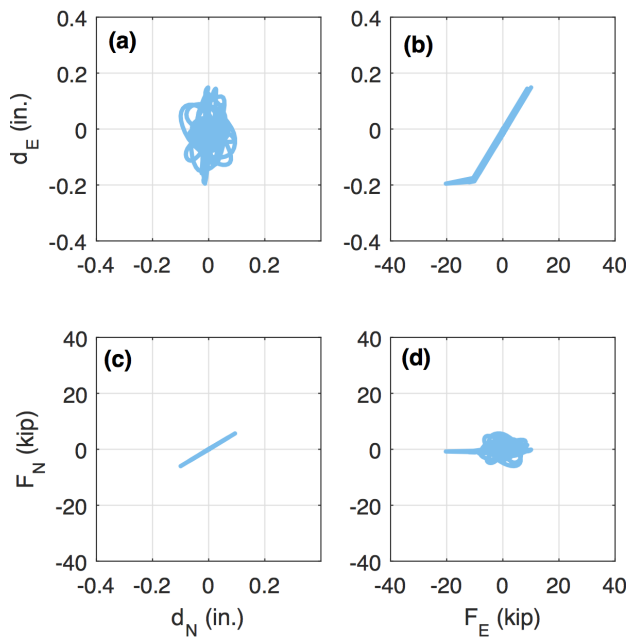

Figure 6.12: Force-deflection response of a fixed-type elastomeric bearing for a bridge oriented EW at $S_1 = 0.15g$: (a) d_E vs. d_N (b) d_E vs. F_E (c) F_N vs. d_N and (d) F_N vs. F_E.

6.3   Seismic Evaluation of Concrete Columns

Fig. 6.13 shows the peak column curvatures for bridges oriented NS and EW versus the scaled spectral accelerations at 1.0 sec (S_1). Up to $S_1 = 0.085g$, the peak column curvatures for the NS- and EW-oriented bridges are nearly identical, but then diverge at higher intensities. Beyond $S_1 = 0.085g$, larger curvatures are observed in the NS-oriented bridge, which is attributed to the gaps closing in the elastomeric bearings (Fig. 6.4) and transferring the inertial load of the deck to the piers. Similarly, for the EW-oriented bridge, larger column curvatures are observed in the piers with fixed-type bearings that provide a load path to the pier. Smaller curvatures are observed in the piers with expansion bearings because the inertial loads are not transmitted to the piers. The divergence of the responses in the two piers can be seen in Fig. 6.13.

6.3.1   Response Under Design Spectral Acceleration

The moment-curvature responses for two columns — one located at pier 1 (expansion-expansion) and another located at pier 2 (fixed-expansion) — at $S_1 = 0.10g$ are dis-
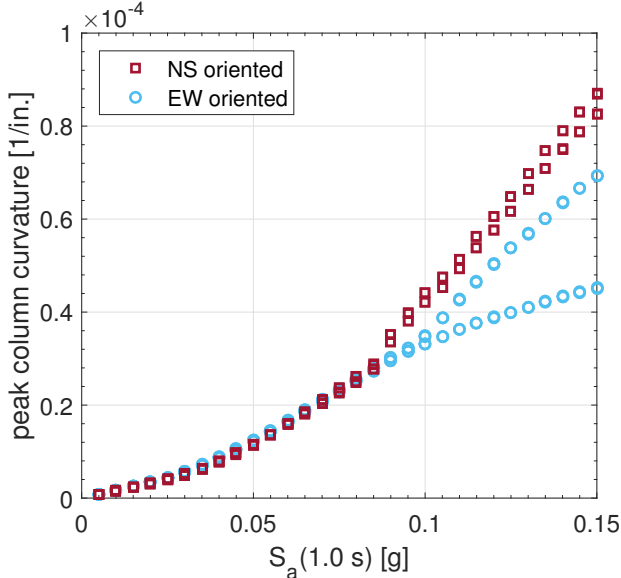
Figure 6.13: Peak column curvature for a bridge oriented NS and a bridge oriented EW.

played individually for a bridge oriented NS and a bridge oriented EW by Figs. 6.14 – 6.17.

Considering both columns, the one located at pier 2 displayed the largest column curvature. This is because the anchor bolts are engaged, creating a path for the inertial load of the superstructure to be transmitted to the bent. Figs. 6.14 and 6.15 show that the maximum column curvature are 42.05×10^{-6} and 44.05×10^{-6} 1/in., while Figs. 6.16 and 6.17 display maximum column curvatures of 33.18×10^{-6} and 34.69×10^{-6} 1/in. The curvatures observed when the bridge is oriented EW are smaller because the inertial loads transmitted to the pier are lower. The bearings are less stiff while oriented EW than they are while oriented NS, transmitting less inertial load.

Recalling that the the yield curvature of the columns is 106.0×10^{-6} 1/in., for this scenario it can be seen that the column curvature is moderately below its yield curvature — a curvature ductility of about 40% for a expansion type bearing and 42% a fixed type bearing when a bridge is oriented NS and 31% for a expansion type bearing and 32% a fixed type bearing when a bridge is oriented EW.

6.3.2 Response Under $1.5\times$ Design Spectral Acceleration

The moment-curvature responses for two columns — one located at pier 1 and another located at pier 2 — at $S_1 = 0.15g$ are displayed individually for a bridge oriented NS and a bridge oriented EW by Figs. 6.18 – 6.21. Note that this level of shaking is smaller than the largest predicted by ShakeMap ($0.20g$).

For this scenario, the column located at pier 2 still displayed the largest column curvature, as seen at the design $S_1 = 0.10g$. Figs. 6.18 and 6.19 show that the maximum column curvature are 82.09×10^{-6} and 86.87×10^{-6} 1/in., which is two times larger than the curvatures at $0.10g$ (Figs. 6.14 and 6.15). Figs. 6.20 and 6.21 display maximum column curvature of 44.98×10^{-6} and 69.19×10^{-6} 1/in. which are 25% and 50% larger than the responses at $0.10g$ (Figs. 6.16 and 6.17).

Figure 6.14: Moment-curvature response of a column located at pier 1 for a bridge oriented NS at $S_1 = 0.10g$: (a) ϕ_E vs. ϕ_N (b) ϕ_E vs. M_E (c) M_N vs. ϕ_N and (d) M_N vs. M_E.

Figure 6.15: Moment-curvature response of a column located at pier 2 for a bridge oriented NS at $S_1 = 0.10g$: (a) ϕ_E vs. ϕ_N (b) ϕ_E vs. M_E (c) M_N vs. ϕ_N and (d) M_N vs. M_E.

Recalling that the yield curvature of the columns is 106.0×10^{-6} 1/in., the column curvatures at $0.15g$ are still below the yield curvature — a curvature ductility of about 77% for an expansion-type bearing and 81% for a fixed-type bearing when a bridge is oriented NS and 42% for an expansion-type bearing and 66% for a fixed-type bearing when a bridge is oriented EW.

6.4 Summary

The detailed finite element model of the SH-99 bridge over Tiger Creek was used to conduct an incremental dynamic analysis at design-level and at larger motions to assess the bridge response. The GM from station GS.OK005 was scaled based on the 1.0-sec spectral acceleration S_1 to be from $0.005g$ to $0.15g$ (1.5 times higher than the design S_1). The analysis indicated that at design S_1 ($0.10g$) (a) the maximum bearing deflection is seen for the NS-oriented bridge, corresponding to predominantly transverse (EW) motion and is 0.19 in. for the expansion- and fixed-type elastomeric bearings; and (b) the maximum column curvature is displayed for the NS-oriented bridge and is about 42% of the yield curvature. Up to $S_1 = 0.085g$, the response remained linear, but then diverged for larger S_1 due to engagement of the anchor bolts in the elastomeric bearings. Then for $S_1 = 0.15g$, the analysis indicated that (c) the maximum deformation at the bearings is observed for the EW-oriented bridge. The expansion-type bearings experienced up to 0.30 in. in the longitudinal direction, while the fixed-type elastomeric bearings were constrained by the anchor bolt to deflect only 0.19 in.; the expansion-type bearing demonstrated sliding of the elastomeric pad; and (d) the maximum column curvature is shown for the NS-oriented bridge and reached about 82% of the yield curvature due to transmission of the superstructure's inertial load into the piers upon engagement of the anchor bolts in their holes.
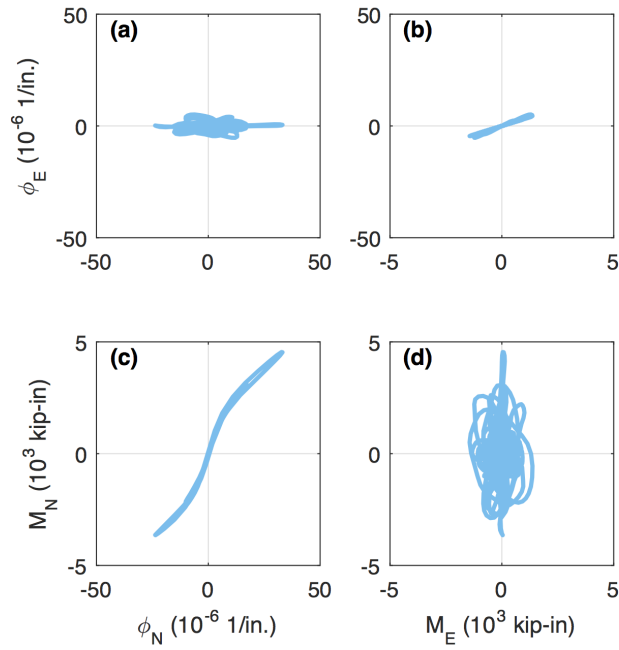
Figure 6.16: Moment-curvature response of a column located at pier 1 for a bridge oriented EW at $S_1 = 0.10g$: (a) ϕ_E vs. ϕ_N (b) ϕ_E vs. M_E (c) M_N vs. ϕ_N and (d) M_N vs. M_E.
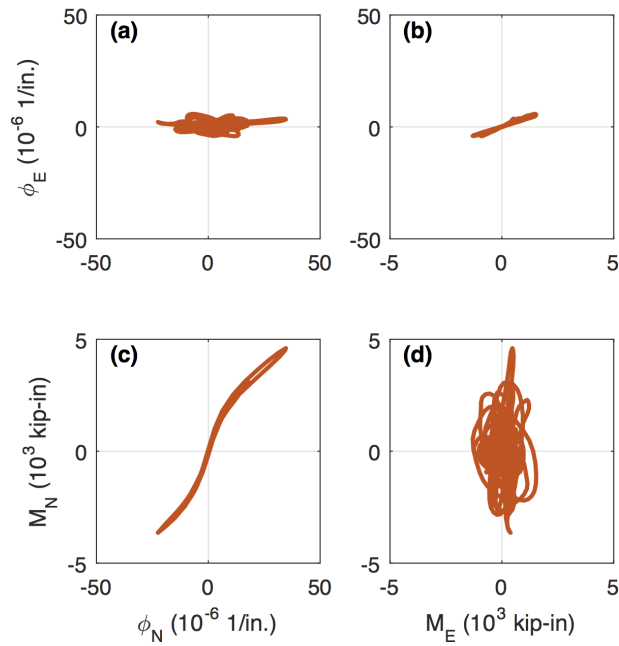
Figure 6.17: Moment-curvature response of a column located at pier 2 for a bridge oriented EW at $S_1 = 0.10g$: (a) ϕ_E vs. ϕ_N (b) ϕ_E vs. M_E (c) M_N vs. ϕ_N and (d) M_N vs. M_E.
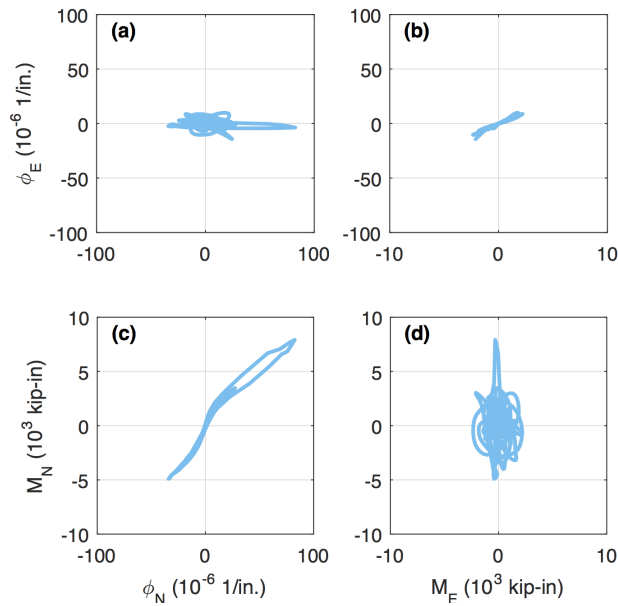
Figure 6.18: Moment-curvature response of a column located at pier 1 for a bridge oriented NS at $S_1 = 0.15g$: (a) ϕ_E vs. ϕ_N (b) ϕ_E vs. M_E (c) M_N vs. ϕ_N and (d) M_N vs. M_E.
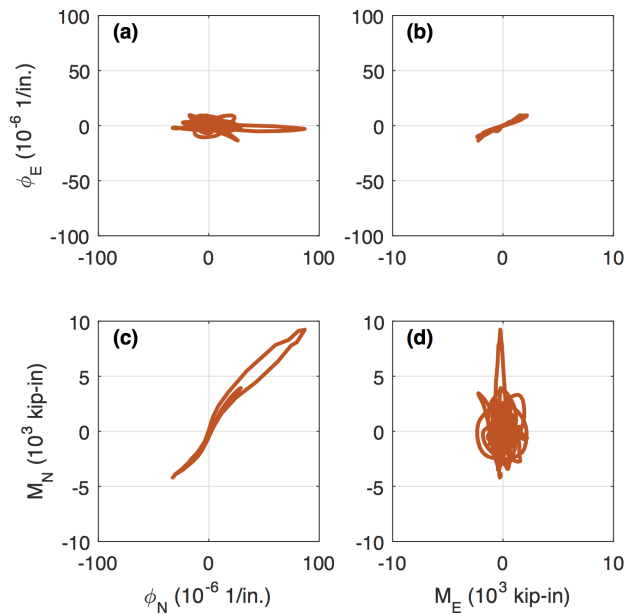
Figure 6.19: Moment-curvature response of a column located at pier 2 for a bridge oriented NS at $S_1 = 0.15g$: (a) ϕ_E vs. ϕ_N (b) ϕ_E vs. M_E (c) M_N vs. ϕ_N and (d) M_N vs. M_E.
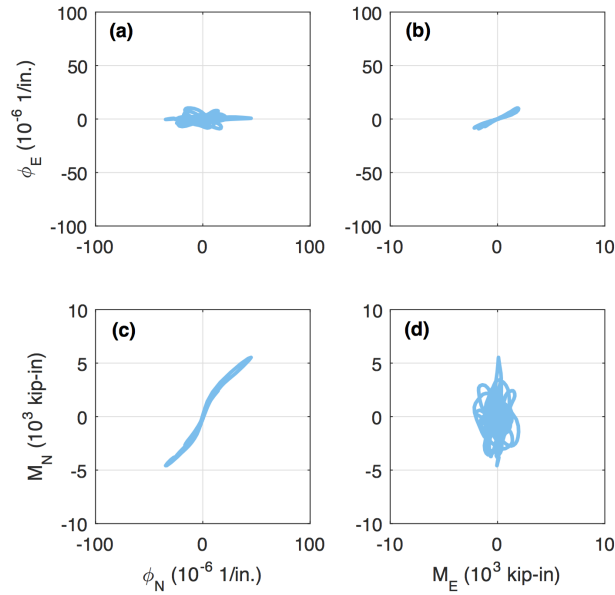
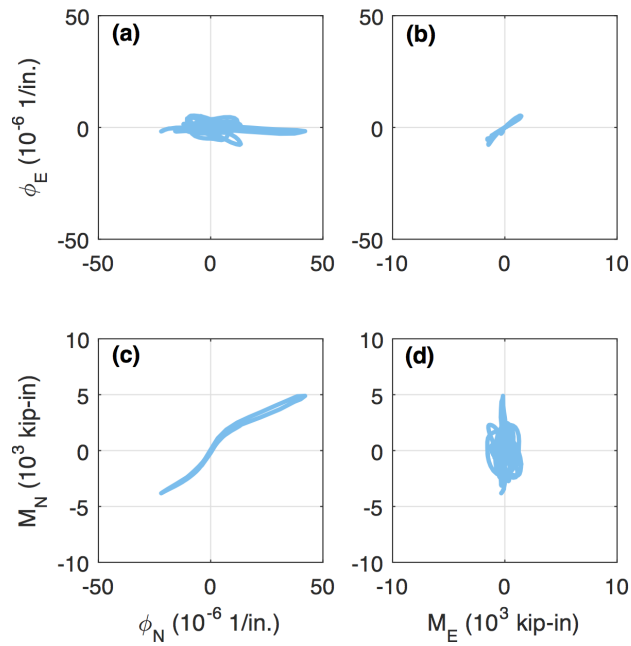**Figure 6.20:** Moment-curvature response of a column located at pier 1 for a bridge oriented EW at $S_1 = 0.15g$: (a) ϕ_E vs. ϕ_N (b) ϕ_E vs. M_E (c) M_N vs. ϕ_N and (d) M_N vs. M_E.
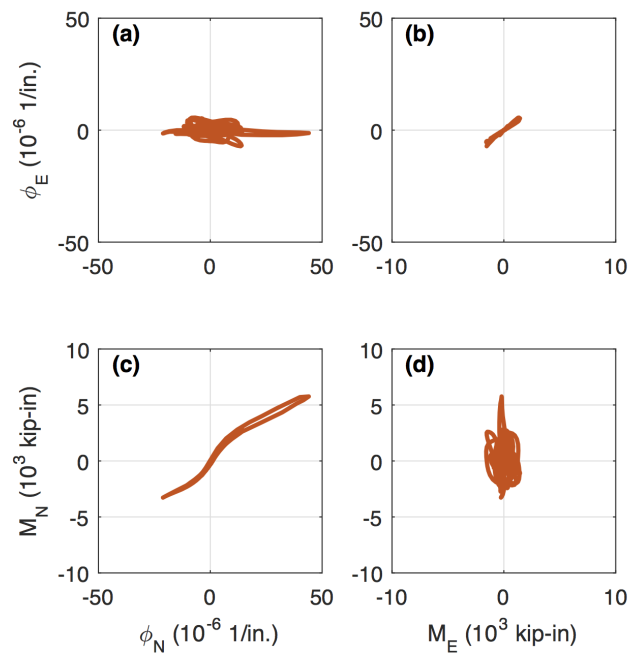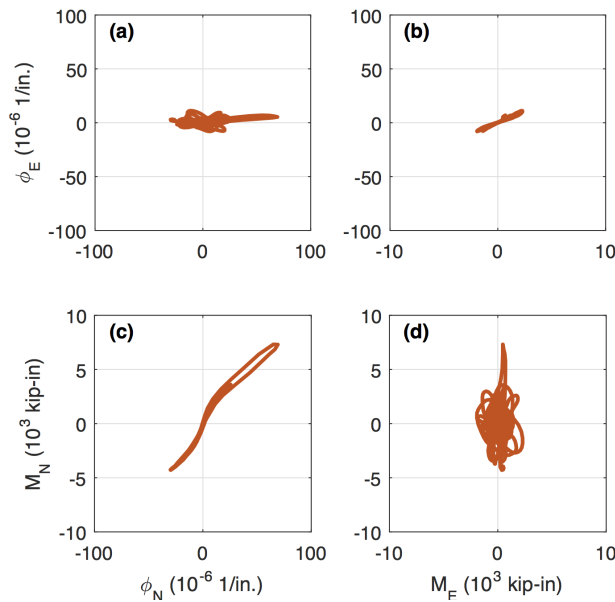

Figure 6.21: Moment-curvature response of a column located at pier 2 for a bridge oriented EW at $S_1 = 0.15g$: (a) ϕ_E vs. ϕ_N (b) ϕ_E vs. M_E (c) M_N vs. ϕ_N and (d) M_N vs. M_E.

Chapter 7

Summary, Conclusions, and Future Work

7.1   Summary and Conclusions

Prior to 2011, little attention was given to the seismic hazard to infrastructure in Oklahoma as earthquake activity was quite low. Since then there has been a rapid increase in the number and magnitude of earthquakes occurring in and around Oklahoma. The research presented in this thesis has explored the vulnerability of Oklahoma's highway bridges to these earthquakes. The objectives of this work were primarily three-fold: (i) identify and analytically model the most typical bridge class represented in Oklahoma; (ii) characterize the seismic demand on Oklahoma bridges, comparing mapped design levels to actual measurements; and (iii) rigorously evaluate the performance of the typical Oklahoma bridge under measured and scaled bidirectional ground motions.

In the first part of this thesis, Oklahoma highway bridge inventory data was analyzed to classify the most typical bridge class, which was then modeled using finite elements. In Chapter 2, a detailed analysis of the Oklahoma Department of Transportation's on-system bridge inventory was performed. Prestressed concrete (PC) girder bridges were the dominant group, constituting 47% of the total bridge inventory (excluding culvert bridges). Among PC girder bridges, the largest bridge category was found to be the multi-span simply-supported bridges, which account for approximately 85.2% percent of PC girder bridges. Moreover, it was observed that 48% of the bridges were repre-

sented by three spans, so this study focuses on three-span PC (3SPC) girder bridges.

In Chapter 3, a three-dimensional finite element model of a typical 3SPC girder bridge was developed using the analysis software *OpenSees*. The bridge components consist of prestressed concrete girders, deck slab, abutments, bents (beams and columns), foundations (drilled shafts), and fixed- and expansion- type elastomeric bearings. The model was developed to integrate a high degree of fidelity in the major bridge components (e.g., bearings and columns) that were to be used as damage indicators. For the elastomeric bearings, deflections limits in terms of engagement and failure of the anchor bolts were established; for the reinforced concrete columns, first-yield and ultimate capacities were determined. Finally, an eigenvalue analysis indicated that the fundamental modes were dominated by longitudinal and transverse rigid-body motion.

Following the development of the finite element model, the seismic demand on Oklahoma bridges was characterized in Chapter 4. To represent the actual seismic hazard in Oklahoma, this study focused on recent earthquakes in the region. Seismic station data measured during the largest earthquake to date (the M 5.8 Pawnee earthquake) was used to generate a suite of 27 bidirectional ground motions (GMs) that were subsequently applied in time-history analyses of the typical Oklahoma bridge. The suite of GMs contained variability in epicentral distance, soil type and spectral characteristics. Spectral response accelerations determined from the measured GMs were compared to design spectra; in some cases the measured spectral responses exceeded the design values, especially at short periods (0.1 – 0.3 sec).

Finally, transient analyses were conducted using the finite element model to evaluate the response of the bridge and assess the potential for damage. In Chapter 5, transient time-history bridge responses were calculated for the suite of 27 measured GMs. The analytical model of the 3SPC girder bridge was subjected to these bidirectional ground

motion records. Two bridge orientations were considered for each GM: North-South (NS) and East-West (EW). Capacity limit states for as-built components from Nielson (2005) were used when appropriate and modified otherwise for this bridge case. From the peak bearing deflection responses, larger bearing deflections were observed for the NS-oriented bridge, and the GMs recorded at station GS.OK005 produce the largest bearing deflection of approximately 0.13 in., which is less than the anchor bolt clearance in its slot/hole. From the peak column curvature responses, the bridge oriented EW exhibited larger column curvatures — up to 13.45% of the yield curvature. For the GS.OK005 record, the predominant motion was in the East direction (corresponding to larger curvatures about the North-axis, ϕ_N), indicating a stronger GM component in the EW direction than in the NS direction. Overall, small bearing deflections and column curvatures were observed, and the responses remained nearly linear.

In Chapter 6, an incremental dynamic analysis was conducted to assess the response of the typical highway bridge to design-level and larger motions. The GM from station GS.OK005 was scaled based on the 1.0-sec spectral acceleration S_1 to be from $0.005g$ to $0.15g$ (1.5 times higher than the design S_1). Up to $S_1 = 0.085g$, the response remained linear, but then diverged for larger S_1 due to engagement of the anchor bolts in the elastomeric bearings.

At the design S_1 ($0.10g$), the largest bearing deflections and column curvatures were both observed for the NS-oriented bridge, corresponding to predominantly transverse (EW) motion. Both the expansion- and fixed-type elastomeric bearings experienced deflections up to 0.19 in.; the columns sustained curvatures up to 42% of the yield curvature. At $S_1 = 0.15g$, the largest bearing deflections were observed for the EW-oriented bridge, whereas the largest column curvatures were observed for the NS-oriented bridge. The expansion-type bearings experienced deflections up to 0.30 in. in the longitudinal direction, while the fixed-type elastomeric bearings were constrained

by the anchor bolt to deflect only 0.19 in.; the expansion-type bearing demonstrated sliding of the elastomeric pad. Column curvatures on the NS-oriented bridge reached 82% of the yield curvature due to transmission of the superstructure's inertial load into the piers upon engagement of the anchor bolts in their holes.

Damage of the considered 3SPC girder bridge was not observed during the application of the largest GM event in Oklahoma to date. However, considering higher accelerations showed that effects such as sliding of the bearings and yielding of the steel in columns may be possible and may produce some impact in the future of Oklahoma highway bridges.

7.2 Future Work

This research is a first step toward assessing the vulnerability of Oklahoma bridges to the emerging seismic threat. As a continuation of this research, the following are several areas which have the potential for further investigation:

- This research examined a single earthquake event in determining the seismic response of the most typical Oklahoma bridge. Due to the increasing number and magnitude of earthquakes in the region, the effects of repeated small-to-moderate seismic loading should be explored.

- The work performed in this study considered as-built conditions in the modeling of the SH-99 bridge over Tiger Creek. The inclusion of factors that trigger deterioration processes such as corrosion and scour in combination with seismic loading should be investigated to truly represent an aging highway bridge structure.

- The current study considered the modeling of the soil-structure interaction of the abutment by using linear elements. To expand the interaction and represent a

more realistic soil behavior, the inclusion and modeling of non-linear elements should be considered as well as performing soil-structure interaction analyses for the abutments and drilled shafts.

- The work realized in this study contemplated the damage characterization of the most typical Oklahoma bridge by close examination of bearings deflection and column curvature data. The development of fragility curves as seismic risk assessment tool for the most typical Oklahoma bridge is a straightforward extension of this work and should be topic of further research.

Appendix A

Nielson (2005) Limit States

Tables A.1 and A.2 respectively present the prescriptive and Bayesian updated limit states for bridge components.

Table A.1: x

Prescriptive limit states for bridge components taken from Nielson (2005).

Component	Slight	Moderate	Extensive	Complete
REINFORCED CONCRETE COLUMN				
curvature ductility μ_ϕ	1.0	1.58	3.22	6.84
FIXED-TYPE ELASTOMERIC BEARING				
longitudinal deflection (in.)	1.18	3.94	5.91	10.0
transverse deflection (in.)	1.18	3.94	5.91	10.0
EXPANSION-TYPE ELASTOMERIC BEARING				
longitudinal deflection (in.)	1.18	3.94	5.91	10.0
transverse deflection (in.)	1.18	3.94	5.91	10.0

Table A.2: Bayesian updated limit states for bridge components.

Component	Slight	Moderate	Extensive	Complete
REINFORCED CONCRETE COLUMN				
curvature ductility μ_ϕ	1.29	2.10	3.52	5.24
FIXED-TYPE ELASTOMERIC BEARING				
longitudinal deflection (in.)	1.14	4.10	5.36	7.35
transverse deflection (in.)	1.14	3.58	5.60	7.68
EXPANSION-TYPE ELASTOMERIC BEARING				
longitudinal deflection (in.)	1.14	4.10	5.36	7.35
transverse deflection (in.)	1.14	3.58	5.60	7.68

Appendix B

Design Calculations for GS.OK005

The following pages present the design calculations for a bridge per the 2009 AASHTO Guide Specifications for LRFD Seismic Bridge Design (AASHTO, 2009) at the site of seismic station GS.OK005.

≋USGS Design Maps Detailed Report

2009 AASHTO Guide Specifications for LRFD Seismic Bridge Design (35.65486°N, 97.1911°W)

Site Class D – "Stiff Soil"

Article 3.4.1 — Design Spectra Based on General Procedure

Note: Maps in the 2009 AASHTO Specifications are provided by AASHTO for Site Class B.
Adjustments for other Site Classes are made, as needed, in Article 3.4.2.3.

From Figure 3.4.1-2 [1]	PGA = 0.073 g
From Figure 3.4.1-3 [2]	S_s = 0.146 g
From Figure 3.4.1-4 [3]	S_1 = 0.040 g

Article 3.4.2.1 — Site Class Definitions

The authority having jurisdiction (not the USGS), site-specific geotechnical data, and/or the default has classified the site as Site Class D, based on the site soil properties in accordance with Article 3.4.2.

Table 3.4.2.1–1 Site Class Definitions

SITE CLASS	SOIL PROFILE NAME	Soil shear wave velocity, $\overline{v}_s$, (ft/s)	Standard penetration resistance, $\overline{N}$	Soil undrained shear strength, $\overline{s}_u$, (psf)
A	Hard rock	$\overline{v}_s > 5,000$	N/A	N/A
B	Rock	$2,500 < \overline{v}_s \leq 5,000$	N/A	N/A
C	Very dense soil and soft rock	$1,200 < \overline{v}_s \leq 2,500$	$\overline{N} > 50$	>2,000 psf
D	Stiff soil profile	$600 \leq \overline{v}_s < 1,200$	$15 \leq \overline{N} \leq 50$	1,000 to 2,000 psf
E	Stiff soil profile	$\overline{v}_s < 600$	$\overline{N} < 15$	<1,000 psf
E	—	Any profile with more than 10 ft of soil having the characteristics: 1. Plasticity index $PI > 20$, 2. Moisture content $w \geq 40\%$, and 3. Undrained shear strength $\overline{s}_u < 500$ psf		
F	—	Any profile containing soils having one or more of the following characteristics: 1. Soils vulnerable to potential failure or collapse under seismic loading such as liquefiable soils, quick and highly sensitive clays, collapsible weakly cemented soils. 2. Peats and/or highly organic clays ($H > 10$ feet of peat and/or highly organic clay where H = thickness of soil) 3. Very high plasticity clays ($H > 25$ feet with plasticity index $PI > 75$) 4. Very thick soft/medium stiff clays ($H > 120$ feet)		

For SI: 1ft/s = 0.3048 m/s 1lb/ft² = 0.0479 kN/m²

Article 3.4.2.3 — Site Coefficients

Table 3.4.2.3-1 (for F_{pga})—Values of F_{pga} as a Function of Site Class and Mapped Peak Ground Acceleration Coefficient

Site Class	Mapped Peak Ground Acceleration				
	PGA ≤ 0.10	PGA = 0.20	PGA = 0.30	PGA = 0.40	PGA ≥ 0.50
A	0.8	0.8	0.8	0.8	0.8
B	1.0	1.0	1.0	1.0	1.0
C	1.2	1.2	1.1	1.0	1.0
D	1.6	1.4	1.2	1.1	1.0
E	2.5	1.7	1.2	0.9	0.9
F	See AASHTO Article 3.4.3				

Note: Use straight–line interpolation for intermediate values of PGA

For Site Class = D and PGA = 0.073 g, F_{PGA} = 1.600

Table 3.4.2.3-1 (for F_a)—Values of F_a as a Function of Site Class and Mapped Short-Period Spectral Acceleration Coefficient

Site Class	Spectral Response Acceleration Parameter at Short Periods				
	S_S ≤ 0.25	S_S = 0.50	S_S = 0.75	S_S = 1.00	S_S ≥ 1.25
A	0.8	0.8	0.8	0.8	0.8
B	1.0	1.0	1.0	1.0	1.0
C	1.2	1.2	1.1	1.0	1.0
D	1.6	1.4	1.2	1.1	1.0
E	2.5	1.7	1.2	0.9	0.9
F	See AASHTO Article 3.4.3				

Note: Use straight–line interpolation for intermediate values of S_S

For Site Class = D and S_S = 0.146 g, F_a = 1.600

Table 3.4.2.3-2—Values of F_v as a Function of Site Class and Mapped 1-sec Period Spectral Acceleration Coefficient

Site Class	Mapped Spectral Response Acceleration Coefficient at 1-sec Periods				
	$S_1 \leq 0.10$	$S_1 = 0.20$	$S_1 = 0.30$	$S_1 = 0.40$	$S_1 \geq 0.50$
A	0.8	0.8	0.8	0.8	0.8
B	1.0	1.0	1.0	1.0	1.0
C	1.7	1.6	1.5	1.4	1.3
D	2.4	2.0	1.8	1.6	1.5
E	3.5	3.2	2.8	2.4	2.4
F	See AASHTO Article 3.4.3				

Note: Use straight–line interpolation for intermediate values of S_1

For Site Class = D and S_1 = 0.040 g, F_v = 2.400

Equation (3.4.1-1): $A_S = F_{PGA}\ PGA = 1.600 \times 0.073 = 0.117\ g$

Equation (3.4.1-2): $S_{DS} = F_a\ S_S = 1.600 \times 0.146 = 0.234\ g$

Equation (3.4.1-3): $S_{D1} = F_v\ S_1 = 2.400 \times 0.040 = 0.097\ g$

Figure 3.4.1-1: Design Response Spectrum

$$\begin{cases} T < T_0 : S_a = S_{DS}\,(\,0.4 + 0.6\,T/T_0\,) \\ T_0 \leq T \leq T_S : S_a = S_{DS} \\ T_S < T \leq T_L : S_a = S_{D1}/T \\ T > T_L : S_a = S_{D1}T_L/T^2 \end{cases}$$

$S_{DS} = 0.234$

$A_S = 0.117$

$S_{D1} = 0.097$

Spectral Response Acceleration, Sa (g)

$T_0 = 0.083$ $T_S = 0.415$ 1.000

Period, T (sec)

96
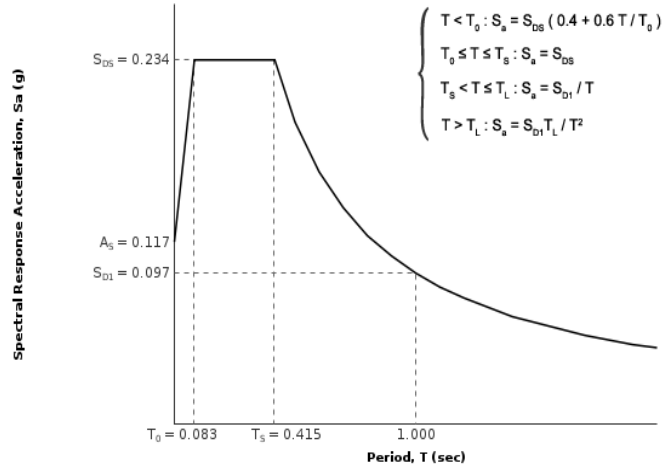
Article 3.5 - Selection of Seismic Design Category (SDC)

Table 3.5-1—Partitions for Seismic Design Categories A, B, C, and D

VALUE OF S_{D1}	SDC
$S_{D1} < 0.15g$	A
$0.15g \leq S_{D1} < 0.30g$	B
$0.30g \leq S_{D1} < 0.50g$	C
$0.50g \leq S_{D1}$	D

For S_{D1} = 0.097 g, Seismic Design Category = A

Seismic Design Category ≡ "the design category in accordance with Table 3.5-1" = A

References

1. *Figure 3.4.1-2*: http://earthquake.usgs.gov/hazards/designmaps/downloads/pdfs/AASHTO-2009-Figure-3.4.1-2.pdf
2. *Figure 3.4.1-3*: http://earthquake.usgs.gov/hazards/designmaps/downloads/pdfs/AASHTO-2009-Figure-3.4.1-3.pdf
3. *Figure 3.4.1-4*: http://earthquake.usgs.gov/hazards/designmaps/downloads/pdfs/AASHTO-2009-Figure-3.4.1-4.pdf

Bibliography

AASHTO (2009). *Guide Specifications for LRFD Seismic Bridge Design*. Association of State Highway and Transportation Officials, Washington D.C.

Akiyama, M., Frangopol, D., and H., M. (2011). "Life-cycle reliability of RC bridge piers under seismic and airborne chloride hazards." *Earthquake Engineering and Structural Dynamics*, 40, 1671–1687.

Alam, M. S., Bhuiyan, A. R., , and Billah, A. H. M. (2012). "Seismic fragility assessment of SMA-bar restrained multi-span continuous highway bridge isolated by different laminated rubber bearings in medium to strong seismic risk zones." *Bull Earthquake Engineering*, 10, 1885–1909.

Amadio, C., Fragiacomo, M., and Rajgelj, S. (2003). "The effects of repeated earthquake ground motions on the non-linear response of SDOF systems." *Earthquake Engineering and Structural Dynamics*, 32, 291–308.

ATC (1996). *Improved seismic design criteria for California bridges: provisional recommendations*. Applied Technology Council, California, ATC-32 edition.

Basoz, N. and Kiremidjian, A. (1997). "Evaluation of bridge damage data from the Loma Prieta and Northridge, CA earthquakes." *Report No. MCEER-98-0004*, John A. Blume Earthquake Engineering Center.

Bley, D., Kaplan, S., and Perla, H. (1983). "A methodology for seismic risk analysis of nuclear power plants." *Risk Analysis Journal*, 3(3), 169–180.

Boore, D., Watson-Lamprey, J., and Abrahamson, N. (2006). "Orientation-independent measures of ground motion." *Bulletin of the Seismological Society of America*, 96(4A), 1502–1511.

Campbell, R., Hardy, G., Hoy, A., Johnson, J., and Ravindra, M. (1998). "Seismic reevaluation of nuclear facilities worldwide: overview and status." *Nuclear Engineering and Design Journal*, 182, 17–34.

Choe, D., Gardoni, P., Rosowsky, D., and Haukaas, T. (2009). "Seismic fragility estimates for reinforced concrete bridges subject to corrosion." *Structural Safety*, 31, 275–283.

Choi, E., DesRoches, R., and Nielson, B. (2004). "Seismic fragility of typical bridges in moderate seismic zones." *Engineering Structures*, 26(2), 187–199.

Deco, A. and Frangopol, D. (2011). "Risk assessment of highway bridges under multiple hazards." *Journal of Risk Research*, 14(9), 1057–1089.

Der Kiureghian, A. (2002). "Bayesian methods for seismic fragility assessment of lifeline components." *Report No. 21*, American Society of Civil Engineers.

Dong, Y., Frangopol, D., and Saydam, D. (2013). "Time-variant sustainability assessment of seismically vulnerable bridges subjected to multiple hazards." *Earthquake Engineering and Structural Dynamics*, 42, 1451–1467.

Ellsworth, W. (2013). "Injection-induced earthquakes." *Science*, 341.

Elnashai, A., Borzi, B., and Vlachos, S. (2004). "Deformation-based vulnerability functions for RC bridges." *Structural Engineering and Mechanics*, 17(2), 215–244.

Enright, M. and Frangopol, D. (1998). "Probabilistic analysis of resistance degradation of reinforced concrete bridge beams under corrosion." *Engineering Structures*, 20(11), 960–971.

FEMA (1997). *HAZUS 97 technical Manual*. Federal Emergency Management Agency, Washington, D.C.

FEMA (2003). *Multi-hazard loss estimation methomethod: Earthquake model: HAZUS MR4 technical manual*. Federal Emergency Management Agency, Washington, D.C.

FHWA (1995a). *Recording and coding guide for the structure inventory and appraisal of the nations bridges*. Office of Engineering Bridge Division, Federal Highway Administration, FHWA-PD-96-001 edition.

FHWA (1995b). *Seismic retrofitting manual for highway bridges*. Office of Engineering and Highway Operations R&D, Federal Highway Administration, McLean, VA, FHWA-RD-94-052 edition.

Ghosh, J. (2013). "Parameterized seismic fragility assessment and life-cycle analysis of aging highway bridges." Ph.D. thesis, Rice University, Rice University.

Ghosh, J. and Padgett, J. (2010). "Aging considerations in the development of time dependent seismic fragility curves." *Journal of Structural Engineering*, 136(12), 1497–1511.

Ghosh, J., Padgett, J., and M., S.-S. (2015). "Seismic damage accumulation in highway bridges in earthquake-prone regions." *Earthquake Spectra*, 31(1), 115–135.

Heinrich, S. K., Harvey, Jr., P. S., and Muraleetharan, K. K. (2015). *Smart Bridge-Earthquake Bridge Inspection Radii*. University of Oklahoma, Norman, Oklahoma.

Holland, A. (2013). "Earthquakes triggered by hydraulic fracturing in south-central Oklahoma." *Bulletin of the Seismological Society of America*, 103(3), 1784–1792.

Hough, S. and Page, M. (2015). "A century of induced earthquakes in Oklahoma?." *Bulletin of the Seismological Society of America*, 105(6), 2863–2870.

Howard, K., Aaron, J.and Brabb, E., Brock, M., Gower, H., Hunt, S., Milton, D., Muehlberger, W., Nakata, J., Plafker, G., Prowell, D., Wallace, R., and Whitkind, I. (1978). "Preliminary map of young faults in the United States as a guide to possible fault activity." *Report No. MF-916*, United State Geological Survey.

Hwang, H., Jernigan, J. B., and Lin, Y. W. (2000). "Evaluation of seismic damage to Memphis bridges and highway systems." *Journal of Bridge Engineering*, 5(4), 322–330.

Kattell, J. and Eriksson., M. (1998). *Bridge scour evaluation: screening, analysis, and countermeasures*. Forest Service, United States Department of Agriculture (USDA), San Dimas, California.

Keranen, K., Savage, H., Abers, G., and Cochran, E. (2013). "Potentially induced earthquakes in Oklahoma, USA: links between wastewater injection and the 2011 mw 5.7 earthquake sequence." *Geology*, 41(6), 699–702.

Lawson, J. (1985). "Seismicity at the Meers fault." *Earthquake Notes*, 55(1).

Liu, T. and Weyers, R. (1998). "Modeling the dynamic corrosion process in chloride contaminated concrete structures." *Cement and Concrete Research*, 28(3), 365–379.

Llenos, A. and Michael, A. (2013). "Modeling earthquake rate changes in Oklahoma and Arkansas: Possible signatures of induced seismicity." *Bulletin of the Seismological Society of America*, 103(5), 2850–2861.

Mackie, K. and Stojadinovic, B. (2003). "Seismic demands for performance-based design of bridges." *Report No. PEER 312*, Pacific Earthquake Engineering Research Center.

Mander, J. B. (1999). "Fragility curve development for assessing the seismic vulnerability of highway bridges." *Research Progress and Accomplishments*, 89–98.

Mander, J. B., Priestley, M. J. N., and Park, R. (1988). "Observed stress-strain behavior of confined concrete." *Journal of Structural Engineering*, 114(8), 1827–1849.

McGarr, A., Bekins, B., Burkardt, N., Dewey, J., Earle, P., Ellsworth, W., Ge, S., Hickman, S., Holland, A., Majer, E., Rubinstein, J., and Sheehan, A. (2015). "Coping with earthquakes induced by fluid injection." *Science*, 347.

McKenna, F. and Feneves, G. L. (2000). *Open System for Earthquake Engineering Simulation (OpenSees)*. Pacific Earthquake Engineering Research Center, University of California, Berkeley, CA, version 2.5.0 edition.

Nicholson, C. and Wesson, R. (1992). "Triggered earthquakes and deep well activities." *Pure and Applied Geophysics (Pageoph)*, 139(3-4), 561–577.

Nielson, B. (2005). "Analytical fragility curves for highway bridges in moderate seismic zones." Ph.D. thesis, Georgia Institute of Technology, Georgia Institute of Technology.

Nielson, B. and DesRoches, R. (2007a). "Analytical seismic fragility curves for typical bridges in the central and southeastern United States." *Earthquake Spectra*, 23(3), 615–633.

Nielson, B. and DesRoches, R. (2007b). "Seismic fragility methodology for highway bridges using a component level approach." *Earthquake Engineering and Structural Dynamics*, 36, 823–839.

OGS (1987). "Investigation of the Meers fault, Southwestern Oklahoma." *0275-0929*, Oklahoma Geological Survey.

Padgett, J. E. and DesRoches, R. (2007). "Bridge functionality relationships for improved seismic risk assessment of transportation networks." *Earthquake Spectra*, 23(1), 115–130.

Park, R., Priestley, M. J. N., and Gill, W. D. (1982). "Ductility of square-confined concrete columns." *Journal of Structural Engineering*, 108(ST4), 929–950.

Petersen, M., Mueller, C., Moschetti, M., Hoover, S., Rubinstein, J., Llenos, A., Michael, A., Ellsworth, W., McGarr, A., Holland, A., and J., A. (2015). "Incorporating induced seismicity in the 2014 United States national seismic hazard model-results of 2014 workshop and sensitivity studies.," *Report No. 2015-1070*, United Stated Geological Survey.

Rubinstein, J. and Mahani, A. (2015). "Myths and facts on wastewater injection, hydraulic fracturing, enhanced oil recovery, and induced seismicity." *Seismological Research Letters*, 86(4), 1–8.

Sanchez-Silva, M., Klutke, G., and Rosowsky, D. (2011). "Life-cycle performance of structures subject to multiple deterioration mechanisms." *Structural Safety*, 33, 206–217.

Schrage, I. (1981). "Anchoring of bearings by friction." *Special Publication SP70-12*, American Concrete Institute (ACI), Detroit, MI. 197–215.

Scott, B. D., Park, R., and Priestley, M. J. N. (1982). "Stress-strain behavior of concrete confined by overlapping hoops at low and high strain rates." *ACI Journal*, 79(1), 13–27.

Shinozuka, M., Feng, M., Kim, H. K., and Kim, S. H. (2000a). "Nonlinear static procedure for fragility curve development." *Journal of Engineering Mechanics*, 126(12), 1287–1296.

Shinozuka, M., Feng, M., Lee, J., and Naganuma, T. (2000b). "Statistical analysis of fragility curves." *Journal of Engineering Mechanics*, 126(12), 1224–1231.

Shinozuka, M., Feng, M. Q., Kim, H., Uzawa, T., and Ueda, T. (2003). "Statistical analysis of fragility curves." *Report No. MCEER-03-0002*, Multidisciplinary Center for Earthquake Engineering Research (MCEER), Los Angeles, California.

Stewart, M. and Rosowsky, D. (1998). "Time-dependent reliability of deteriorating reinforced concrete bridge decks." *Structural Safety*, 20, 91–109.

Sullivan, I. (2010). "Analytical seismic fragility curves for skewed multi-span steel girder bridges." M.S. thesis, Clemson University, Clemson University.

Townend, J. and Zoback, M. (2000). "How faulting keeps the crust strong." *Geology*, 28, 399–402.

USDOT (2015). *National Bridge Inventory*. Federal Highway Administration, Washington, D.C.

USGS (2016a). "Earthquake facts & earthquake fantasy." *Earthquake Hazards Program*, U. S. Geological Survey, <`http://earthquake.usgs.gov/learn/topics/megaqk_facts_fantasy.php`>. Accessed July 16, 2016.

USGS (2016b). "M 5.8 - 14km nw of pawnee, oklahoma." *Earthquake Hazards Program*, U. S. Geological Survey, <`http://earthquake.usgs.gov/earthquakes/eventpage/us10006jxs#dyfi`>. Accessed November 11, 2016.

USGS (2016c). "Map." *Earthquake Hazards Program*, U. S. Geological Survey, <`https://earthquake.usgs.gov/earthquakes/map/`>. Accessed July 16, 2016.

USGS (2016d). "Poster of the north central oklahoma earthquake of 3 september 2016 - magnitude 5.8." *Earthquake Hazards Program*, U. S. Geological Survey, <`https://earthquake.usgs.gov/earthquakes/eqarchives/poster/2016/20160903.php`>. Accessed September 8, 2016.

USGS (2016e). "Shakemap." *Earthquake Hazards Program*, U. S. Geological Survey, <`https://earthquake.usgs.gov/earthquakes/shakemap/`>. Accessed November 10, 2016.

Vintzeleou, E. N. and Tassios, T. P. (1987). "Behavior of dowels under cyclic deformations." *ACI Structural Journal*, 84(1), 18–30.

Wald, D., Lin, K.-W., Porter, K., and Turner, L. (2008). "ShakeCast: Automating and improving the use of ShakeMap for post-earthquake decision-making and response." *Earthquake Spectra*, 24(2), 533–553.

Zhang, J. and Huo, Y. (2009). "Evaluating effectiveness and optimum design of isolation devices for highway bridges using the fragility function method." *Engineering Structures*, 31, 1648–1660.